BRNO UNIVERSITY OF TECHNOLOGY

VYSOKÉ UČENÍ TECHNICKÉ V BRNĚ

FACULTY OF MECHANICAL ENGINEERING

FAKULTA STROJNÍHO INŽENÝRSTVÍ

INSTITUTE OF MATHEMATICS

ÚSTAV MATEMATIKY

MODELLING 3D FOREST STRUCTURE FOR IMPROVED RETRIEVAL OF FOREST BIOPHYSICAL PROPERTIES

MODELOVÁNÍ 3D STRUKTURY LESA PRO ZLEPŠENÍ ODHADŮ BIOFYZIKÁLNÍCH VLASTNOSTÍ LESA

DOCTORAL THESIS

DIZERTAČNÍ PRÁCE

AUTHOR
AUTOR PRÁCE

Ing. Růžena Janoutová

SUPERVISOR
ŠKOLITEL

doc. PaedDr. Dalibor Martišek, Ph.D.

BRNO 2017

Abstract

The main goal of the thesis was to improve quantitative estimation of vegetation parameters of spruce stand using spectral simulations of three-dimensional radiative transfer model. In the first step, the precise computer 3D model of a spruce tree was created. Since implementation of such precise representation was computationally too demanding for a larger forest canopy, the 3D model had to be simplified. The optimal simplification was found using available spectral airborne data and through comparison with the original 3D spruce model. The optimal simplification yielded an acceptable compromise between computation requirements and accuracy of radiative transfer simulations reproducing the forest stand reflectance. The optimized simplification was subsequently used in retrievals estimating the vegetation parameters from a spectral satellite image. Accuracy of the estimates was validated through comparison with field measurements of retrieved parameters.

Finally, the results obtained after implementation of new optimal 3D spruce model were compared with results obtained using a more traditional approach based on geometrically simpler tree crown shapes.

Abstrakt

Hlavním cílem práce bylo zlepšení kvantitativních odhadů vegetačních parametrů smrkových porostů pomocí spektrálních simulací trojrozměrného modelu přenosu záření. Prvně bylo potřeba vytvořit přesný 3D model smrku. Implementace přesného 3D modelu smrku pro parametrizaci celých lesních porostů je v současné době výpočetně nemožné, bylo tedy nutné tento 3D model smrku zjednodušit. Přesný 3D model smrku společně s dostupnými leteckými daty sloužil pro nalezení optimálního zjednodušení. Optimální model vedl ke kompromisu mezi výpočetní náročností a přesností výsledné odrazivosti z modelu přenosu záření. Následně byl optimální model smrku využit pro odhady vegetačních parametrů ze satelitních snímků. Přesnost odhadů byla ověřena oproti pozemním měřením odhadovaných parametrů. Na závěr byly porovnány výsledky z odhadů vegetačních parametrů pomocí optimálního 3D modelu smrku s výsledky z tradičního přístupu pomocí modelů stromu s geometricky jednodušími tvary korun.

Keywords
radiative transfer model, DART, 3D spruce model, estimation of vegetation parameters

Klíčová slova
model přenosu záření, DART, 3D model smrku, odhady vegetačních parametrů

I declare that I have written the doctoral thesis *Modelling 3D forest structure for improved retrieval of forest biophysical properties* on my own according to advice of my supervisor doc. PaedDr. Dalibor Martišek, Ph.D., and using the sources listed in references.

February 14, 2017   Ing. Růžena Janoutová

Table of contents

1 | Introduction

1.1 Thesis structure and synopsis

Remote sensing (RS) is a multidisciplinary scientific domain for measuring the electromagnetic radiance reflected and radiated from Earth surfaces. One kind of RS imaging spectroscopy data is called hyperspectral spectroscopy. It contains tens to hundreds reflectance images representing very narrow wavelength intervals within the continuous optical spectral range of 400 – 2500 nm. The hyperspectral images are frequently used for mapping of vegetation traits such as content of chlorophylls a+b (Cab), leaf area index (LAI), etc.

Methods of quantitative estimation of plant Cab using proximal and RS data can be divided in two major groups: i) empirical and ii) physical approaches (Liang 2005). Empirical approaches build on a simple regression relationship established between field measured Cab and reflectance data (Curran et al. 2001; Gitelson et al. 2003; Main et al. 2011). Physical approaches use radiative transfer models (RTM), for instance the Discrete Anisotropic Radiative Transfer (DART) model (Gastellu-Etchegorry et al. 2015), to simulate plant-light interactions. RTMs provide an explicit link between their outputs, simulated top-of-canopy reflectance, and input characteristics, i.e. biochemical and structural properties of the main scattering elements – leaves (Jacquemoud et al. 2009).

The thesis is consisting of several consecutive methodological steps illustrated in Figure 1.1: i) creation of representative 3D spruce tree model from terrestrial laser scanning data, ii) three-level optimization of the 3D tree model, iii) DART forward simulations of spruce forest, and iv) estimation and validation of Cab and LAI from the Sentinel-2 satellite image.

The wooden skeleton of a tree is an important part of the 3D spruce model. It contributes to reflected radiance of a whole forest stand scene due to a high near infrared reflectance, especially in cases of low LAI and sparse forest canopy cover. The reconstruction of wooden skeleton was realized with an automatic algorithm designed by Sloup (2013), which uses the terrestrial Light Detection and Ranging (LiDAR) scans of single trees. The LiDAR point cloud are also used for virtual distribution of needle-age classes shoots within a tree crown.

Correct shoot distribution and assignment of the foliage optical properties within a spruce tree crown is not an easy task. The Norway spruce is an evergreen tree, which means that its crown contains shoots of several (on average five) ages (Figure 1.2a). Needles of current year have significantly different optical properties when compared to older needles (Figure 1.3), whereas the differences among older age classes are much less significant. It is important to characterize these differences in our model, because they play an important role in estimation of quantitative parameters of whole canopy. Unfortunately, the shoot age is not the only aspect influencing optical properties of needles. Another important aspect is the amount and canopy penetration of incoming photosynthetically active solar irradiance (Figure 1.2b), which stimulates growth of new foliage and consequently the number of current year needles in vertical profile of tree crown. The dependences between optical properties and distribution of leaf biomass within a tree spruce crown is depicted in Figure 1.3. Therefore, a new algorithm had to be designed for correct distribution of needle shoots in spruce crown, which is one

of the main outcomes of this thesis.

It must be acknowledged that the reflectance of forests, captured in remotely sensed data, is strongly modulated by its architecture and canopy structure. Different approaches allow one to consider the architectural an structural forest features when simulating remote sensing optical data in RTMs. The traditional approach in the DART model, considered in this study as the base model, is to treat forest as a 3D matrix of voxels (cells) shaped geometrically in crowns and filled with a homogeneous turbid medium of foliage particles. Each vegetation turbid cell contains virtual particles with predefined optical and structural properties of leaves, in our case the shoots of needles, where $G(\Omega)$ is the function representing the interception of light by foliar area unit along direction Ω, which is weighted by a coefficient $\alpha(\Omega)$. The coefficient expresses the foliage clumping within and between tree crowns, i.e. at levels of shoots/branches and spruce trees, respectively. The density and the geometrical distribution of turbid medium particles is determined by the LAI and the leaf angle distribution (LAD) and other vegetation structural parameters of the DART model. However, this approach is not always fully satisfactory, because $\alpha(\Omega)$ is an empirically derived weight and because LAD is defined as a simplified function, which might not be able to properly describe the complex spruce structure. As the result, the direct comparison of DART top-of-canopy reflectance simulations and RS observation shows in some cases significant intensity differences (Figure 3.15a). This discrepancy is the main motivation for improvement of spruce forest simulation in the DART model. One of the key DART inputs are tree representations - 3D models, which characterize architecture of each forest species. Compared to the base turbid-cell models, the explicit 3D tree models are highly computationally demanding, and in case of too large forested scenes with large amount of trees unfeasible to simulate.

Therefore, an optimization of 3D spruce model at three scale levels (shoots, tree crowns, and canopy) was conducted. Two new simplified shoot models were designed and their reflectance simulated with the DART model was cross-compared with reflectance of i) an original geometrically complex shoot containing single needles (reference shoot) and ii) a shoot previously simplified by DART developers. DART simulations with new shoots, implemented in a single-tree mock-up, were compared with the same simulation of exact 3D spruce model, converted and original turbid cell tree, as well as real airborne data. Since it was impossible to use 3D spruce model in whole forest stand simulations, only the last two comparisons were performed at the canopy level.

The final part of this study is devoted to estimation of the two vegetation parameters, Cab and LAI, retrieved from satellite RS image using the DART simulations over the optimized representation of the spruce canopy. Accuracy of the estimations is compared with those achieved using the base turbid cell model.

1.2   Research goals

The main goal of this study is to improve accuracy of quantitative vegetation parameters for Norway spruce stand estimated through inversion of the DART model. This main goal can be divided in the following specific aims:

1. Creation of the geometrically precise 3D model of Norway spruce (*Picea abies* [L.] Karst.) according to point clouds obtained for individual trees at the Bílý Kříž study site with the terrestrial laser scanning approach (Section 3.3).

2. Optimization of computationally too demanding 3D spruce model for operational implementation in RTM, specifically in the DART model.

3. Assessment of improvements due to the new 3D spruce model and its derivate, i.e. a converted turbid cell models of spruce trees. This aim can be broken down in three consecutive steps:

- Creation of an optimized spruce forest stand DART scene and simulation of a DART reflectance look-up-tables (LUT).

- Retrieval of spruce canopy parameters from a multispectral satellite image through an inversion using DART LUT.

- Validation and accuracy assessment of the estimates through comparison with field Cab and LAI measurements.

creating of
3D spruce model
from laser scanning data

whole point cloud
wooden point cloud
wooden skeleton
wooden skeleton + foliage point cloud
wooden skeleton + 3D shoot models
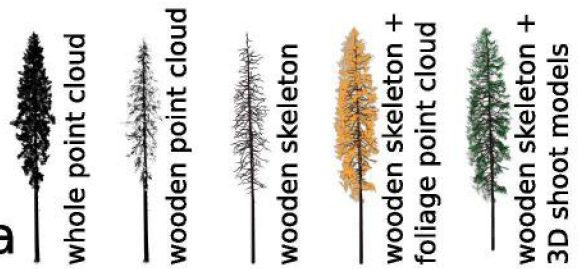
3D spruce model optimization at three levels

shoot level

tree level

canopy level
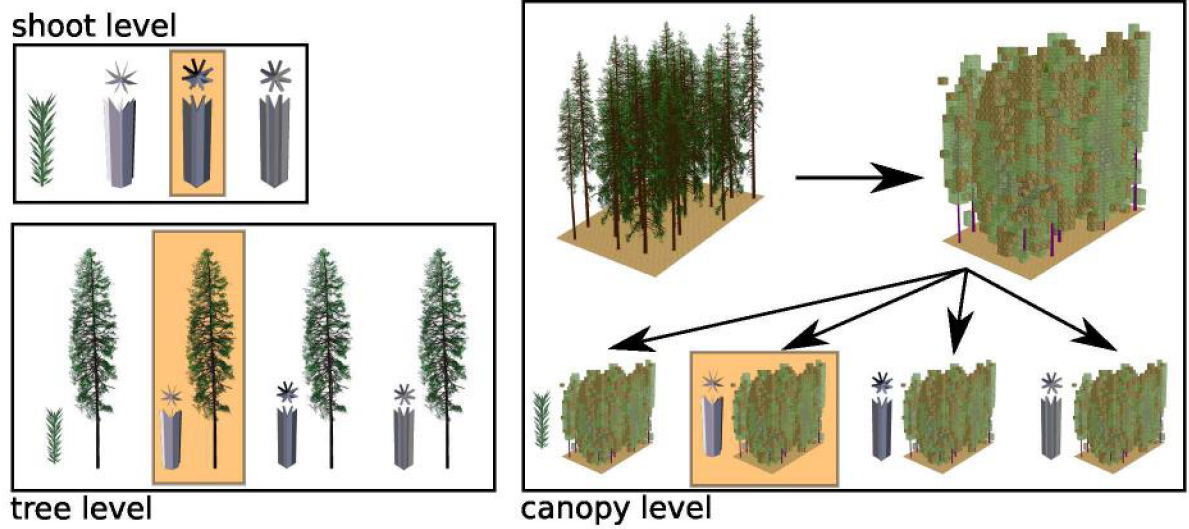
DART - radiative transfer modelling
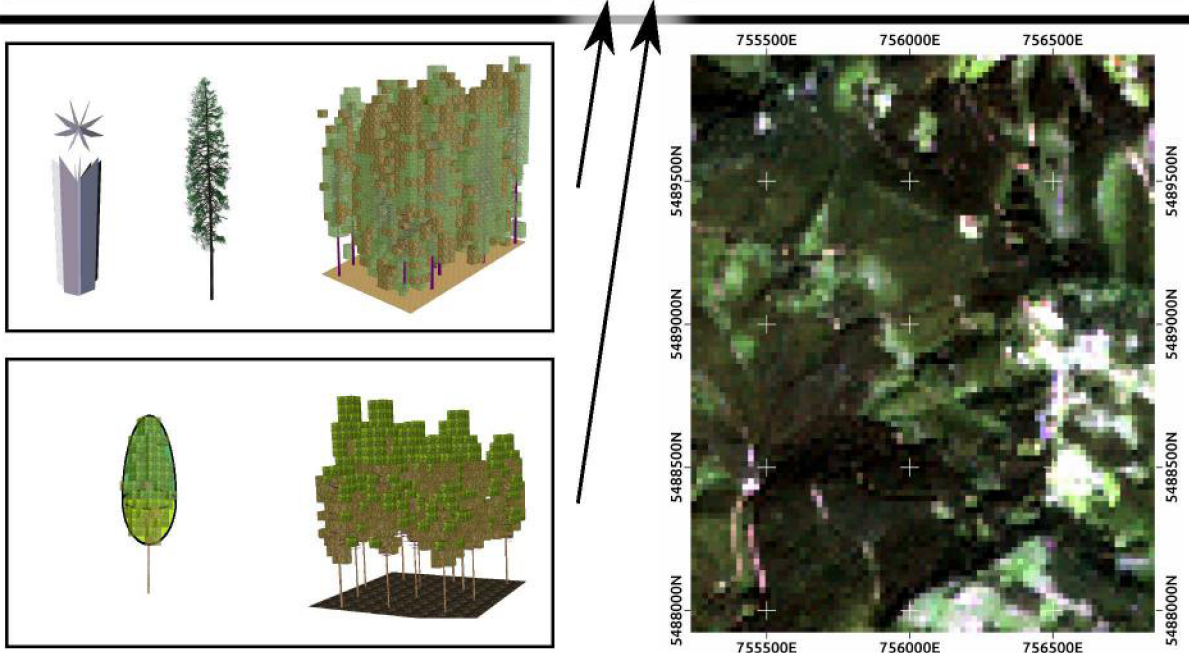
estimation of vegetation parameters from
remote sensing satellite data and validation

Figure 1.1: The workflow diagram of this thesis. The orange boxes indicate the optimal solution for each optimization level.

7

(a) Distribution of needle shoots of the last three age classes. The orange ellipses represent the current shoots, inside the blue ellipses are the one year old shoots, and the pink ellipses indicates the two years old shoot.
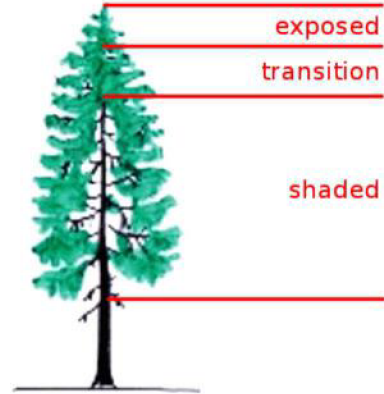
(b) Distinction of shoots based on foliage adaptation to the amount of incident photosynthetically active solar irradiance.

Figure 1.2: Distribution of shoots within the tree crown according to age and incident solar irradiance.
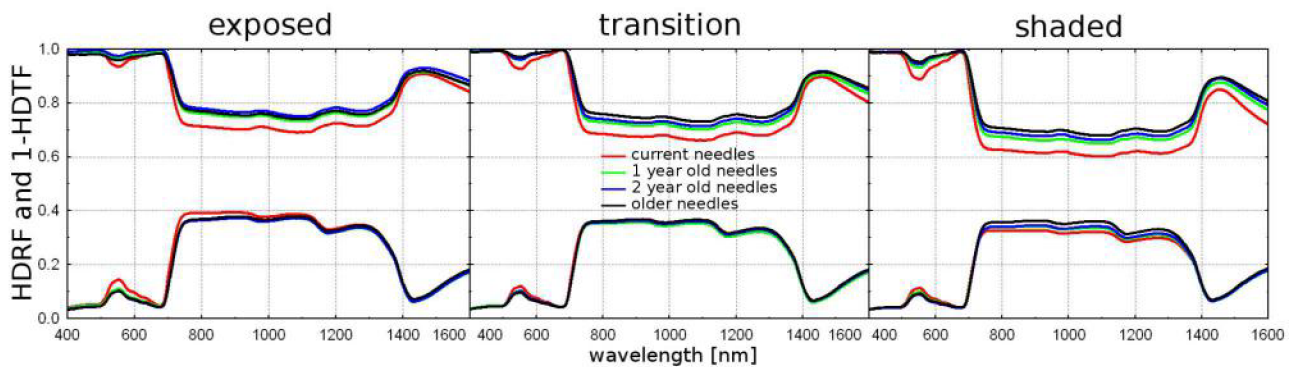
Figure 1.3: The needle optical properties in young trees (cca 30 years) split in three categories - exposed, transition, and shaded. In the graphs is reflectance (HDRF - lower curve) and 1-transmittance (HTRF - upper curve). Here are separated also the different age of the needles.

8

2 | Theoretical background

At the beginning, it is needed to define terms used throughout this thesis. The theoretical part is separated into three main sections. First, the theory concerning the creation of the 3D spruce model, second, the theory connected to radiative transfer modelling, and third, the theory behind estimation of vegetation parameters from RS data is described here. Because the topic of this thesis is very wide, it combines different fields of mathematics and physics, therefore not every single term is defined in details. The precise definitions are used only for the terms used directly in this thesis and for instances with multiple definitions.

2.1 3D spruce model

Creation of the 3D spruce model is one of the main goals and it is necessary to define theory behind algorithms designed in this study. The 3D spruce model based on LiDAR data was created, therefore the first part of this section introduces theory of laser scanning (Section 2.1.1). The LiDAR data were processed in space and thus different geometrical transformations are defined in Section 2.1.2. The two parts of the 3D spruce model - wooden skeleton and foliage parts were reconstructed separately. The creation of the foliage part determines the shoot positions and for that computer graphics extended to 3D space (Section 2.1.3) and cluster analysis theory (Section 2.1.5) were used. The theory of cluster analysis requires definitions from statistics theory, which is also used in other parts of the thesis and therefore it is introduced more deeply in Section 2.1.4.

2.1.1 Laser scanning

Portable terrestrial laser scanning systems are increasingly being used for studies of canopy structure from the ground. LiDAR systems employ similar principles to radar systems. The laser sends out a series of very short pulses of a very narrow beam of coherent light, in a precise waveband; the time delay of the reflected pulse can then be used to determine the distance between the sensor and the reflecting surface.

The first sensors recorded only one echo per pulse, but with vegetation may be echoes from leaves at different levels, branches, and background. Multiecho sensors may detect several returns for one pulse including the first and last returns. In full-waveform mode, instead of just sampling the returned pulse at a few points, recent developments have enabled the whole of the waveform to be analyzed using a form of Gaussian decomposition to extract the component echoes (Figure 2.1). In addition to providing 3D coordinates of scatterers in the canopy, analysis of the full-waveform data can provide useful biophysical information on the nature of the scattering surface. This section was adapted from Jones & Vaughan (2010) and Morsdorf et al. (2006).
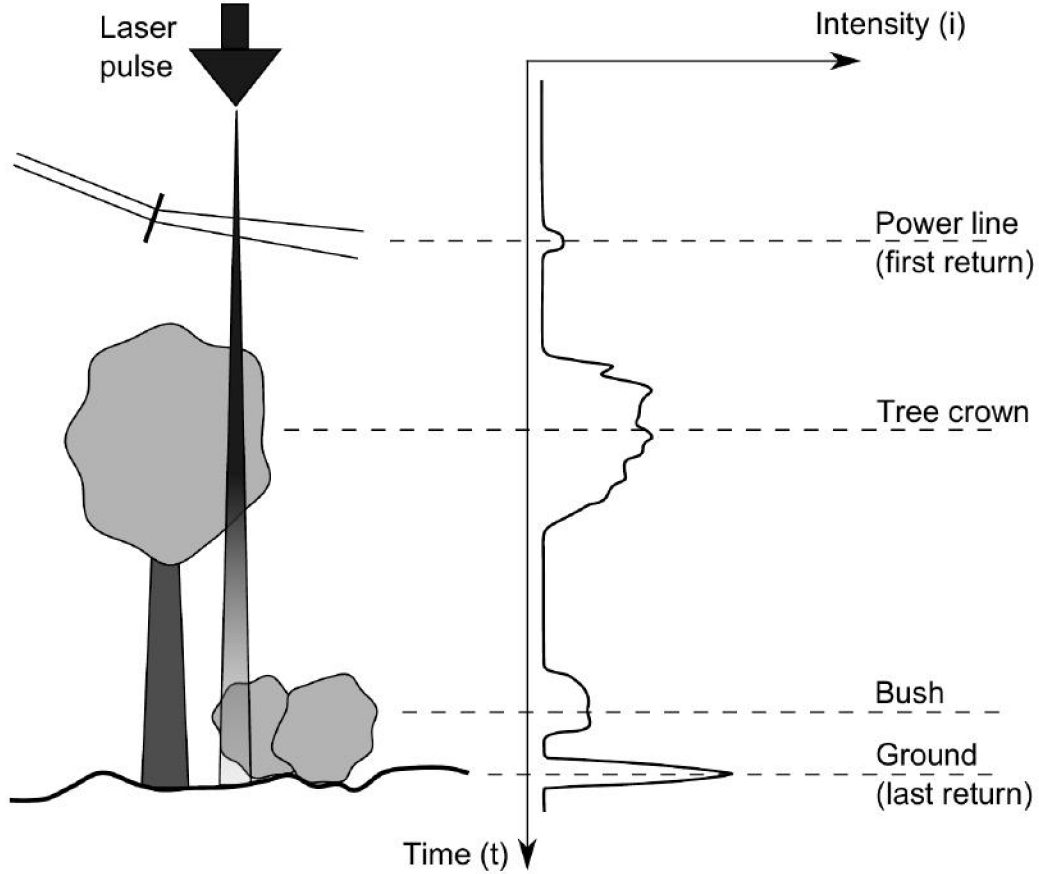
Figure 2.1: Full waveform laser scanning system provides complete digitization of returned signal (adopted from Hanzl et al. 2014)

2.1.2 Image processing

The theory of image processing was applied in the algorithm for creation of the 3D spruce model, especially for the shoot distribution using the LiDAR data (Section 3.3.3). Since the LiDAR data are three-dimensional, it is needed to extend the theory from 2D to 3D space.

The term *image* refers to a two-dimensional light-intensity function. Since light is a form of energy, $f(x, y)$ must be nonzero and finite.

Definition 2.1.1. The image is any continuous nonnegative and finite function f with domain $\langle 0; H - 1) \times \langle 0; W - 1)$, where H is height and W width of the image. Function value $f(x, y)$ of function f in the point (x, y) is called intensity (or brightness).

Definition 2.1.1 gives

$$0 < f(x, y) < \infty \tag{2.1}$$

the image consist of light reflected from objects. $f(x, y)$ is characterized by two components. One is amount of source light incident on the scene called *illumination* and denoted as $i(x, y)$. Second is amount of light reflected by the objects in the scene called *reflectance* denoted as $r(x, y)$. The functions $i(x, y)$ and $r(x, y)$ combine as a product to form $f(x, y)$:

$$f(x, y) = i(x, y)r(x, y), \tag{2.2}$$

where

$$0 < i(x,y) < \infty \tag{2.3}$$

and

$$0 < r(x,y) < 1 \tag{2.4}$$

(Gonzalez 2002).

Equation 2.4 indicates the fact that reflectance is bounded by 0 (total absorption) and 1 (total reflection). The nature of $i(x,y)$ is determined by the light source, while $r(x,y)$ is determined by the characteristics of the object in scene.

The form suitable for computer processing of the image function $f(x,y)$ must be digitized both spatial and in amplitude. Digitization of the spatial coordinates (x,y) is referred as *sampling*, while amplitude digitization will be called *quantization* (Gonzalez 2002).

Definition 2.1.2. The matrix

$$\mathbf{F} = \begin{pmatrix} f(0,0) & f(0,1) & \cdots & f(0,W-1) \\ f(1,0) & f(1,1) & \cdots & f(1,W-1) \\ \vdots & \vdots & \ddots & \vdots \\ f(H-1,0) & f(H-1,1) & \cdots & f(H-1,W-1) \end{pmatrix}, \tag{2.5}$$

where $W, H \in \mathbb{N}$ is the discrete approximation of the image $f(x,y)$.

the right side of the equation represents *digital image*, while each element of the array is referred as *pixel* (Gonzalez 2002).

Definition 2.1.3. The pixels with coordinates:

$$(x+1,y), (x-1,y), (x,y+1), (x,y-1) \tag{2.6}$$

are called *4-neighbors* of $p = (x,y)$ and will be denoted by $N_4(p)$. The pixels with coordinates:

$$(x+1,y+1), (x+1,y-1), (x-1,y+1), (x-1,y-1) \tag{2.7}$$

are called diagonal neighbors and will be denoted $N_d(p)$. These points, together with the $N_4(p)$, are called the *8-neighbors* of p, denoted $N_8(p)$.

Some of the points in $N_4(p)$, $N_d(p)$ or $N_8(p)$ can be outside the image if (x,y) is on border of the image (Gonzalez 2002).

For our purpose we need to extend the definition of neighbors for 3D space. This requires equivalent definitions of image and pixel.

Definition 2.1.4. The 3D - image is any continuous nonnegative and finite function f_3 with domain $\langle 0; H-1 \rangle \times \langle 0; W-1 \rangle \times \langle 0; D-1 \rangle$, where H is height, W width, and D is depth of the image. Function value $f_3(x,y.z)$ of function f_3 in the point (x,y,z) is called intensity (or brightness).

Definition 2.1.4 gives

$$0 < f(x,y,z) < \infty \tag{2.8}$$

Also in case of 3D-image is need to digitized function $f_3(x,y,z)$.

Definition 2.1.5. The matrix

$$\mathbf{F}_3 = (f_3(i, j, k)), \tag{2.9}$$

where $i \in \langle 0; H - 1 \rangle$, $j \in \langle 0; W - 1 \rangle$, $k \in \langle 0; D - 1 \rangle$, and $W, H, D \in \mathbb{N}$, is the discrete approximation of the image $f_3(x, y, z)$.

Definition 2.1.6. *Voxel* is an element of discrete approximation of three-dimensional image representing a volume. It is three-dimensional equivalent of pixel.

Definition 2.1.7. A voxels with coordinates:

$$(x + 1, y, z), (x - 1, y, z), (x, y + 1, z), (x, y - 1, z), (x, y, z + 1), (x, y, z - 1). \tag{2.10}$$

are called *facet-neighbors* of $v = (x, y, z)$ and will be denoted by $N_f(v)$. The twelve neighbors of v, which have exactly one common edge with v with coordinates

$$
\begin{aligned}
&(x + 1, y + 1, z), (x + 1, y - 1, z), (x - 1, y + 1, z), (x - 1, y - 1, z), \\
&(x + 1, y, z + 1), (x + 1, y, z - 1), (x - 1, y, z + 1), (x - 1, y, z - 1), \\
&(x, y + 1, z + 1), (x, y + 1, z - 1), (x, y - 1, z + 1), (x, y - 1, z - 1)
\end{aligned} \tag{2.11}
$$

are called *edge-neighbors* and will be denoted $N_e(v)$. The last eight neighboring voxels, which have exactly one common corner with v with coordinates

$$
\begin{aligned}
&(x + 1, y + 1, z + 1), (x + 1, y + 1, z - 1), (x + 1, y - 1, z + 1), (x + 1, y - 1, z - 1) \\
&(x - 1, y + 1, z + 1), (x - 1, y + 1, z - 1), (x - 1, y - 1, z + 1), (x - 1, y - 1, z - 1)
\end{aligned} \tag{2.12}
$$

are called *corner-neighbors* and will be denoted $N_c(v)$. The sets of voxels $N_f(v)$, $N_e(v)$, and $N_c(v)$ together are called *26-neighbors* and will be denoted $N_{26}(v)$.

2.1.3 Linear transformations

Fundamental of matrix theory are applied for transformation of the LiDAR point clouds (foliage and wooden) and 3D objects (wooden skeleton and 3D shoot models). The following transformations were used: translation, rotation, and scaling. Translation and scaling were used for adaptation of the scanned trees to the required size (Section 3.3.2). Translation and rotation were applied for the distribution of shoot models. All the transformations are defined in the 3D space.

Definition 2.1.8. The transformation of the point $A(x, y, z)$ to the point $A^*(x^*, y^*, z^*)$ is called the translation if and only if

$$
\begin{aligned}
x^* &= x + v_x \\
y^* &= y + v_y \\
z^* &= z + v_z
\end{aligned} \tag{2.13}
$$

Equation 2.13 may be expressed in matrix representation by writing:

$$\mathbf{X}^* = \mathbf{TX} \tag{2.14}$$

in more detail:

$$\begin{pmatrix} x^* \\ y^* \\ z^* \\ 1 \end{pmatrix} = \begin{pmatrix} 1 & 0 & 0 & v_x \\ 0 & 1 & 0 & v_y \\ 0 & 0 & 1 & v_z \\ 0 & 0 & 0 & 1 \end{pmatrix} \begin{pmatrix} x \\ y \\ z \\ 1 \end{pmatrix} \tag{2.15}$$

the matrix $\mathbf{T}$ represents the transformation matrix of translation. The other transformation can be also represented by transformation matrices. Here are defined only the transformation matrices and the expressions for the other transformations can be derived the same way.

Definition 2.1.9. The transformation which is given by matrix

$$\mathbf{S} = \begin{pmatrix} S_x & 0 & 0 & 0 \\ 0 & S_y & 0 & 0 \\ 0 & 0 & S_z & 0 \\ 0 & 0 & 0 & 1 \end{pmatrix} \tag{2.16}$$

is called scaling by factor S_x, S_y, and S_z along the x, y, and z axes.

Definition 2.1.10. the transformation which is given by matrix

$$\mathbf{R_x} = \begin{pmatrix} 1 & 0 & 0 & 0 \\ 0 & cos\alpha & -sin\alpha & 0 \\ 0 & sin\alpha & cos\alpha & 0 \\ 0 & 0 & 0 & 1 \end{pmatrix} \tag{2.17}$$

is called rotation of a point about x axis by an angle α.

Definition 2.1.11. The transformation which is given by matrix

$$\mathbf{R_y} = \begin{pmatrix} cos\beta & 0 & -sin\beta & 0 \\ 0 & 1 & 0 & 0 \\ sin\beta & 0 & cos\beta & 0 \\ 0 & 0 & 0 & 1 \end{pmatrix} \tag{2.18}$$

is called rotation of a point about the y by an angle β.

Definition 2.1.12. The transformation which is given by matrix

$$\mathbf{R_z} = \begin{pmatrix} cos\gamma & -sin\gamma & 0 & 0 \\ sin\gamma & cos\gamma & 0 & 0 \\ 0 & 0 & 1 & 0 \\ 0 & 0 & 0 & 1 \end{pmatrix} \tag{2.19}$$

is called rotation of a point about z axis by an angle γ.

Simple transformations defined in 2.1.9–2.1.12 can be used for construction of more complicated cases. For example, translation, scaling, ad rotation about z axis is given by $\mathbf{X}^* = \mathbf{MX}$, where $\mathbf{M} = \mathbf{R_z}\mathbf{ST}$ is the 4×4 matrix. It is important to note that these matrices generally do not commute, so the order of application is important.

2.1.4   Statistics

Theory of cluster analysis (Section 2.1.5), support vector machines (Section 2.3.4) is build on theory of statistics. The following definitions are adopted from Introduction to Mathematical Statistics (Hogg & Craig 1978).

Definition 2.1.13. The nonempty set Ω of every possible outcomes of a random experiment is called the *sample space*.

Definition 2.1.14. Let $\mathcal{P}(C)$ be a function defined for each subset C of the space Ω, and if

(a) $\mathcal{P}(C) \geq 0$; probabilities are positive,

(b) $\mathcal{P}\left(\bigcup\limits_{i=1}^{\infty} C_i\right) = \sum\limits_{i=1}^{\infty} \mathcal{P}(C_i)$, where the sets $C_i, i = 1, 2, ..., n$, are disjoint (that is, where $C_i \cup C_j = \varnothing, i \neq j$,

(c) $\mathcal{P}(\Omega) = 1$; the probability of all the outcomes combined is 1 (has to happen),

then $\mathcal{P}(C)$ is called the *probability function* of the outcome of the random experiment.

Following theorems give some other properties of a probability function.

Theorem 2.1.1. For each $C \subset \Omega$, $\mathcal{P}(C) = 1 - \mathcal{P}(C^*)$, where $\Omega = C \cup C^*$ and $C \cap C^* = \varnothing$.

Theorem 2.1.2. The probability of the null set is zero; that is, $\mathcal{P}(\varnothing) = 0$.

Theorem 2.1.3. If C_1 and C_2 are subset of Ω such that $C_1 \subset C_2$, then $\mathcal{P}(C_1) \leq \mathcal{P}(C_2)$.

Theorem 2.1.4. For each $C \subset \Omega$, $0 \leq \mathcal{P}(C) \leq 1$.

Theorem 2.1.5. If C_1 and C_2 are subsets of Ω, then

$$\mathcal{P}(C_1 \cup C_2) = \mathcal{P}(C_1) + \mathcal{P}(C_2) - \mathcal{P}(C_1 \cap C_2)$$

Definition 2.1.15. Given a random experiment with a sample space Ω. A function X, which assigns to each element $c \in \Omega$ one and only one real number $X(c) = x$, is called a *random variable*. The *space* of X is the set of real numbers $\mathcal{A} = \{x; x = X(c), c \in \Omega\}$. The probability of event A is denoted by $\mathcal{P}_r(X \in A)$, where $\mathcal{P}_r$ is an abbreviation of "the probability that."

It may be that the set Ω has the elements which are themselves real numbers. In such an instance we could write $X(c) = c$ so that $\mathcal{A} = \Omega$.

Let X be a random variable that is defined on a sample space Ω, and let $\mathcal{A}$ be the space of X. Further, let A be a subset of $\mathcal{A}$. Just as we used terminology "the event C," with $C \subset \Omega$, we shall now speak of "the event A."

With A a subset of $\mathcal{A}$, let C be that subset of Ω such that $C = \{c; c \in \Omega \text{ and } X(c) \in A\}$. Thus C has its elements outcomes in Ω for which the random variable X has a value that is in A.

Let $\mathcal{P}_r$ be an assignment of probability to a set A, which is a subset of the space $\mathcal{A}$ associated with random variable X. This assignment is determined by the probability function $\mathcal{P}$ and the random variable X and is sometimes denoted by $\mathcal{P}_x(A)$. That is,

$$\mathcal{P}_r(X \in A) = \mathcal{P}_x(A) = \mathcal{P}(C), \tag{2.20}$$

where $C = \{c; c \in \Omega \text{ and } X(c) \in A\}$. Thus random variable X is a function that carries the probability from a sample space Ω to a space $\mathcal{A}$ of real numbers. In this sense, with $A \subset \mathcal{A}$, the probability $\mathcal{P}_x(A)$ is often called an *induced probability*.

The function $\mathcal{P}_x(A)$ satisfies the condition (a), (b) and (c) from Definition 2.1.14. That is, $\mathcal{P}_x(A)$ is also a probability function.

Note: *There should be fully recognized that the probability set function $\mathcal{P}$ is defined for subset C of Ω, whereas $\mathcal{P}_x$ is defined for subset A of $\mathcal{A}$, and in general they are not the same function. Nevertheless, they are closely related. Therefore in further text the probability function $\mathcal{P}_x(A)$ is denoted as $\mathcal{P}(A)$.*

Definition 2.1.16. Given a random experiment with a sample space Ω. Consider two random variables X_1 and X_2, which assign to each element c of Ω one and only one ordered pair of numbers $X_1(c) = x_1$, $X_2(c) = x_2$. The set of ordered pairs $\mathcal{A} = \{(x_1, x_2); x_1 = X_1(c), x_2 = X_2(c), c \in \Omega\}$ is called the *space* of X_1 and X_2.

Let $\mathcal{A}$ be the space associated with the two random variables X_1 and X_2 and let A be a subset of $\mathcal{A}$. As in the case of one random variable, we shall speak of the event A. We define the probability of the event A, which we denote by $\mathcal{P}_r[(X_1, X_2) \in A]$. Take $C = \{c; c \in \Omega$ and $[X_1(c), X_2(c)] \in \mathcal{A}\}$, where Ω is the sample space. We then define $\mathcal{P}_r[(X_1, X_2) \in A] = \mathcal{P}(C)$, where $\mathcal{P}$ is the probability function defined for subset C in Ω. Here again we could denote $\mathcal{P}_r[(X_1, X_2) \in A]$ by the probability function $\mathcal{P}_{x_1, x_2}(A)$, but with previous note, we simply write

$$\mathcal{P}(A) = \mathcal{P}_r[(X_1, X_2) \in A]. \tag{2.21}$$

The preceding notions about one and two random variables can be immediately extended to n random variable. We make the following definition of the space of n random variables.

Definition 2.1.17. Given a random experiment with the sample space Ω. Let the random variable X_i assign to each element $c \in \Omega$ one and only one real number $X_i(c) = x_i$, $i = 1, 2, ..., n$. The set of ordered n-tuplets $\mathcal{A} = \{(x_1, x_2, ..., x_n); x_1 = X_1(c), x_2 = X_2(c), ...x_n = X_n(c), c \in \Omega\}$ is called the *space* of random variables.

Further, let A be a subset of $\mathcal{A}$. Then $\mathcal{P}_r[(X_1, X_2, ..., X_n) \in a] = \mathcal{P}(C)$, where $C = \{c; c \in \Omega$ and $[X_1(c), X_2(c), ..., X_n(c)] \in a\}$.

Let X denote a random variable with space $\mathcal{A}$ and let A be a subset of $\mathcal{A}$. If we know how to compute $\mathcal{P}(C)$, $C \subset \Omega$, then for each A under consideration we can compute $\mathcal{P}(A) = \mathcal{P}_r(X \in A)$; that is, we know how the probability is distributed over the various subsets of $\mathcal{A}$. In this sense, we speak of the distribution of the random variable X, meaning, of course, the distribution of probability.

Some random variables distributions can be described very simply by what will be called the *probability density function*. The two types of distributions that shall be considered are called, respectively, *discrete type* and the *continuous type*. For simplicity of presentation, we first consider a distribution of on random variable.

Let X denote a random variable with 1D space $\mathcal{A}$. Where the space $\mathcal{A}$ is a set of points such that there is at most a finite of points of $\mathcal{A}$ in every finite interval. Such a set $\mathcal{A}$ will be called a set of discrete points. Let $f(x)$ be a function such that $f(x) > 0$, $x \in \mathcal{A}$, and that

$$\sum_{\mathcal{A}} f(x) = 1. \tag{2.22}$$

Whenever a probability function $\mathcal{P}(A)$, $A \subset \mathcal{A}$, can be expressed in terms of such an $f(x)$ by

$$\mathcal{P}(A) = \mathcal{P}_r(X \in A) = \sum_{A} f(x), \tag{2.23}$$

then X is called a random variable of the *discrete type*, and X is said to have a distribution of the discrete type.

Let $\mathcal{A}$ be the 1D set such that the Riemann integral

$$\int_{\mathcal{A}} f(x)\, dx = 1, \tag{2.24}$$

where 1) $f(x) > 0$, $x \in \mathcal{A}$, and 2) $f(x)$ has at most a finite number of discontinuities in every finite interval that is a subset of $\mathcal{A}$. If $\mathcal{A}$ is the space of the random variable X and if the probability function $\mathcal{P}(A)$, $A \in \mathcal{A}$, can be expressed in terms of such an $f(x)$ by

$$\mathcal{P}(A) = \mathcal{P}_r(X \in A) = \int_A f(x)\, dx, \tag{2.25}$$

then X is said to be a random variable of the *continuous type* and to have a distribution of that type.

It is seen that whether the random variable X is of the discrete type or of the continuous type, the probability $\mathcal{P}_r(X \in A)$ is completely determined by a function $f(x)$. In either case $f(x)$ is called the *probability density function* of the random variable X.

The notion of the probability density function of one random variable X can be extended to the notion of the probability density function of two or more random variables. Under certain restrictions on the space $\mathcal{A}$ and the function $f > 0$ on $\mathcal{A}$, we say that the two random variables X and Y are of the discrete type or of the continuous type, and have a distribution of that type, according as the probability function $\mathcal{P}$, $A \subset \mathcal{A}$, can be expressed as

$$\mathcal{P}(A) = \mathcal{P}_r[(X, Y) \in A] = \sum_A \sum f(x, y), \tag{2.26}$$

or as

$$\mathcal{P}(A) = \mathcal{P}_r[(X, Y) \in A] = \iint_A f(x, y)\, dxdy. \tag{2.27}$$

In either case f is called the probability density function of the two random variables X and Y. Of necessity, $\mathcal{P}(\mathcal{A}) = 1$ in each case.

More generally, we say that the n random variables X_1, X_2, ..., X_n are of the discrete type or of the continuous type, and have a distribution of that type, according as the probability function $\mathcal{P}(A)$, $A \subset \mathcal{A}$, can be expressed as

$$\mathcal{P}(A) = \mathcal{P}_r[(X_1, X_2, ..., X_n) \in A] = \sum_A \cdots \sum f(x_1, x_2, ..., x_n), \tag{2.28}$$

or as

$$\mathcal{P}(A) = \mathcal{P}_r[(X_1, X_2, ..., X_n) \in A] = \int_A \cdots \int f(x_1, x_2, ..., x_n)\, dx_1\, dx_2 \cdots dx_n. \tag{2.29}$$

Let $f(x_1, x_2)$ be the probability density function of two random variables X_1 and X_2. For emphasis and clarity, we shall call a probability density function or a distribution function a *joint* probability density function or a *joint* distribution function when more than one random variable is involved. Thus $f(x_1, x_2)$ is the joint probability density function of the random variables X_1 and X_2.

Let the random variable X have the probability function $\mathcal{P}(A)$, where A is a 1D set. Take x to be a real number and consider the set A which is an unbounded set from $-\infty$ to x, including the point x itself. For all such sets A we have $\mathcal{P}(A) = \mathcal{P}_r(X \in A) = \mathcal{P}_r(X \leq x)$. This probability depends on the point x; that is, this probability is a function of the point x. This point function is denoted by the symbol $F(x) = \mathcal{P}_r(X \leq x)$. The function $F(x)$ is called the *distribution function* of the random variable X. Since $F(x) = \mathcal{P}_r(X \leq x)$, then, with $f(x)$ the probability density function, we have

$$F(x) = \sum_{\omega \leq x} f(\omega), \tag{2.30}$$

for the discrete type of random variable, and

$$F(x) = \int\limits_{-\infty}^{x} f(\omega)\, d\omega, \tag{2.31}$$

for the continuous type of random variable. We speak of a distribution function $F(x)$ as being of the continuous or discrete type, depending on whether the random variable is of the continuous or discrete type.

There are several properties of a distribution function $F(x)$ that can be listed as a consequence of the properties of the probability function. Some of these are the following. In listing these properties, we shall not restrict X to be a random variable of the discrete or continuous type.

(a) $0 \leq F(x) \leq 1$ because $0 \leq \mathcal{P}_r(X \leq x) \leq 1$.

(b) $F(x)$ is a nondecreasing function of x.

(c) $\lim_{x \to \infty} F(x) = 1$ and $\lim_{x \to -\infty} F(x) = 0$ because the set $\{x; x \leq \infty\}$ is the entire 1D space and set $\{x; x \leq -\infty\}$ is the null set.

(d) $F(x)$ is continuous to the right at each point x.

We shall now point out an important fact about a function of a random variable. Let X denote a random variable with space $\mathcal{A}$. Consider the function $Y = u(x)$ of the random variable X. Since X is a function defined on a sample space Ω, then $Y = u(X)$ is itself a random variable which has its own space $\mathcal{B} = \{y; y = u(x), x \in \mathcal{A}\}$ and its own probability function. If $y \in \mathcal{B}$, the event $Y = u(X) \in y$ occurs if, and only if, the event $X \in A \subset \mathcal{A}$ occurs, where $A = \{x; u(x) \leq y\}$. That is, the distribution function of Y is

$$G(y) = \mathcal{P}_r(Y \leq y) = \mathcal{P}_r[u(X) \leq y] = \mathcal{P}(A). \tag{2.32}$$

One of the more useful concepts in problems involving distributions of random variables is that of mathematical expectations.

Definition 2.1.18. Let X be a random variable having a probability density function $f(x)$, and let $u(X)$ be a function of X such that

$$\int\limits_{-\infty}^{\infty} u(x) f(x)\, dx \tag{2.33}$$

exists (in the case of a continuous type of random variable), or such that

$$\sum_{x} u(x) f(x) \tag{2.34}$$

17

exists (in case of a discrete type of random variable). The integral or the sum is called *mathematical expectation* (or expected values) of $u(X)$ and is denoted by $E[u(X)]$. That is,

$$E[u(X)] = \int_{-\infty}^{\infty} u(x)f(x)\, dx, \tag{2.35}$$

if X is a continuous type of random variable, or

$$E[u(X)] = \sum_{x} u(x)f(x), \tag{2.36}$$

if X is a discrete type of random variable.

Certain mathematical expectations, if they exist, have a special names and symbols to represent them. We shall mention now only those associated with one random variable.

Definition 2.1.19. Let $u(X) = X$, where X is a random variable of the discrete type having a probability density function $f(x)$. The expression

$$E(X) = \sum_{x} x f(x). \tag{2.37}$$

we call the arithmetic mean of the values of X or, more simply, the *mean value* of X (or the mean value of the distribution). The mean value μ of a random variable X is defined to be $\mu = E(X)$, where X is a random variable of the discrete or of the continuous type.

Another special mathematical expectation is obtained by taking $u(X) = (X - \mu)^2$. If, initially, X is a random variable of the discrete type having probability density function $f(x)$, then

$$E[(X - \mu)^2] = \sum_{x} (x - \mu)^2 f(x) \tag{2.38}$$

and for a random variable of continues type

$$E[(X - \mu)^2] = \int_{-\infty}^{\infty} (x - \mu)^2 f(x)dx. \tag{2.39}$$

This mean value of the square of the deviation of X from its mean value μ is called the *variance* of X (or the variance of the distribution). The variance of X will be denoted by σ^2, and we define σ^2, if it exists, by $\sigma^2 = E[(X - \mu)^2]$, whether X is a discrete or a continuous type of random variable.

It is customary to call σ (the positive square root of the variance) the *standard deviation* (SD) of X (or the standard deviation of the distribution).

Let X and Y denote random variables that have joint probability density function $f(x, y)$. If $u(x, y)$ is a function of x and y, then $E[u(x, y)]$ was defined. The means of X and Y, say μ_x and μ_y are obtained by taking $u(x, y)$ to be x and y, respectively; and the variances of X and Y, say σ_x^2 and σ_y^2, are obtained by setting the function $u(x, y)$ equal to $(x - \mu_x)^2$ and $(y - \mu_y)^2$, respectively. Consider the mathematical expectation

$$cov(X, Y) = E[(X - \mu_x)(Y - \mu_y)]. \tag{2.40}$$

This number $cov(X, Y)$ is called *covariance* of X and Y. If each of σ_x and σ_y is positive, the number

$$r_{xy} = \frac{E[(X - \mu_x)(Y - \mu_y)]}{\sigma_x \sigma_y} \tag{2.41}$$

is called the *correlation coefficient* of X and Y.

If a joint distribution of two variables has a correlation coefficient (that is, if both of the variances are positive), then r satisfies $-1 \leq r \leq 1$. If $r = 1$, there is a line with equation $y = a + bx$, $b > 0$, the graph of which contains all of the probability for the distribution of X and Y. In this extreme case, we have $\mathcal{P}_r(Y = a + bX) = 1$. If $r = -1$, we have the same state of affairs except that $b < 0$.

2.1.5 Cluster analysis

The important task in the creation of the 3D spruce model is the shoot distribution. Positions of shoots within the crown were determined from the foliage point cloud and for this task the cluster analysis theory was applied. There are several techniques how the cluster analysis theory can be applied, but in the following section only the one chosen for the study is defined.

Cluster analysis is a family of analytic procedures whose main purpose is to develop meaningful aggregations, or groups, of entities based on a large number of interdependent variables. Specifically, the objective is to classify a sample of entities into a smaller number of usually mutually exclusive groups based on the multivariate similarities among entities. The procedure creates groups using one of many different clustering strategies that, in general, maximizes within-group similarity (i.e. minimize within-group distances in multidimensional space) and minimizes between-group similarity (i.e. maximize between-group distances in multidimensional space) based on the variables. Entities are generally assumed to represent a single random sample (N) of an unknown number of populations (in the statistical sense of the word). The data set must consist of a single set of two or more continuous, categorical, and/or count variables, and there is no distinction between independent and dependent variables. This paragraphs was adapted from McGarigal et al. (2000).

Most of this theory is adopted from Legendre & Legendre (1998), MacKay (2003), and McGarigal et al. (2000)

Definition 2.1.20. *Clustering* is an operation of multidimensional analysis which consists in partitioning the collection of objects (or descriptors) in the study. A *partition* is a division of a set (collection) into subsets, such that each object or descriptor belongs to one and only one subset for that partition (Legendre & Rogers 1972).

the classification of objects (or descriptors) that results from clustering may include a single partition, or several hierarchically nested partitions of the objects (or descriptors), depending on the clustering model that has been selected.

Each object is characterized by a state (its cluster) of the classification and it belongs to only one of the clusters.

Williams et al. (1971) recognize two major categories of methods. In a *descriptive clustering*, misclassifying objects is to be avoided, even at the expense of creating single object cluster. In a *synoptic clustering*, all objects are forced into one of the main clusters; the objective is to construct a general conceptual model which encompasses a reality wider than data under study.

A simple-to-understand method (or model) is single *linkage* (or *nearest neighbor*) clustering (Sneath 1957). The algorithm for single linkage clustering is *sequential*, *agglomerative*, and *hierarchical*. Its starting point is any association matrix (similarity or distance) among the objects or descriptors to be clustered.

Any classification or partition can be fully described by a cophenetic matrix. This matrix is used for comparing different classification of the same object.

Definition 2.1.21. The *cophenetic similarity* (or *distance*) of two objects x_1 and x_2 is the similarity (or distance) level at which objects x_1 and x_2 become members of the same cluster during the course of clustering (Jain & Dubes 1988).

As depicted by connected subgraphs or a dendrogram. Any dendrogram can be uniquely represented by a matrix in which the similarity (or distance) for a pair of objects is their cophenetic similarity (or distance).

Such a matrix is often called a *cophenetic matrix* (Sokal & Rohlf 1962, Jain & Dubes 1988). The ordering of objects in the cophenetic matrix is irrelevant.

There are many different clustering techniques. Several properties of clustering techniques can be used to group methods into manageable categories (Sneath & Sokal 1973, Everitt 1977, Gauch 1982).

2.1.5.1 Exclusive vs. non-exclusive

Exclusive (or non-overlapping) techniques place each entity in one, and only one, group; non-exclusive (or overlapping) techniques place each entity in one or more groups. Most techniques are exclusive.

2.1.5.2 Sequential vs. simultaneous

Sequential techniques apply a recursive sequence of operations to the set of the entities; simultaneous techniques apply a single non-recursive operation to the entities to form clusters. Simultaneous procedures have been explored by a few researchers but have not generally been adopted. Therefore, most of the techniques are sequential.

2.1.5.3 Hierarchical vs. non-hierarchical

Hierarchical techniques group similar entities together into groups and arrange these groups into a hierarchy that expresses the relationships among groups; non-hierarchical techniques merely assign each entity to group, placing similar entities together to achieve within-cluster homogeneity. The non-hierarchical method does not necessarily reveal any interesting structure within clusters or definition of relationships among clusters. Both hierarchical and non-hierarchical procedures have received widespread attention.

2.1.5.4 Agglomeration vs. divisive

Agglomerative techniques begin with each entity in class of its own, then fuse (agglomerate) the classes into larger classes; divisive techniques begin with all entities in a single class and divide this class into progressively smaller classes, stopping when each class contains a single member or when the predetermined limit of some "stopping rule" has been reached.

2.1.5.5 Polythetic vs. monothetic methods

Polythetic techniques consider all the information for each entity when deriving cluster assignments. Monothetic techniques can only be divisive and are often used in community ecology studies involving samples-by-species data, where sets of samples are divided according to the presence or absence of a single species.

2.1.5.6 K-means

In this study exclusive, non-hierarchical, polythetic, divisive cluster method called k-means is used. Therefore, this method is introduced in this section. This method is widely used and there are prepared libraries for example for Matlab, Python, R. Because is no need for high accuracy of shoot position, this method is preferred due to the easy implementation and computer efficiency even if there are some disadvantages of this method. The accuracy is not so important because the variability and extreme cases are common in the nature.

The *centroid* of a cluster of objects may be imagined as the type-object of the cluster, whether that object actually exists or is only a mathematical construct. The coordinates of a cluster are computed by averaging the coordinates of the objects in the group.

To form clusters, the method minimize an *objective function* which is, in this case, the square error criterion.

Let $z_1, z_2, \ldots$ be a random sequence of points (vectors) in E_N, each point being selected independently of the preceding ones using a fixed probability measure $\mathcal{P}$. Thus $\mathcal{P}_r[z_1 \in A] = \mathcal{P}(A)$ and $\mathcal{P}_r[z_{n+1} \in A | z_1, z_2, \ldots, z_n] = \mathcal{P}(A)$, $n = 1, 2, \ldots$, for any measurable set A in E_N.

Definition 2.1.22. Let $x = (x_1, x_2, \ldots, x_k)$, $x_i \in E_N$, $i = 1, 2, \ldots, k$ be a k-tuple. The expressions

$$
\begin{aligned}
S_1(x) &= T_1(x), \\
S_2(x) &= T_2(x) S_1'(x), \\
&\vdots \\
S_k(x) &= T_k(x) S_1'(x) S_2'(x) \cdots S_{k-1}'(x),
\end{aligned}
\tag{2.42}
$$

where

$$
T_i(x) = \{\xi : \xi \in E_N, |\xi - x_i| \le |\xi - x_j|, j = 1, 2, \ldots, k\}.
\tag{2.43}
$$

are called *minimum distance partition* $S(x) = \{S_1(x), S_2(x), \ldots, S_k(x)\}$ of E_N.

the set $S_i(x)$ contains the position in E_N nearest to x_i, with tied points being assigned arbitrarily to the set of lower index.
Note that, if $x_i = x_j$ and $i < j$ then $S_j(x) = \emptyset$, with this convention concerning tied points. Sample k-means $x^n = (x_1^n, x_2^n, \ldots, x_k^n)$, $x_i^n \in E_N$, $i = 1, 2, \ldots, k$, with associated integer weights $(w_1^n, w_2^n, \ldots w_k^n)$, are now defined as follows: $x_i^1 = z_i$, $w_i^1 = 1$, $i = 1, 2, \ldots, k$, and for $n = 1, 2, \ldots$, if $z_{k+n} \in S_i^n$, $x_i^{n+1} = \frac{(x_i^n w_i^n + z_{n+k})}{(w_i^n + 1)}$, $w_i^{n+1} = w_i^n + 1$, and $x_j^{n+1} = x_j^n$, $w_j^{n+1} = w_j^n$ for $j \neq i$, where $S^n = \{S_1^n, S_2^n, \ldots, S_k^n\}$ is the minimum distance partition relative to x_n.

The process, which is called "k-means", appears to give partitions which are reasonably efficient in the sense of within-class variance. That is, if f is the probability density function for the population, $S = \{S_1, S_2 \ldots, S_k\}$ is a partition of E_N, and u_i, $i = 1, 2, \ldots, k$, is the conditional mean of f over the set S_i, then $w^2(S) = \sum_{i=1}^{k} \sum_{z \in S_i} |z - u_i|^2$ tends to be low for the partitions S generated by method.

Stated informally, the k-means procedure consists of simply starting with k groups each of which consists of a single random point, and thereafter adding each new point to the group whose mean the new point is nearest. After a point is added to a group, the mean of that group is adjusted in order to take account of the new point. Thus at each stage the k-means are, in fact, the means of the groups they represent.

The major problem encountered by the algorithms is that the solution on which the computation eventually converges depends to some extent on the initial positions of the centroids. This problem is known as the "local minimum" problem in algorithms.

2.2 Radiative transfer modelling

In remote sensing the usual requirement is to determine the surface reflectance and to make use of this in inferring canopy or surface biophysical characteristics. The use of bidirectional reflectance data greatly enhances the capacity to extract canopy biophysical information when coupled with appropriate radiative transfer (RT) modelling. The various radiative transfer models available vary in the detail in which they treat the anisotropy of the radiation field in canopies. In such modelling it is often convenient to treat the radiation field as the sum of a number of components. These could include the unscattered irradiance, radiation that has been scattered once, and multiply scattered irradiance that has been scattered several times. This paragraph was adapted from Jones & Vaughan (2010).

There are two types of Radiative Transfer Models (RTMs), at the leaf-level and at the canopy-level. Leaf-level models simulate optical properties i.e. light reflectance and transmittance through a leaf. Among the leaf-level RTMs, the PROSPECT model (Jacquemoud & Baret 1990; Feret et al. 2008) is probably the most widely used. This is due to its simplicity and low number of input parameters (leaf chlorophyl a+b (Cab), leaf carotenoid (Car), water (Cw), dry matter content (Cm) and N-number (N)).

Canopy-level RTM effectively scales the leaf optical properties to the level of plant canopies (e.g. agricultural fields, forests). There has been a large number of canopy RTMs developed and they span from relatively simple ones to complex, computationally demanding 3D models. A good overview of currently used canopy RTMs is provided at the website of RAdiation transfer Model Intercomparison (RAMI, http://rami-benchmark.jrc.ec.europa.eu).

Canopy RTMs that attempt to reproduce the complex architecture of trees and forests are naturally more suitable to interpret remote sensing (RS) data acquired over forested areas. Examples of 3D canopy RTMs are: DART (Gastellu-Etchegorry et al. 1996, 2004, and 2015), FLIGHT (North 1996), Raytran (Govaerts & Verstraete 1998), and many others, which are well summarized at the RAMI website. In this thesis the DART model was used.

2.2.1 PROSPECT

PROSPECT simulates leaf reflectance (HDRF) and transmittance (HTRF) from the visible (VIS) to the middle infrared spectrum as a function of the leaf structure parameter and leaf biochemical parameters (Jacquemoud and Baret 1990). It is based on so-called "plate model" developed by Allen et al. (1969), who represented a leaf as a uniform plate with rough surfaces. The leaf reflectance (HDRF) and transmittance (HTRF) are determined in the plate model using geometric optical principles. The fixed parameters include the index of refraction and absorption coefficients of the main absorbing constituents (Cab, Car, Cm, and Cw). This section is adapted from Jones & Vaughan (2010).

The simple plate model was then extended to noncompact leaves by regarding them as piles of N plates separated by N-1 airspaces (Allen et al. 1970). The solution of such a system has been extended to N as a real number, this is so-called generalized plate model.

Mathematically, the total reflectance (HDRF) and transmittance (HTRF) for N layers are given by

$$
\begin{aligned}
R_{N,\alpha} &= x R_{N,90} + y \\
T_{N,\alpha} &= x T_{N,90} \\
x &= \frac{t_{av}(\alpha, n)}{t_{av}(90, n)} \\
y &= x[t_{av}(90, n) - 1] + 1 - t_{av}(\alpha, n),
\end{aligned}
\tag{2.44}
$$

where n is the refractive index of the leaf plate and α is the maximum incident angle; $t_{av}(\alpha, n)$ is the transmittance of a dielectric plane surface, averaged over all directions of incidence and over all polarizations. Finally, this model has four parameters: n, N, α and the transmission coefficient θ that is related to the absorption coefficient k through the following equation (Allen 1969):

$$\theta - (1-k)e^{-k} - k^2 \int_k^\infty x^{-1} e^{-x} dx = 0 \qquad (2.45)$$

the spectral absorption coefficient $k(\lambda)$ can be written in the form

$$k(\lambda) = \sum K_i(\lambda) C_i + k_0, \qquad (2.46)$$

where k_0 is the intercept, $K_i(\lambda)$ is the spectral specific absorption coefficient relative to the leaf component i. And C_i is the leaf component i content per unit leaf area.

In this thesis were used two versions of the PROSPECT model 3S and 5. The PROSPECT 3S model was adjusted to recalibrated to Norway spruce needles by Malenovský et al. (2006) and it calculates leaf reflectance (HDRF) and transmittance (HTRF) in the range from 450 to 1000 nm as functions of four input parameters: Cab, Cw, Cm, and N. The PROSPECT 5 model differs in the reflectance (HDRF) range from 400 to 2500 nm and number of input parameters: Cab, Car, Cm, Cw, N. (Jacquemoud & Baret 1990; Feret et al. 2008).

2.2.2 DART

The DART model simulates the radiative budget and RS data (images of radiometers, LiDAR waveforms, snd photon counting) of any Earth scene (natural/urban, with/without relief) for any sun direction, atmosphere and viewing direction in optical and thermal domain (CESBIO 2015, Gastellu-Etchegorry et al. 2015, Figure 2.2). The DART model is able to simulate detailed complex scenes with 3D objects and is able to simulate RS images, therefore it was chosen for simulating spruce forest scenes for this thesis. Part of this section was adapted from Jones & Vaughan (2010).

The canopy simulated in the DART model is divided into a rectangular cell matrix, and the radiation transfer is restricted to propagate in a finite number of directions with some simplified assumptions. The scene consists of parallel-piped cells, each of which may contain different components of the landscape (e.g.,leaves, grass, water, soil). Their optical properties are represented by individual scattering phase functions and structural characteristics of elements within the cell. Radiative transfer is simulated with the exact kernel and discrete ordinate approaches.

Mathematically, the radiative transfer equation for steady state monochromatic radiance $I(\mathbf{r}, \Omega)$ at a position $\mathbf{r}$ along a direction Ω_{ij} in 3D Cartesian geometry is given by

$$\left[\mu_{ij} \frac{d}{dz} + \eta_{ij} \frac{d}{dy} + \zeta_{ij} \frac{d}{dx} \right] I(\mathbf{r}, \Omega_{ij}) =$$
$$= -\alpha(\mathbf{r}, \Omega_{ij}) I(\mathbf{r}, \Omega_{ij}) + \mathfrak{Q}(\mathbf{r}, \Omega_{ij}) + \sum_{u=1}^{U} \sum_{v=1}^{V} C_{uv} \alpha_d(\mathbf{r}, \Omega_{uv} \to \Omega_{ij}) I(\mathbf{r}, \Omega_{uv}), \qquad (2.47)$$

where μ, η, and ζ are directional cosines with respect to the z, y, and x axes, the angular dependence is approximated by discretizing the angular variable Ω into a number of discrete directions Ω_{ij}, α and α_d are the extinction coefficient and differential scattering coefficient, and $\mathfrak{Q}$ is the first scattering source term. In equation 2.47, C_{uv} represents the integration weight (note that the last term is an integration kernel).
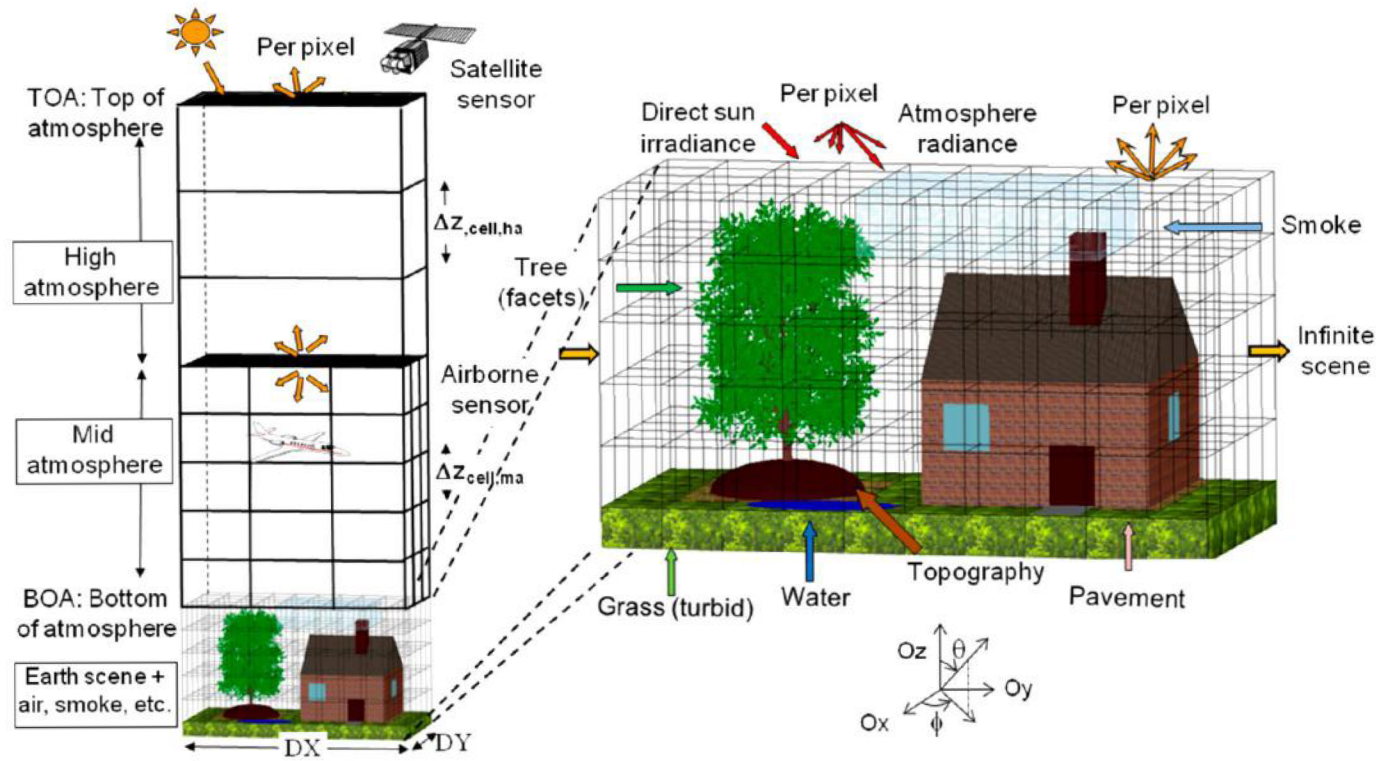
Figure 2.2: DART - cells matrix for Earth surface and Atmosphere (Gastellu-Etchegorry et al. 2015).

2.3   Estimation of vegetation parameters from remote sensing data

Some quantitative vegetation parameters, which are propagated in optical spectra, could be estimated with several retrieval methods from RS data. Relatively simple and widely used retrieval method of vegetation parameters is based on building a statistical relationship between a vegetation index and the vegetation parameter of interest. Nevertheless, the major drawback of the empirical approach based on vegetation indices is limited transferability of the statistical relationship to another study area, vegetation type, or different growing period, because the vegetation indices are typically tailored to a specific case study.

The physically based retrieval approaches use inversion of RTM. These methods provide more universal and robust solutions when compared to the empirical methods and have been previously successfully implemented in estimation of Cab and leaf area index (LAI). Commonly employed inversion methods include direct iterative optimization, inversions of look-up-tables (LUT), and machine learning algorithms.

The direct iterative optimization uses an iterative numerical approach to find values of the RTM input variables. It optimizes a cost function, while satisfying a set of prior constraints. This approach is computationally and time demanding as the RTM must be run at each iteration. Hence, it is not suitable for inversion of complex RTMs or for spectrally and spatially large RT datasets.

More computationally efficient than iterative optimization is the LUT inversion. LUTs are databases of reflectance (bidirectional reflectance factor - BRF) simulated specifically for a set of canopy biochemical and biophysical variables. RTM computes all possible combinations of input parameters and results are saved to LUT. Then values of a cost function between simulated and measured reflectance (BRF) values are calculated. The LUT is aligned ascending or descending according to the cost function, which allows to find a global solution. The cost function represents a distance between simulated (BRF_{LUT}) and observed (BRF_{OBS}) reflectance (BRF) values in a given wavelength λ. Classic example of a simple cost function is root mean square error (RMSE), which is often used in RS. The relationship between input parameters and simulated reflectance (BRF) is often nonlinear, which is in conflict of basic prerequisite for RMSE serving as cost function (Leonenko et al. 2013). Due to this fact Leonenko et al. (2013) and Rivera et al. (2013) tested different cost functions. Results of both studies suggest, that alternative cost functions provide better and more consistent results for vegetation parameters estimation.

The main problem of the LUT-based inversions is their mathematically ill-posed nature, when a given solution might not be the only one, but other sets of input parameters result in almost identical spectral outputs (Combal et al., 2002). to alleviate the ill-posed problem, some prior knowledge about the site-specific parameters is needed. One way is to limit input parameters only to possible values interval (Combal et al. 2002). Another way is using the additional radiometric information of neighboring pixels (Atzberger 2004; Houborg et al. 2009; Laurent et al. 2013). Other possible solutions how to stabilize inversion results are to choose optimal LUT size (Weiss et al. 2000). Where only one best solution are not take into account, but an average of n is taken as best solutions (Weiss et al. 2000; Darvishzadeh et al. 2012; Rivera et al. 2013). Also it is possible to take into account only the key spectral regions, which do not correlate with each other (Schlerf & Atzberger 2006; Darvishzadeh et al. 2012).

Use of modern machine learning methods for retrieval of vegetation parameters is increasing lately. Machine learning is a prolific field of research, producing algorithms that are able to cope with strong nonlinearity and high dimensionality of the data. They typically use RTM simulated LUTs for training to build a non-parametric statistical inversion model (Schlerf & Atzberger 2006; Verrelst a kol. 2012a). Among the most popular machine learning methods are artificial neural networks and support vector machines (SVM). Even more recent methods, such as kernel

26

ridge regression and Gaussian process regression (Verrelst et al., 2012b), showed promising results in terms of performance of retrieval and computing efficiency.

This section was adopted from Homolová et al. (2015b).

2.3.1 Remote sensing data

RS brings together a wide range of discipline, including physics, maths, and computing as well as the environmental sciences and biology (Jones & Vaughan 2010). In this section terms used in this thesis are briefly introduced. Most of the RS theory was adapted from Jones & Vaughan (2010) and Liang (2005).

Electromagnetic radiation is a form of energy, ranging from low-energy radio waves to high-energy γ-rays. Other forms of energy exist, such as chemical, mechanical, sound,nuclear, etc., and although the total amount of energy must stay constant in any process (low of conservation of energy), each type can be converted one into another. Different wavelengths may be absorbed by a substance depending on the physical or chemical properties of that substance.

Electromagnetic radiation consists of time-varying electric and magnetic field that travel in the form of wave at the speed of light.

Wavelength λ, measured in meters, is called a distance between adjacent wave crests.

Frequency f, measured in cycles (oscillations) per second or Hertz (Hz), is called a number of waves that pass a given point in one second.

In nature, electromagnetic waves of all frequencies and wavelengths can exist, and it is these parameters that distinguish the different type, such as VIS light, X-rays, and radio waves. The continuum is referred to as the *electromagnetic spectrum*. Because the speed of all electromagnetic wave, c, is constant and independent of wavelength, we can relate the frequency, f and wavelength λ by

$$\lambda f = c \quad \text{or} \quad \lambda = \frac{c}{f}. \tag{2.48}$$

The spectrum is usually divided up into regions (Figure 2.3), as VIS, to which the human eye responds, ultra violet, near infrared (NIR from 700 nm to 1 μm), the mid-infrared ($1 - 4$ μm), and the thermal infrared ($4 - 15$ μm).

When radiation reflected from a surface is measured, it is actually measured a *spectral radiance* L (= the radiant flux density reflected from the surface measured per area per solid angle; $W\,m^{-2}\,sr^{-1}\,nm^{-1}$).

The *solid angle* Ω is defined as the ratio of the area A of a spherical surface intercepted by the cone to the square of the radius (r)

$$\Omega = \frac{A}{r^2} \; [\text{sr}] \tag{2.49}$$

a solid angle is often represented by the zenith (θ) and azimuth (ϕ) angles (Figure 2.4) in polar coordinates. If θ represents the zenith angle (the angle measured from the vertical or from horizontal to a surface), ϕ represents the azimuth angle, then a differential element of a solid angle is mathematically given by

$$d\Omega = \frac{dA}{r^2} = \frac{(r\,d\theta)(r\,sin\,\theta\,d\phi)}{r^2} = sin\,\theta\,d\theta\,d\phi = d\mu\,d\phi, \tag{2.50}$$

here $\mu = cos\,\theta$. Note that zenith angle θ ranges from 0° to 90°. The azimuth angle ϕ ranges from 0° to 360°, that is, $0 \leq \phi \leq 2\pi$.
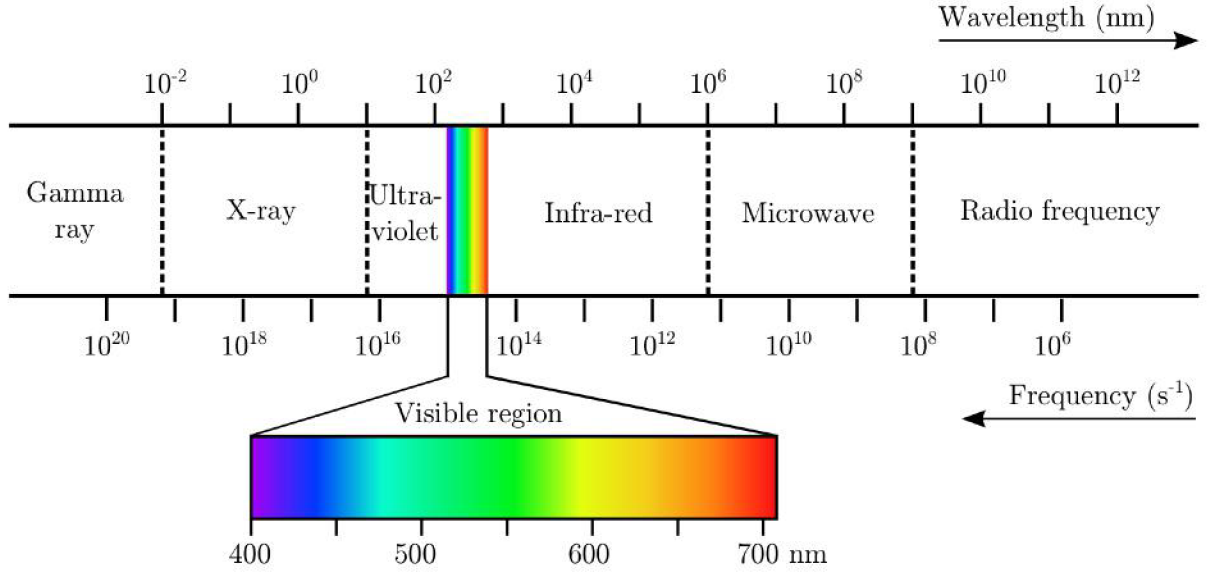
Figure 2.3: The electromagnetic spectrum (adopted from Homolová et al. 2014)
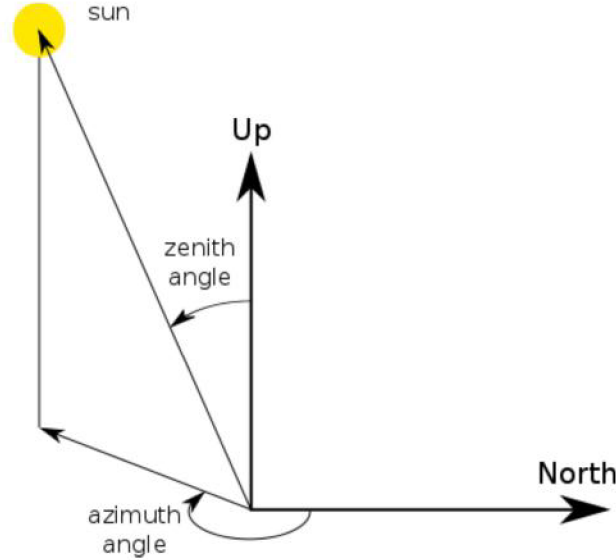
Figure 2.4: Illustration of zenith and azimuth angle.

Irradiance (E) is the integration of radiance (L) over the entire solid angle of a hemisphere consisting of the zenith angle θ and the azimuth angle ϕ:

$$E = \int\limits_{0}^{2\pi} \int\limits_{0}^{\frac{\pi}{2}} L(\theta, \phi) cos\,\theta\, sin\,\theta\, d\theta d\phi = \int\limits_{0}^{2\pi} \int\limits_{0}^{1} L(\mu, \phi)\mu\, d\mu\, d\phi \qquad (2.51)$$

If radiance is independent of the direction (isotropic), equation 2.51 becomes $E = \pi L$.

Upwelling radiance received by the Earth-viewing sensors depends on the incoming solar radiation. To normalize the variation of the incoming solar radiation, the top-of-atmosphere radiance $I(\theta_v, \phi_v)$ at the specific viewing direction (θ_v, ϕ_v) is often further converted to into reflectance

$$R(\theta_i, \phi_i, \theta_v, \phi_v) = \frac{\pi I(\theta_i, \phi_i, \theta_v, \phi_v)}{cos\,\theta_i E_0}, \qquad (2.52)$$

28

where θ_i is the solar zenith angle and E_0 is the incoming top-of-atmosphere irradiance.

Reflectance is the ratio of the reflected to the incoming radiation. The reflectance can be defined in a number of ways depending on the illumination and viewing angles and whether these are directional (restricted to a small solid angle) or hemispherical (integrating over whole hemisphere). The terminology involved in description of reflectance is summarized below (in details can be found in Schaepman-Strub et al. 2006).

Directional reflectances are usually defined by stating first the degree of collimation of the source followed by that of the detector.

Directional-directional (bidirectional) reflectance factor (BRF) when both the illuminating and viewing angles are infinitesimally small.

Hemispherical-directional reflectance factor (HDRF), when the illumination comes from the hemisphere and the sensor has an infinitesimally small view angle. For canopies this is approximated by the scattering of the diffuse component of sky radiation to a sensor. Of course the value depends on the directional distribution of incoming radiation.

As sensors and illuminators such as the sun generally have finite acceptance angles we should strictly replace the term "directional" with "conical" (giving, e.g., a biconical reflectance, see Schaepman-Strub et al. 2006), but directional is in common use (Jones & Vaughan 2010).

Band width of spectral responses are usually expressed as the full width at half maximum (Figure 2.5). The central wavelength of a spectral band responds to the maximum value of the response function (Liang 2005).

Figure 2.5: Illustration of full width half at maximum and spectral sampling interval (adopted from Homolová et al. 2014)

2.3.2 Vegetation parameters

Some vegetation parameters can be retrieved from RS data and those parameters typically refer to the current health (fitness) status of examined vegetation canopies. This thesis focuses on two vegetation parameters, Cab and LAI, and their definitions are given below.

Leaf chlorophyll a+b content (Cab)

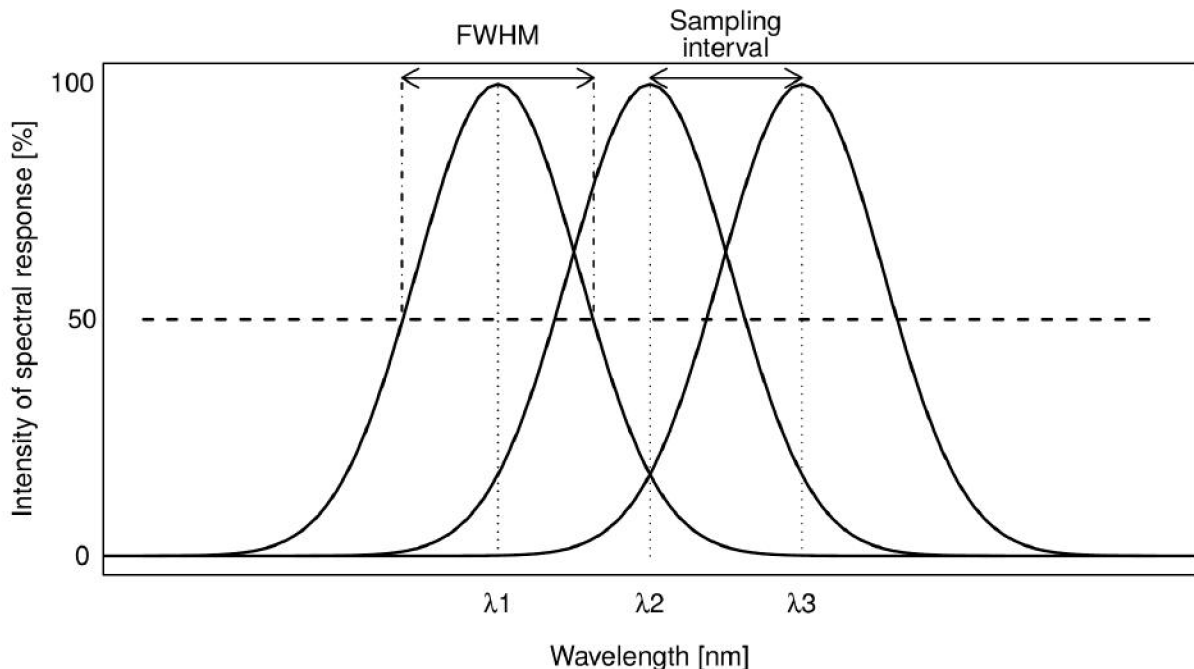Cab is the mass of chlorophyll-a and chlorophyll-b photosynthetic active pigments per unit of leaf area. Cab units are μg of chlorophylls per cm^2 of leaf area [$\mu g\, cm^{-2}$]. Laboratory measured Cab of plant leaves is typically between 10 and 100 $\mu g\, cm^{-2}$.

Leaf Area Index (LAI)

The LAI drives the microclimate of canopy, controls water interception, radiation extinction, and gas exchange (Bréda 2003), therefore, the LAI is an important input parameter for the ecological and plant physiology models (Nikolov & Zeller 2003). The LAI is a dimensionless variable that is defined as a half of the total area of photosynthetic tissue per unit ground surface area (Watson 1947). This definition is fully applicable for broadleaf vegetation because both sides of broad leaves have the same area. The needles of coniferous trees may have in a cylindrical or a hemi-cylindrical shape (Chen & Black 1992), and the definition of the LAI is not applicable. Thus several authors proposed adjusted definition of the LAI, taking into account the irregular shape of leaves or needles. For instance Chen & Black (1992) suggested as a more appropriated definition of the LAI for coniferous canopies: half of the total interception area per a unit ground surface area. In-situ measured LAI ranges typically between 0 and 10. This section was adopted from Homolová (2005).

2.3.3 Linear programming

Linear programming is a basic tool for machine learning approaches for estimating of vegetation parameters. Therefore basic terms of this theory are introduced in this sections for better explanation of support vector machines (SVM) theory in Section 2.3.4. The theory was adopted from Ferguson (2015).

   A linear programming problem may be defined as the problem of maximizing or minimizing a linear function subject to linear constraints. The constraints may be equalities or inequalities. Here is a simple example.

   Find numbers x_1 and x_2 that maximize the sum $x_1 + x_2$ subject to the constraints $x_1 \geq 0$, $x_2 \geq 0$, and

$$
\begin{aligned}
x_1 + 2x_2 &\leq 4 \\
4x_1 + 2x_2 &\leq 12 \\
-x_1 + x_2 &\leq 1
\end{aligned}
\tag{2.53}
$$

in this problem there are two unknowns, and five constraints. All the constraints are inequalities and they are all linear in the sense that each involves an inequality in some linear function of the variables. The first two constraints, $x_1 \geq 0$ and $x_2 \geq 0$, are special. These are called *nonnegativity constraints* and are often found in linear programming problems. The other constraints are then called the *main constraints*. The function to be maximized (or minimized) is called the *objective function*. Here, the objective function is $x_1 + x_2$.

Not all linear programming problems are so easily solved. There may be many variables and many constraints. Some variables may be constrained to be nonnegative and others unconstrained. Some of the main constraints may be equalities and others inequalities. However, two classes of problems, called the *standard maximum problem* and the *standard minimum problem*, play a special role. In these problems, all variables are constrained to be nonnegative, and all main constraints are inequalities.

We given an m-vector, $\mathbf{b} = (b_1, \ldots, b_m)^T$, an n-vector, $\mathbf{c} = (c_1, \ldots, c_n)^T$, and an $m \times n$ matrix,

$$\mathbf{A} = \begin{pmatrix} a_{11} & a_{12} & \cdots & a_{1n} \\ a_{21} & a_{22} & \cdots & a_{2n} \\ \vdots & \vdots & \ddots & \vdots \\ a_{m1} & a_{m2} & \cdots & a_{mn} \end{pmatrix} \tag{2.54}$$

of real numbers.

The Standard Maximum Problem: Find an n-vector , $\mathbf{x} = (x_1, \ldots, x_n)^T$, to maximize

$$\mathbf{c}^T \mathbf{x} = c_1 x_1 + \cdots + c_n x_n \tag{2.55}$$

subject to the constraints

$$\begin{aligned} a_{11} x_1 + a_{12} x_2 + \cdots + a_{1n} x_n &\leq b_1 \\ a_{21} x_1 + a_{22} x_2 + \cdots + a_{2n} x_n &\leq b_2 \\ &\vdots \\ a_{m1} x_1 + a_{m2} x_2 + \cdots + a_{mn} x_n &\leq b_m \end{aligned} \qquad (\text{or } \mathbf{Ax} \leq \mathbf{b}) \tag{2.56}$$

and

$$x_1 \geq 0,\ x_2 \geq 0, \ldots x_n \geq 0 \quad (\text{or } \mathbf{x} \geq \mathbf{0}). \tag{2.57}$$

The Standard Minimum Problem: Find an m-vector , $\mathbf{y} = (y_1, \ldots, y_m)$, to minimize

$$\mathbf{y}^T \mathbf{b} = y_1 b_1 + \cdots + y_m b_m \tag{2.58}$$

subject to the constraints

$$\begin{aligned} y_1 a_{11} + y_2 a_{21} + \cdots + y_m a_{m1} &\geq c_1 \\ y_1 a_{12} + y_2 a_{22} + \cdots + y_m a_{m2} &\geq c_2 \\ &\vdots \\ y_1 a_{1n} + y_2 a_{2n} + \cdots + y_m a_{mn} &\geq c_n \end{aligned} \qquad (\text{or } \mathbf{y}^T \mathbf{A} \geq \mathbf{c}^T) \tag{2.59}$$

and

$$y_1 \geq 0,\ y_2 \geq 0, \ldots y_m \geq 0 \quad (\text{or } \mathbf{y} \geq \mathbf{0}). \tag{2.60}$$

A vector, $\mathbf{x}$ for the standard maximum problem or $\mathbf{y}$ for the standard minimum problem, is said to be *feasible* if it satisfies the corresponding constraints.

The set of feasible vectors is called the *constraint set*.

A linear programming problem is said to be *feasible* if the constraints set is nit empty; otherwise it is said to be *infeasible*.

A feasible maximum (resp. minimum) problem is said to be *unbounded* if the objective function can assume arbitrarily large positive (rep. negative) values at feasible vectors; otherwise, it is said to be *bounded*. Thus there are three possibilities for a linear programming problem. It may be bounded feasible, it may be unbounded feasible, and it may be infeasible.

The *value* of a bounded feasible maximum (resp. minimum) problem is the maximum (resp. minimum) value of the objective function as the variables range over the constraint set.

A feasible vector at which the objective function achieves the value is called *optimal*.

Duality

To every linear program there is a dual linear program with which it is intimately connected. We first state this duality for the standard programs. As above, $\mathbf{c}$ and $\mathbf{x}$ are n-vectors, $\mathbf{b}$ and $\mathbf{y}$ are m-vectors, and $\mathbf{A}$ is an $m \times n$ matrix. We assume $m \geq 1$ and $n \geq 1$.

Definition 2.3.1. The *dual* of the standard maximum problem

$$
\begin{aligned}
&\text{maximize } \mathbf{c}^T\mathbf{x} \\
&\text{subject to the constraints } \mathbf{Ax} \leq \mathbf{b} \text{ and } \mathbf{x} \geq 0
\end{aligned}
\tag{2.61}
$$

is the standard minimum problem

$$
\begin{aligned}
&\text{minimize } \mathbf{y}^T\mathbf{b} \\
&\text{subject to the constraints } \mathbf{y}^T\mathbf{A} \geq \mathbf{c}^T \text{ and } \mathbf{y} \geq 0
\end{aligned}
\tag{2.62}
$$

If the standard minimum problem 2.62 is transformed into a standard maximum problem (by multiplying $\mathbf{A}$, $\mathbf{b}$, and $\mathbf{c}$ by -1), its dual by the definition above is a standard minimum problem which, when transformed to a standard maximum problem (again by changing the signs of all coefficients) becomes exactly 2.61. Therefore, the dual of the standard minimum problem 2.62 is the standard maximum problem 2.61. The problems 2.61 and 2.62 are said ti be duals.

The general standard maximum problem and the dual standard minimum problem may be simultaneously exhibited in the display:

$$
\begin{array}{c|cccc|c}
 & x_1 & x_2 & \cdots & x_n & \\
\hline
y_1 & a_{11} & a_{12} & \cdots & a_{1n} & \leq b_1 \\
y_2 & a_{21} & a_{22} & \cdots & a_{2n} & \leq b_2 \\
\vdots & \vdots & \vdots & & \vdots & \vdots \\
y_m & a_{m1} & a_{m2} & \cdots & a_{mn} & \leq b_m \\
\hline
 & \geq c_1 & \geq c_2 & \cdots & \geq c_n &
\end{array}
\tag{2.63}
$$

2.3.4 Support vector machines

Support Vector Machines (SVMs) and related kernel methods have become increasingly popular tools for data mining tasks such as classification, regression, and novelty detection (Bennet & Campbell 2000).

In this study is used library `LIBSVM` prepared and actively developing by Chang C.-C. & Lin C.-J. Therefore for description of used SVM methods are used document of authors of this library (Chang & Lin 2011).

2.3.4.1   C-Support Vector Classification

Given training vectors $\mathbf{x}_i \in R^n$, $i = 1, \ldots, l$, in two classes, and an indicator vector $\mathbf{y} \in R^l$ such that $y_i \in \{1, -1\}$, C-SVC (Boser et al. 1992, Cortes and Vapnik 1995) solves the following primal optimization problem.

$$
\begin{aligned}
\min_{\mathbf{w}, b, \boldsymbol{\xi}} \quad & \frac{1}{2}\mathbf{w}^T\mathbf{w} + C\sum_{i=1}^{l}\xi_i \\
\text{subject to} \quad & y_i(\mathbf{w}^T\phi(\mathbf{x}_i) + b) \geq 1 - \xi_i, \\
& \xi_i \geq 0,\ i = 1, \ldots, l,
\end{aligned}
\tag{2.64}
$$

where $\phi(\mathbf{x}_i)$ maps $\mathbf{x}_i$ into a higher -dimensional space $C > 0$ is the regularization parameter. Due to the possible high dimensionality of the vector variable $\mathbf{w}$, usually we solve the following dual problem.

$$
\begin{aligned}
\min_{\boldsymbol{\alpha}} \quad & \frac{1}{2}\boldsymbol{\alpha}^T Q\boldsymbol{\alpha} - \mathbf{e}^T\boldsymbol{\alpha} \\
\text{subject to} \quad & \mathbf{y}^T\boldsymbol{\alpha} = 0, \\
& 0 \leq \alpha_i \leq C, \quad i = 1, \ldots, l,
\end{aligned}
\tag{2.65}
$$

where $\mathbf{e} = (1, .., 1)^T$ is the vector of all ones, Q is an l by l positive semidefinite matrix, $Q_{ij} \equiv y_i y_j K(\mathbf{x}_i, \mathbf{x}_j)$, and $K(\mathbf{x}_i, \mathbf{x}_j) \equiv \phi(\mathbf{x}_i)^T\phi(\mathbf{x}_j)$ is the kernel function.

After problem 2.65 is solved, using the primal-dual relationship, the optimal $\mathbf{w}$ satisfies

$$
\mathbf{w} = \sum_{i=1}^{l} y_i \alpha_i \phi(\mathbf{x}_i)
\tag{2.66}
$$

and the decision function is

$$
\text{sgn}(\mathbf{w}^T\phi(\mathbf{x}) + b) = \text{sgn}\left(\sum_{i=1}^{l} y_i \alpha_i K(\mathbf{x}_i, \mathbf{x}) + b\right).
\tag{2.67}
$$

2.3.4.2 ν - Support Vector Classification

The ν - Support Vector Classification (Schölkopf et al. 2000) introduces a new parameter $\nu \in (0, 1\rangle$. It is proved that ν an upper bound on the fraction of training errors and a lower bound of the fraction of support vectors.

Given training vectors $\mathbf{x}_i \in R^n$, $i = 1, \ldots, l$, in two classes, and a vector $\mathbf{y} \in R^l$ such that $y_i \in \{1, -1\}$, the primal optimization problem is

$$
\begin{aligned}
\min_{\mathbf{w}, b, \boldsymbol{\xi}, \rho} \quad & \frac{1}{2}\mathbf{w}^T\mathbf{w} - \nu\rho + \frac{1}{l}\sum_{i=1}^{l}\xi_i \\
\text{subject to} \quad & y_i(\mathbf{w}^T\phi(\mathbf{x}_i) + b) \geq \rho - \xi_i, \\
& \xi_i \geq 0,\ i = 1, \ldots, l, \quad \rho \geq 0.
\end{aligned}
\tag{2.68}
$$

the dual problem is

$$\min_{\boldsymbol{\alpha}} \quad \frac{1}{2}\boldsymbol{\alpha}^T Q \boldsymbol{\alpha}$$

$$\text{subject to} \quad 0 \leq \alpha_i \leq \frac{1}{l}, \quad i = 1, \ldots, l, \tag{2.69}$$

$$\mathbf{e}^T \boldsymbol{\alpha} \geq \nu, \quad \mathbf{y}^T \boldsymbol{\alpha} = 0,$$

where $Q_{ij} = y_i y_j K(\mathbf{x}_i, \mathbf{x}_j)$. Chang & Lin (2001) show that problem 2.69 is feasible if and only if

$$\nu \leq \frac{2\min(\#y_i = +1, \#y_i = -1)}{l} \leq 1, \tag{2.70}$$

so the usable range of ν is smaller than $(0, 1\rangle$.

The decision function is

$$\text{sgn}\left(\sum_{i=1}^{l} y_i \alpha_i K(\mathbf{x}_i, \mathbf{x}) + b\right). \tag{2.71}$$

It is shown that $\mathbf{e}^T \boldsymbol{\alpha} \geq \nu$ can be replaced by $\mathbf{e}^T \boldsymbol{\alpha} = \nu$ (Crisp & Burges 1999, Chang & Lin 2001). In `LIBSVM`, is solved a scaled version of problem 2.69 because numerically α_i may be too small due to the constraint $\alpha_i \leq \frac{1}{l}$.

$$\min_{\overline{\boldsymbol{\alpha}}} \quad \frac{1}{2}\overline{\boldsymbol{\alpha}}^T Q \overline{\boldsymbol{\alpha}}$$

$$\text{subject to} \quad 0 \leq \overline{\alpha}_i \leq 1, \quad i = 1, \ldots, l, \tag{2.72}$$

$$\mathbf{e}^T \overline{\boldsymbol{\alpha}} = \nu l, \quad \mathbf{y}^T \overline{\boldsymbol{\alpha}} = 0.$$

If $\boldsymbol{\alpha}$ is optimal for the dual problem 2.69 and ρ is optimal for the primal problem 2.68, Chang & Lin (2001) show that $\frac{\boldsymbol{\alpha}}{\rho}$ is an optimal solution of C-SVM with $C = \frac{1}{(\rho l)}$. Thus, in `LIBSVM`, we output $(\frac{\boldsymbol{\alpha}}{\rho}, \frac{b}{\rho})$ in the model. More precisely, solving 2.72 obtains $\overline{\rho} = \rho l$. Because $\overline{\boldsymbol{\alpha}} = l\boldsymbol{\alpha}$, we have $\frac{\boldsymbol{\alpha}}{\rho} = \frac{\overline{\boldsymbol{\alpha}}}{\overline{\rho}}$. Hence, in `IBSVM`, we calculate $\frac{\overline{\boldsymbol{\alpha}}}{\overline{\rho}}$.

2.3.4.3 Distribution Estimation (One-class SVM)

One-class SVM was proposed by Schölkopf et al. (2001) for estimating the support of a high-dimensional distribution. Given training vectors $\mathbf{x}_i \in R^n, i = 1, \ldots, l$ without any class information, the primal problem of one-class SVM is

$$\min_{\mathbf{w}, \boldsymbol{\xi}, \rho} \quad \frac{1}{2}\mathbf{w}^T\mathbf{w} - \rho + \frac{1}{\nu l}\sum_{i=1}^{l}\xi_i$$

$$\text{subject to} \quad \mathbf{w}^T\phi(\mathbf{x}_i) \geq \rho - \xi_i, \tag{2.73}$$

$$\xi_i \geq 0, \ i = 1, \ldots, l.$$

the dual problem is

$$\min_{\boldsymbol{\alpha}} \quad \frac{1}{2}\boldsymbol{\alpha}^T Q \boldsymbol{\alpha}$$
$$\text{subject to} \quad 0 \le \alpha_i \le \frac{1}{(\nu l)}, \quad i = 1,\dots,l, \tag{2.74}$$
$$\mathbf{e}^T\boldsymbol{\alpha} = 1,$$

where $Q_{ij} = K(\mathbf{x}_i,\mathbf{x}_j) = \phi(\mathbf{x}_i)^T\phi(\mathbf{x}_j)$. The decision function is

$$\text{sgn}\left(\sum_{i=1}^{l}\alpha_i K(\mathbf{x}_i,\mathbf{x}) - \rho\right). \tag{2.75}$$

Similar to the case of ν-SVC, in `LIBSVM`, we solve a scaled version of 2.74.

$$\min_{\boldsymbol{\alpha}} \quad \frac{1}{2}\boldsymbol{\alpha}^T Q \boldsymbol{\alpha}$$
$$\text{subject to} \quad 0 \le \alpha_i \le 1, \quad i = 1,\dots,l, \tag{2.76}$$
$$\mathbf{e}^T\boldsymbol{\alpha} = \nu l.$$

2.3.4.4 ϵ - Support Vector Regression (ϵ-SVR)

Consider a set of training points, $\{(\mathbf{x}_1,z_1),\dots,(\mathbf{x}_l,z_l)\}$, where $\mathbf{x}_i \in R^n$ is a feature vector and $z_i \in R^1$ is the target output. Under given parameters $C > 0$ and $\epsilon > 0$, the standard form of support vector regression (Vapnik 1998) is

$$\min_{\mathbf{w},b,\boldsymbol{\xi},\boldsymbol{\xi}^*} \quad \frac{1}{2}\mathbf{w}^T\mathbf{w} + C\sum_{i=1}^{l}\xi_i + C\sum_{i=1}^{l}\xi_i^*$$
$$\text{subject to} \quad \mathbf{w}^T\phi(\mathbf{x}_i) + b - z_i \le \epsilon + \xi_i, \tag{2.77}$$
$$z_i - \mathbf{w}^T\phi(\mathbf{x}_i) - b \le \epsilon + \xi_i^*,$$
$$\xi_i, \xi_i^* \ge 0,\, i = 1,\dots,l.$$

the dual problem is

$$\min_{\boldsymbol{\alpha},\boldsymbol{\alpha}^*} \quad \frac{1}{2}(\boldsymbol{\alpha} - \boldsymbol{\alpha}^*)^T Q(\boldsymbol{\alpha} - \boldsymbol{\alpha}^*) + \epsilon\sum_{i=1}^{l}(\alpha_i + \alpha_i^*) + \sum_{i=1}^{l}z_i(\alpha_i - \alpha_i^*)$$
$$\text{subject to} \quad \mathbf{e}^T(\boldsymbol{\alpha} - \boldsymbol{\alpha}^*) = 0, \tag{2.78}$$
$$0 \le \alpha_i, \alpha_i^* \le C, \quad i = 1,\dots,l,$$

where $Q_{ij} = K(\mathbf{x}_i,\mathbf{x}_j) \equiv \phi(\mathbf{x}_i)^T\phi(\mathbf{x}_j)$.

After solving problem 2.78, the approximate function is

$$\sum_{i=1}^{l}(-\alpha_i + \alpha_i^*)K(\mathbf{x}_i,\mathbf{x}) + b \tag{2.79}$$

2.3.4.5 ν - Support Vector Regression (ν-SVR)

Similar to ν-SVC, for regression, Schölkopf et al. (2000) use a parameter $\nu \in (o,1\rangle$ to control the number of support vectors. The parameter ϵ in ϵ-SVR becomes a parameter here. With (C,ν) as parameters, ν-SVR solves

$$\min_{\mathbf{w},b,\boldsymbol{\xi},\boldsymbol{\xi}^*,\epsilon} \quad \frac{1}{2}\mathbf{w}^T\mathbf{w} + C(\nu\epsilon + \frac{1}{l}\sum_{i=1}^{l}(\xi_i + \xi_i^*))$$

$$\text{subject to} \quad (\mathbf{w}^T\phi(\mathbf{x}_i)+b) - z_i \le \epsilon + \xi_i, \tag{2.80}$$

$$z_i - (\mathbf{w}^T\phi(\mathbf{x}_i)+b) \le \epsilon + \xi_i^*,$$

$$\xi_i, \xi_i^* \ge 0,\ i=1,\dots,l,\quad \epsilon \ge 0.$$

the dual problem is

$$\min_{\boldsymbol{\alpha},\boldsymbol{\alpha}^*} \quad \frac{1}{2}(\boldsymbol{\alpha}-\boldsymbol{\alpha}^*)^T Q (\boldsymbol{\alpha}-\boldsymbol{\alpha}^*) + \mathbf{z}^T(\boldsymbol{\alpha}-\boldsymbol{\alpha}^*)$$

$$\text{subject to} \quad \mathbf{e}^T(\boldsymbol{\alpha}-\boldsymbol{\alpha}^*)=0, \mathbf{e}^T(\boldsymbol{\alpha}+\boldsymbol{\alpha}^*)\le C\nu, \tag{2.81}$$

$$0\le \alpha_i, \alpha_i^* \le \frac{C}{l},\quad i=1,\dots,l.$$

the approximate function is

$$\sum_{i=1}^{l}(-\alpha_i+\alpha_i^*)K(\mathbf{x}_i,\mathbf{x})+b. \tag{2.82}$$

Similar to ν-SVC, Chang & Lin (2002) show that the inequality $\mathbf{e}^T(\boldsymbol{\alpha}+\boldsymbol{\alpha}^*)\le C\nu$ can be replaced by an equality. Moreover, $\frac{C}{l}$ may be too small, thus, there are treated specified regularization parameter as $\frac{C}{l}$. That is, $\overline{C}=\frac{C}{l}$ is what is specified and `LIBSVM` solves following problem.

$$\min_{\boldsymbol{\alpha},\boldsymbol{\alpha}^*} \quad \frac{1}{2}(\boldsymbol{\alpha}-\boldsymbol{\alpha}^*)^T Q (\boldsymbol{\alpha}-\boldsymbol{\alpha}^*) + \mathbf{z}^T(\boldsymbol{\alpha}-\boldsymbol{\alpha}^*)$$

$$\text{subject to} \quad \mathbf{e}^T(\boldsymbol{\alpha}-\boldsymbol{\alpha}^*)=0, \mathbf{e}^T(\boldsymbol{\alpha}+\boldsymbol{\alpha}^*)=\overline{C}l\nu, \tag{2.83}$$

$$0\le \alpha_i, \alpha_i^* \le \overline{C},\quad i=1,\dots,l.$$

Chang & Lin (2002) prove that ϵ-SVR with parameters $(\overline{C},\epsilon)$ has the same solution as ν-SVR with parameters $(l\overline{C},\nu)$.

2.3.4.6 Performance measures

After solving optimization problems listed in previous sections, it can be applied decision function to predict labels (target values) of testing data. Let $\mathbf{x}_1,\dots,\mathbf{x}_{\bar{l}}$ be the testing data and $f(\mathbf{x}_1),\dots,f(\mathbf{x}_{\bar{l}})$ be decision values (target values for regression) predicted by `LIBSVM`. If true labels (true target values) of testing data are known and denoted as $y_i,\dots,y_{\bar{l}}$, we evaluate the prediction results by the following measures.

Classification

$$\text{Accuracy} = \frac{\text{number of correctly predicted data}}{\text{number of total testing data}} \times 100\%$$

Regression

A common accuracy measures are mean square error (MSE) and root mean square error (RMSE):

$$\text{MSE} = \frac{1}{\bar{l}} \sum_{i=1}^{\bar{l}} (f(\mathbf{x}_i) - y_i)^2 \qquad (2.84)$$

to return the original scale, the square root of the MSE

$$\text{RMSE} = \sqrt{\frac{1}{\bar{l}} \sum_{i=1}^{\bar{l}} (f(\mathbf{x}_i) - y_i)^2}, \qquad (2.85)$$

2.3.5 Image classification

Image classification is a fundamental tool for many RS applications where one is often interested in reducing the complexity of a remote image to a limited number of near-homogeneous classes that may represent, for example, different vegetation or landcover types. The classification of pixels into specific classes is most commonly based on recognition of their characteristics spectral signatures. Such a classification process produces a thematic map that displays the spatial distribution of a specific phenomenon such as the type of soil or agricultural crop. There are many approaches available for such pattern recognition. A more complete coverage of the principles and practice of image classification and pattern recognition in remote sensing may be found in any one of the many texts on the subject such as those by Tso and Mather (2001), Mather (2004), Jensen (2005), Richards and Xia (2005) and Russ (2006).

For purpose of this study the supervised maximum-likelihood method was chosen as a robust classification, and the one most widely used in remote sensing. Supervised classification methods start from an initial identification of certain areas or pixels from the image that are known to comprise particular vegetation or other surface types of interest for the particular study. In this case the spectral characteristics of these training pixels are first measured, and, in "conventional" approaches, a mean and variance of the probability of any pixels falling into a given training class is calculated. The software then attempts to assign the remaining pixels to the most similar (nearest) training class. When using the statistically based classifiers as maximum-likelihood it is strictly necessary that the training set contains $> n + 1$ pixels (where n is the number of spectral bands), though substantially larger numbers (of the order $10n$) are preferable to allow good estimates of the variance and covariance properties of each class.

This section was adopted form Jones & Vaughan (2010).

3 | Experimental part

3.1 Study sites

The study was conducted in Norway spruce stand at the permanent ecological research site Bílý Kříž (Moravian-Silesian Beskids) and additional datasets were acquired from the Černá hora study site (Šumava National Park). Detailed description of both research sites is provided in the following sections.

3.1.1 Bílý Kříž

The experimental ecological study site Bílý Kříž was established in 1986 within the framework of the project "Complex Research of Immission Impact on the Forests and Forestry of the Beskids". The site is located in the Moravian-Silesian Beskids Mts. (Czech Republic); geographical coordinates 49°30' N, 18°32' E (Figure 3.1), altitude 870 m a.s.l. It is operated and maintained by the CzechGlobe research institute (Czech Academy of Sciences). The Bílý Kříž site is a part of international measuring network FLUXNET. The site belongs to significant infrastructures of European Strategy Forum on Research Infrastructures and it is a part of the Integrated Carbon Observation System.

Norway spruce (*Picea abies* [L.] Karst.) stand at Bílý Kříž is the main object of this study. The stand was established in 1981 and its monitoring started in 1994. The stand is located on a south exposed slope of 12.5°. Forest stand Bílý Kříž characteristics are detailed in Table 3.1. Description of the Bílý Kříž site was adapted from Marková et al. (2015).

stand characteristics	
dominant forest species	Norway spruce (*Picea abies*)
stand age	29 years
stand density	1580 trees ha^{-1}
mean tree height	12 m
mean LAI	8 $m^2\,m^{-2}$
canopy cover	$90-95$ %

Table 3.1: Overview of the Bílý Kříž forest stand characteristics in 2006.

Figure 3.1: Locations of the Bílý Kříž (at Moravian-Silesian Beskids) and Černá hora (at Šumava National Park) sites.

3.1.2 Černá hora

The Černá hora site is located in the Šumava National Park (Czech Republic), near the Černá Hora mountain (48°58' N, 13°33' E, mean altitude 1280 m a.s.l., mean slope 7°, and prevailing SSE exposition: 157.5°) (Figure 3.1). This site has been originally selected and studied due to the extensive bark beetle outbreak. The Norway spruce (*Picea abies* [L.] Karst.) is the most frequent tree specie at this site. The forest trees are older than those of the Bílý Kříž site. More information about this stand is provided in Table 3.2.

stand characteristics	
dominant forest species	Norway spruce (*Picea abies*)
mean stand age	101 years
stand stem density	800 trees ha^{-1}
mean tree height	19 m
mean LAI	5.03 $m^2\,m^{-2}$
canopy cover	80 %

Table 3.2: Overview of the Černá hora forest stand characteristics in 2009.

3.2   Input data

3.2.1   Distribution of shoots and measurements of tree skeleton structure

Shoot distribution data available in scientific literature and terrestrial Light Detection and Ranging (LiDAR) measurements of spatial distribution of shoots in crown from study sites were used to reconstruct skeletons and foliage distribution of spruce trees in this study.

Spatial distribution of needle shoots depends on crown height and their age (Figure 3.2). The studies of Barták (1992, 1993) described the crown structure of twenty 35-years old Norway spruce (*Picea abies /L./ Karst.*) trees at the Bílý Kříž site. These studies were the only available source providing detailed information on shoot distribution, which was used for our 3D spruce reconstruction.
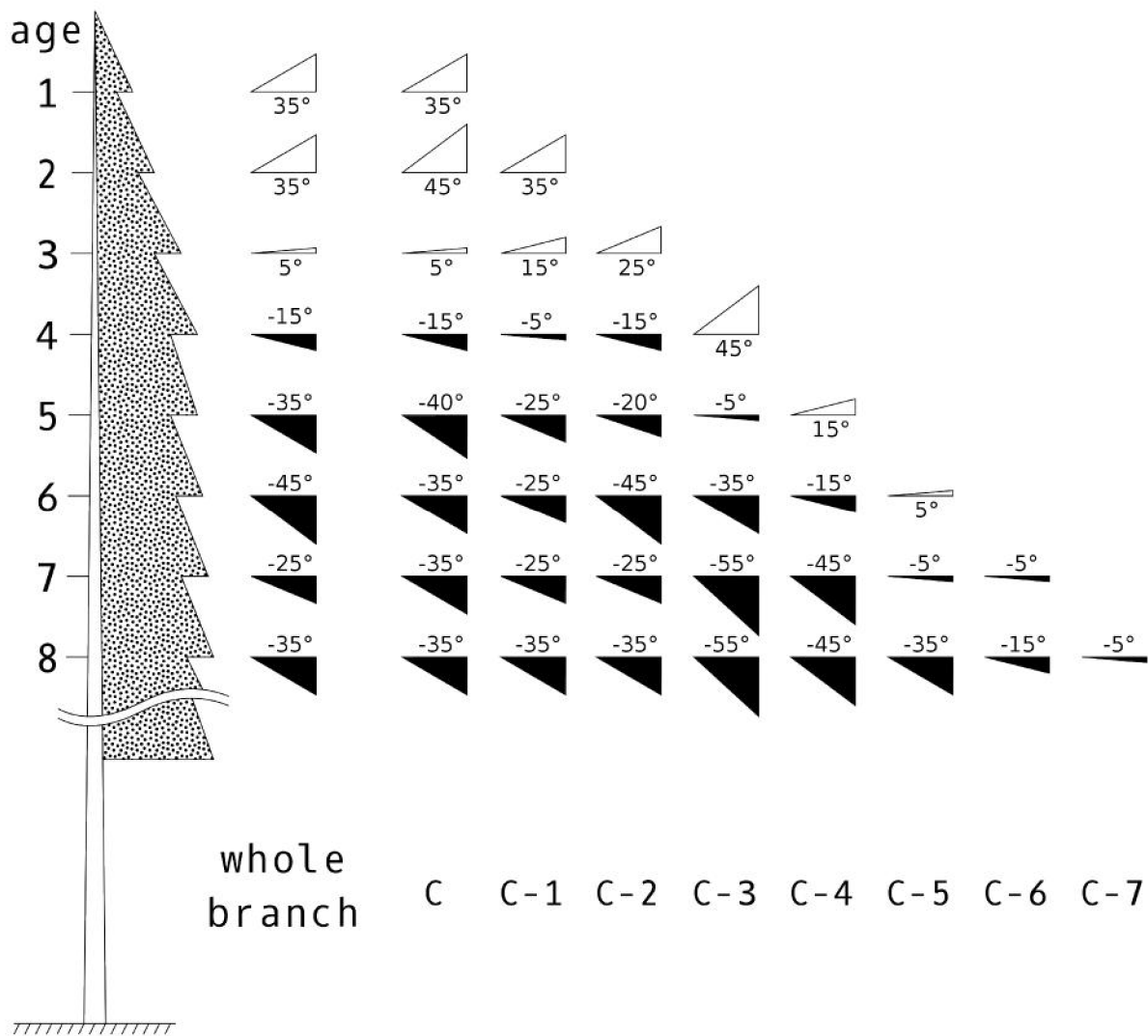

Figure 3.2: The angular distribution of shoots according to the needle age and the shoot vertical position adapted and translated from Barták (1992). The first left column represents angle in the whole branch. C means current year needles.

To create a 3D spruce model it is additionally required to define the azimuth angle of the shoots. Since this parameter was not available from Barták's studies, it was calculated as the angle between a shoot position and a trunk with added random value in range $\langle -\frac{\pi}{4}, \frac{\pi}{4} \rangle$ (see Section 3.3.3), where the predefined range values were observed in field.

The ground LiDAR data were acquired with an OPTECH Ilris-36D terrestrial laser scanner (Figure 3.3) at the Černá hora site in October 2009. The Ilris-36D LiDAR emits laser beams ($\Lambda = 1500$ nm) in various directions and measures the amount of returned laser pulse for up to 2500 points per second. The laser scanning data were acquired for individual mature spruce trees that were left standing at the edge of a bark beetle outbreak clearing. Trees were scanned from multiple directions at several locations and several observations were merged into a single common point cloud. Examples of scanned trees are given in Figure 3.4 and 3.8a.

Figure 3.3: OPTECH Ilris-36D terrestrial laser scanner.
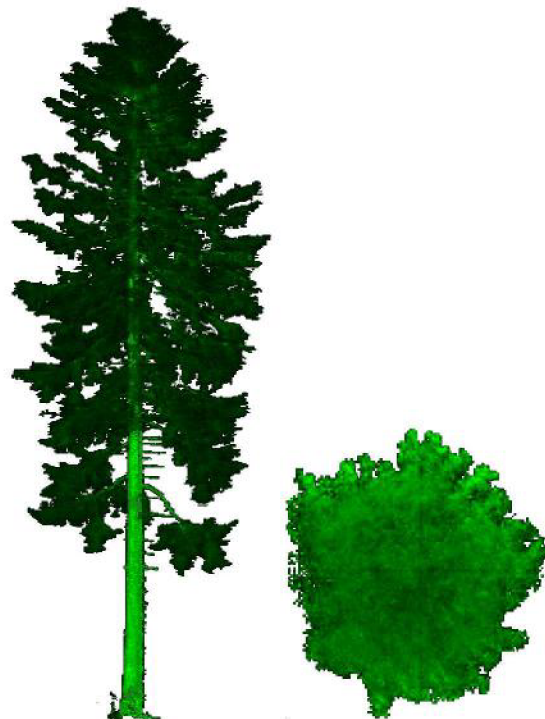
Figure 3.4: Example of terrestrial LiDAR scan of a spruce tree. Side projection on the left and top projection on the right.

The raw LiDAR data were preprocessed using PolyWorks IMSurvey software. In order to minimize mutual shadowing of branches within crowns, only half of the tree (the one facing the LiDAR scanner) was extracted from the point cloud. The foliage biomass, reflecting only about 10% of the laser intensity signal, was separated from wooden parts, having signal reflectance of about 50% intensity, using an intensity threshold between foliage and wood reflectance (Figure 3.8a and 3.8d). The threshold value was set up for each tree manually by operator. The elaboration of LiDAR data acquirement and processing was adopted from Borovička & Pazdera (2009).

The point cloud of wooden elements was subsequently used to reconstruct 3D tree skeleton structure, i.e. trunk and branches (Section 3.3.1), whereas the foliage point cloud was later used in the algorithm for biologically correct distribution of shoots of different age categories (as described in Section 3.3.3).

3.2.2 Field measurements of biochemical and biophysical properties

The forest stand optical, biochemical and biophysical properties, particularly leaf chlorophyll a+b content (Cab) and LAI that were used mainly for validation of retrievals from satellite multispectral images in 2016, were collected in September 2006 and in August 2016 (the peak) of the vegetation seasons. As such, they are compatible with airborne hyperspectral images acquired on the 14th September 2006 (Section 3.2.3) and Sentinel-2 (S2) multispectral sensor image acquired on 31th August 2016 (Section 3.2.4).

Leaf Cab samples collected and analyzed in 2006 were taken from sunlit and shaded branches of nine spruce trees distributed along a East-West oriented transect (Figure 3.5). Leaf Cab was extracted destructively in laboratory according to standard procedures described in Porra et al. (1989) and Wellburn (1994).
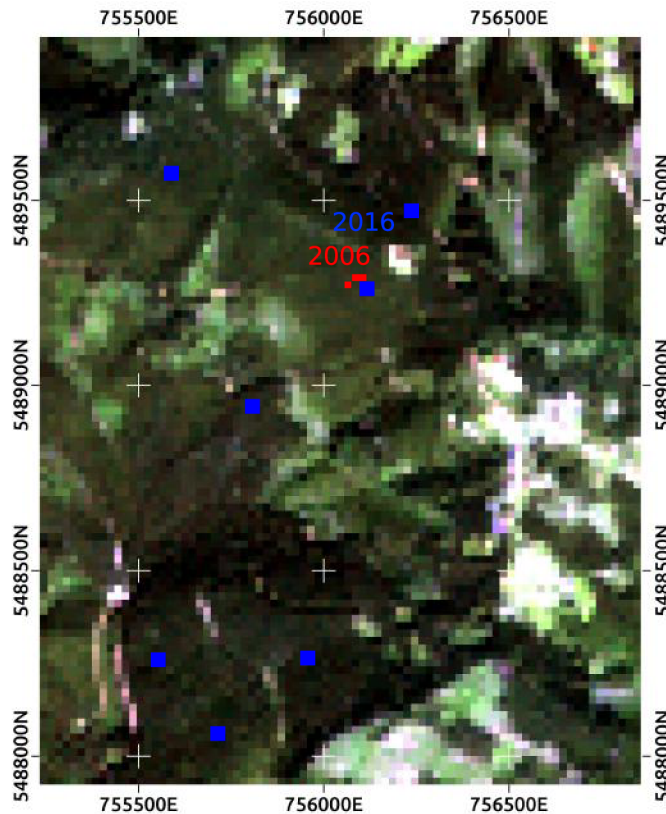
Figure 3.5: Naturally collared RGB composite of S2 multispectral image subset depicting locations of trees measured in 2006 (red) and 2016 (blue). Trees examined in 2006 occupied only three S2 pixels of $20 \times 20m$.

The samples obtained in 2016 were collected from sunlit and shaded branches of three spruce trees at seven plots (Figure 3.5). Shoots of three age categories (current, 1-year old, and 2-year old) were taken from each sampled branch. The plots were selected based on forest inventory records in the attempt to capture high variability in local biochemical and biophysical properties. The samples were processed the same way as samples from 2006.

The LAI was measured with the Plant Canopy Analyzer LAI-2000 (Li-Cor Biosciences, Inc., Lincoln, Nebraska, USA) in a regular grid of 6×6 points with distance between two points of 10 m. The LAI measurements were processed in C2000 software developed by Li-COR Biosciences. The resulting LAI values corresponded to Plant Area Index and were, therefore corrected for the inclusion of wooden material. They were also corrected for the effect of needle

clumping at the shoot level (Chen 1996). The correction coefficient α was equal to 0.133 and ε was equal to 1.526. Both values were obtained from experimental destructive analyses of spruce shoots originating from the Bílý Kříž site. The correction coefficient Ω, equal to 0.89, was derived from experimental measurements with the TRAC instrument (3 Wave Engineering, Ottawa, ON, Canada). Detailed description of the LAI measurements and data processing for the spruce site is available in Homolová et al. (2007).

The in-situ LAI data formed 9 validation points with LAI varying between 6.8 and 8.5 $m^2 m^{-2}$ in 2006. Description of the field measurements was adopted from Homolová et al. (2015b).

The LAI measured in 2016 was done on two perpendicular transects per each seven plots and the mean value from each plot is the LAI value of this plot. The LAI values per plot varying between 5 and 9 $m^2 m^{-2}$. The processing of these data was the same as in 2006.

3.2.3 AISA airborne hyperspectral data

Hyperspectral airborne data used in this study were acquired at the Bílý Kříž (Figure 3.6) with the AISA Eagle imaging system (Specim Inc.) during the peak of vegetation season 2006. Basic characteristics of the image data are summarized in Table 3.3. The airborne images were first radiometrically, geometrically and atmospherically corrected. Radiometric corrections were performed with the factory calibration coefficients embedded in the CaliGeo software (the AISA image post-processing software developed by Specim Inc.) running under the ENVI/IDL programming environment. Required geometric corrections, i.e. image orthorectification and georeferencing, were also performed in the CaliGeo software. Accuracy of geometric corrections was evaluated using the set of ground control points measured with a geodetic Global Positioning System (GPS) receiver. Declared position accuracy was about 1.0 m (around 2 – 3 pixels). Atmospheric corrections were performed in the ATCOR-4 software (Richter & Schläpfer 2002). The most crucial input parameters for atmospheric corrections, visibility (or aerosol optical thickness) and water vapor column, were estimated directly from the hyperspectral images using the SPECTRA module of ATCOR-4. Aerosol optical model was selected with the estimated visibility of 20 km and the water vapor column varying between 0.93 – 0.96 $[\mu m]$. The quality of atmospheric corrections was evaluated by means of ground reflectance measurements of seven artificial and three natural near-Lambertian spectral calibration targets, performed with an ASD FieldSpec PRO spectroradiometer. Mean difference in reflectance values was equal to 1.6 % at 550 nm and 1.8 % at 850 nm (Figure 3.6). Description of airborne data processing was adopted from Homolová et al. (2015a).

3.2.4 Sentinel-2 satellite multispectral data

The space-born data used in this study to estimate quantitative biochemical and biophysical vegetation parameters were acquired with the multispectral images on board of the EC Copernicus satellite system called S2. The satellite is a part of the Sentinel mission series operated by the European Space Agency (ESA, http://www.esa.int/ESA). Since the DART simulations produced a mean reflectance (BRF) for the scene of 10×10 m in size, multispectral bands of S2 with the pixel size of 10 and 20 m were more suitable for quantitative retrievals than airborne data with the sub-meter spatial resolution.

The multispectral satellite data at the Bílý Kříž site were acquired simultaneously with collection of field biochemical and biophysical properties (31th August 2016). Most important image data technical specifications are summarized in Table 3.4 and 3.5. The satellite data were atmospherically corrected in the S2 toolbox provided by ESA (Figure 3.7).

AISA airborne data characteristics	
acquisition date	14/09/2006
acquisition time (UTC)	$10:35 - 11:03$
number of flight lines	5
solar zenith angle	46°
solar azimuth angle	182°
flight heading	170°
flight altitude above terrain	360 m
sensor field of view	39.7°
swath width	200 m
spectral range	$391.7 - 981.6$ mm
number of bands	65
spectral sampling	$8.6 - 9.5$ nm
spatial resolution	0.4 m
geographical projection	UTM, Zone 34N

Table 3.3: Characteristics of AISA Eagle airborne hyperspectral images used in this study.

S2 satellite data characteristics	
acquisition date	31/08/2016
acquisition time (UTC)	$9:50 - 9:52$
solar zenith angle	43°
solar azimuth angle	160°
orbit height	786 km
orbit type	sun-synchronous
inclination	98.5°
swath width	290 km
number of bands	13
geographical projection	UTM, Zone 33N

Table 3.4: Characteristics of the S2 satellite multispectral images used in this study. Swath is the strip of ground beneath airborne or satellite sensor from which data are collected. The swath width is determined by the length of the scan line of the detector (Jones & Vaughan 2010).

Only a spatial and spectral subset of S2 image data, which contains all seven ground plots investigated for the Cab and LAI measurements, was used (see Section 3.2.2). The bands with too large spatial resolution (60 m) and with broad spectral bandwidth were excluded from the subset. The final collection contained the following selected S2 bands: B2, B3, B4, B5, B6, B7, B8a, B11, and B12 (Table 3.5).
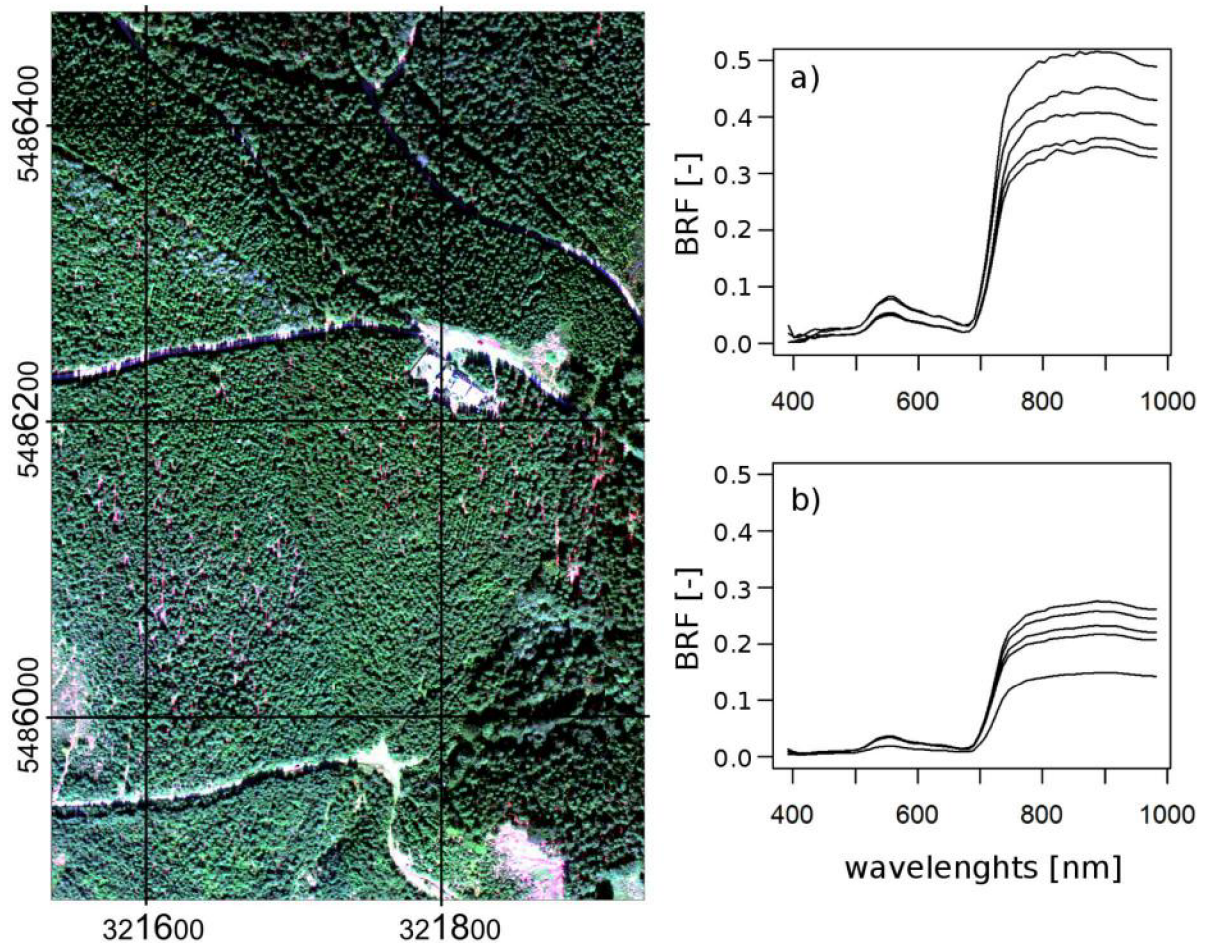
Figure 3.6: Georeferenced RGB composite in natural colors for the AISA Eagle hyperspectral image of the Bílý Kříž site acquired in 2006 (spatial resolution of 0.4 m, 65 spectral bands with spectral sampling distance of about 9 nm projected in UTM Zone 34N (WGS 84)). The right graphs show spectral reflectance (BRF) signatures of five randomly selected a) spruce crowns and b) aggregated areas of 20 x 20 m (adopted from Homolová et al. 2015a).

band ID	central wavelength [nm]	bandwidth [nm]	spatial resolution [m]
B1	443	20	60
B2	490	65	10
B3	560	35	10
B4	665	30	10
B5	705	15	20
B6	740	15	20
B7	783	20	20
B8	842	115	10
B8a	865	20	20
B9	945	20	60
B10	1375	30	60
B11	1610	90	20
B12	2190	180	20

Table 3.5: The central wavelengths, bandwidths, and spatial resolutions of all S2 multispectral bands.
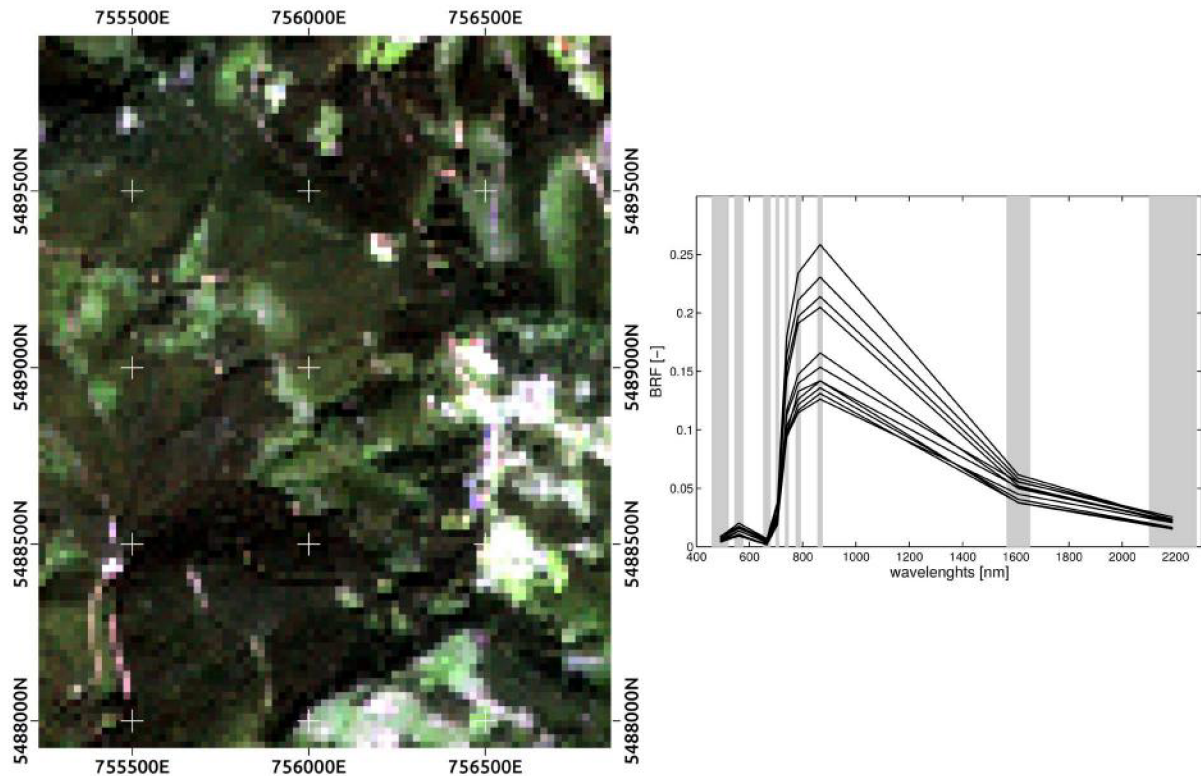
Figure 3.7: Atmospherically corrected subset of S2 multispectral image for the Bílý Kříž site in natural colors. The image spatial resolution is 20 m and was placed in UTM Zone 33N (WGS 84). The graph at the right hand side illustrates spectral reflectance (BRF) signatures of eleven randomly selected pixels.

3.3 Reconstruction of virtual Norway spruce 3D tree models

The first goal of this study was to create realistic digital 3D model of N. spruce tree. There are several approaches that can be applied to create a virtual 3D spruce model, i.e. using simple geometrical primitives or complex 3D shapes. For the radiative transfer modelling purpose of this study was necessary to construct as much precise geometrical model as feasible in order to obtain a benchmark spruce model. Since the input vegetation parameters were only for the Bílý Kříž research site (Section 3.2.2), the constructed 3D spruce models were tailored to this location and data from the Černá hora site were adapted for it.

One approach to create a 3D spruce model, where the tree growth is computer simulated (i.e. L-systems), is not precise enough, because many input parameters that are not explicitly measured are causing unacceptably high uncertainty in final outputs (Janoutová 2012). More precise approach is to use a LiDAR scanning data, which supply explicit information about position and density of wood and foliage elements, and combine it with a priori information about angular shoot distribution. Such approach produces 3D digital models of trees based on specifics of the exact location and, therefore more realistic and precise.

Creation of the 3D spruce spruce models was split into three steps.

1. An existing algorithm (Sloup 2013) for spatial reconstruction of trunk and branches from terrestrial LiDAR data was applied (Figure 3.8b, 3.8c).

2. We scaled and transformed the foliage point cloud and wooden skeleton of the spruce model to fit the desired dimensions. It was necessary because the LiDAR data were taken at the Černá hora site, where trees were older and higher, therefore the point clouds had to be scaled the forest dimensions at the Bílý Kříž site.

3. a new algorithm for the distribution of shoots into the tree crown was developed and applied (Figure 3.8e). This last step is crucial and the most innovative achievement of this thesis.

3.3.1 Reconstruction of wooden skeletons - trunks and main branches

In the first step, the algorithm designed by Sloup (2013) was applied to create a detailed wooden skeleton (trunks and main branches) from input terrestrial LiDAR data.

The fully automated algorithm for reconstruction of wooden skeleton is able to process wooden point cloud containing spatial gaps from omission of laser returns duet to various obstacles (other branches, trunks, and needles). The process goes in three steps:

1. component identification - spatially-related clusters of the points are identified

2. component analysis - branch structure is reconstructed in each identified component

3. component connecting - all the components are interconnected to form the final branch structure (Sloup et al. 2013, Figure 3.9)

The process of connecting the components together was designed to keep real architecture of branches and their connections to the trunk (Figure 3.8c).

(a)	(b)	(c)	(d)	(e)
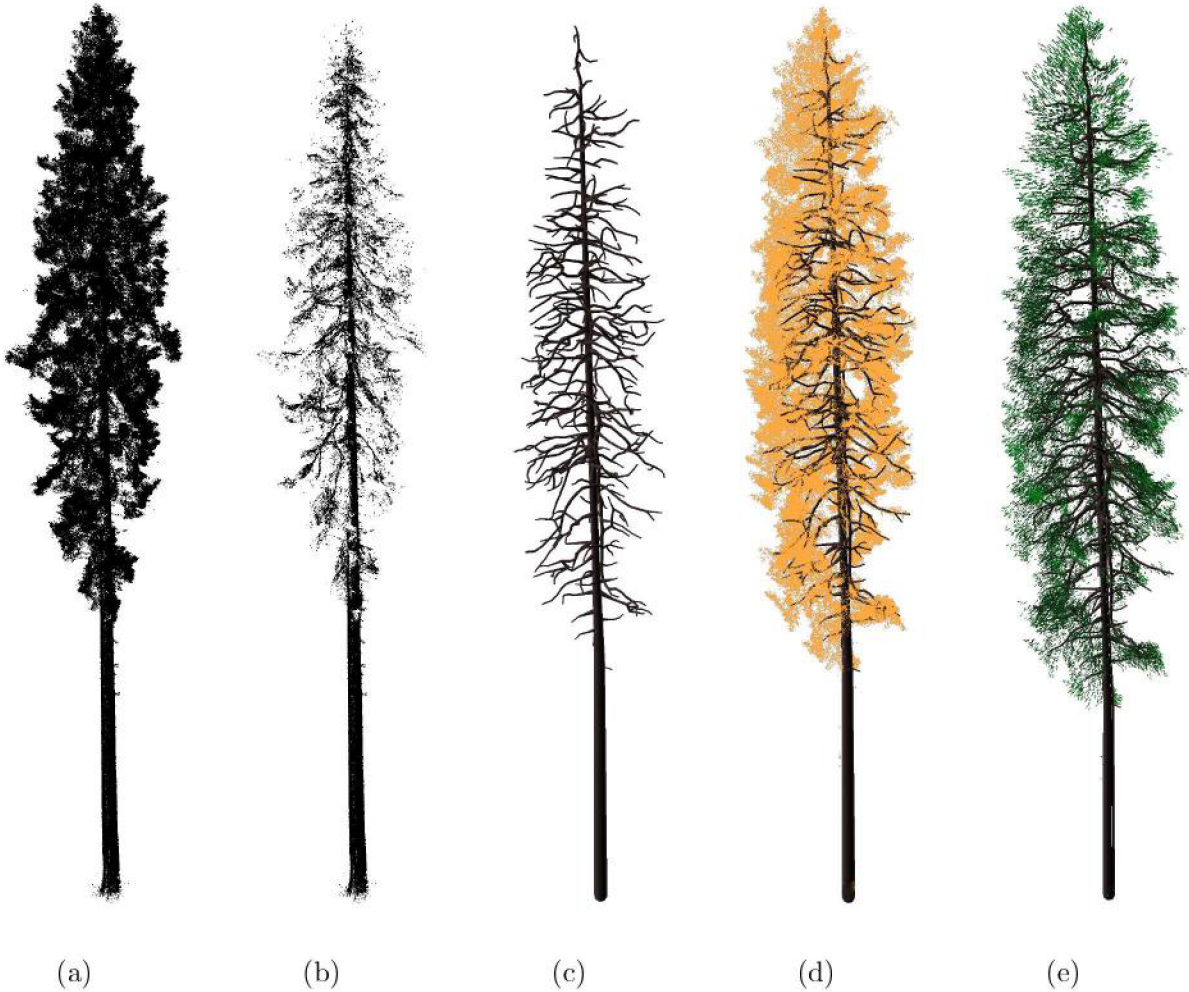
Figure 3.8: Creation of a virtual 3D spruce model from a terrestrial LiDAR point cloud. a) original terrestrial LiDAR scan of a spruce tree (Section 3.2.1), b) separated wooden point cloud (Section 3.2.1), c) reconstructed wooden skeleton (Section 3.3.1), d) reconstructed wooden skeleton with scaled foliage point cloud (Section 3.3.2), and e) the final 3D spruce model populated by shoots of two age categories: current year (light green) and older shoots (dark green) (Section 3.3.3).

3.3.2 Translation and scaling of the foliage point cloud

The second step was needed to translate spatially the foliage point cloud in such a way it matches the virtually reconstructed wooden skeleton and subsequently to scale them both to fit the desired dimensions at the Bílý Kříž site.

The output of the first step, i.e. The reconstructed 3D wooden skeleton, was created in local coordinate system with origin in the center of the trunk base. To ensure the same coordinates as for wooden skeleton, the foliage point cloud was spatially translated according its coordinates system. The transformation was executed in the following seven steps:

1. finding the point with the maximum z-coordinate of created reconstructed wooden skeleton,

$$M_{sk} = (x_{sk};\ y_{sk};\ z_{sk})$$

2. finding the point with the maximum z-coordinate of wooden point cloud,

48
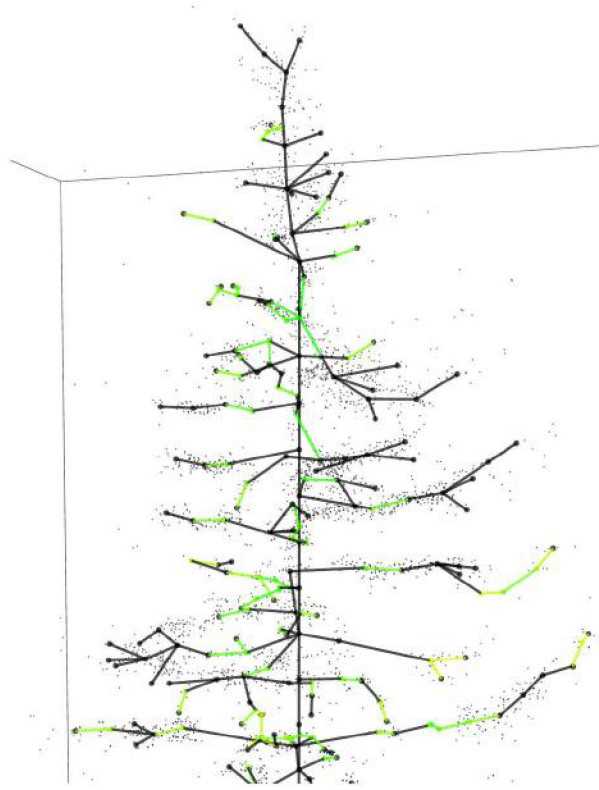
Figure 3.9: Part of the tree with interconnected (green lines) components (adapted from Sloup 2013).

$$M_{wc} = (x_{wc};\ y_{wc};\ z_{wc})$$

3. finding the point with the maximum z-coordinate of extracted foliage point cloud,

$$M_{fc} = (x_{fc};\ y_{fc};\ z_{fc})$$

4. calculating a height correction coefficient from the wooden and foliage point clouds (both clouds have the same coordinate system),

$$c_{cor} = z_{fc} - z_{wc}$$

5. calculating the vector $\mathbf{v}$ for translation

$$\mathbf{v} = (x_{sk} - x_{fc};\ y_{sk} - y_{fc};\ z_{sk} - z_{fc} + c_{cor})$$

6. formulating translation matrix

$$\begin{pmatrix} 1 & 0 & 0 & x_{wa} - x_{fc} \\ 0 & 1 & 0 & y_{wa} - y_{fc} \\ 0 & 0 & 1 & z_{wa} - z_{fc} + c_{cor} \\ 0 & 0 & 0 & 1 \end{pmatrix}$$

7. translating the entire foliage point cloud.

As already mentioned the terrestrial LiDAR scans were acquired at the Černá hora site, whereas estimation of forest quantitative parameters was performed for the Bílý Kříž site, where airborne, satellite, and field data were available all together (Sections 3.2.2 and 3.2.3). Since spruces at the Černá hora site were older and higher than trees at the Bílý Kříž site (Section 3.1) a scale transformation was needed to equalize foliage point clouds with size of reconstructed wooden skeletons in order to fit dimensions of trees at the Bílý Kříž site. The scaling factor f_s was calculated as quotient of required canopy height and z coordinate of wooden skeleton (z_{sk} - see step 1.). The transformation matrix can be expressed as:

$$\begin{pmatrix} f_s & 0 & 0 & 0 \\ 0 & f_s & 0 & 0 \\ 0 & 0 & f_s & 0 \\ 0 & 0 & 0 & 1 \end{pmatrix}$$

After transforming the foliage point cloud according to the wooden skeleton, the algorithm distributing shoots within a crown can be applied based on the transformed foliage point cloud.

3.3.3 Algorithm for shoot distribution within spruce crown

The last step in the process of the 3D spruce model creation was distribution of shoots within crown. Spatial distribution of needles has significant impact on the light scattering, especially in the near infrared (NIR) part of the electromagnetic spectra. Consequently, the distribution of shoots of different age categories is crucial part of the whole 3D spruce model reconstruction. Shoot distribution must reflect the actual foliage point cloud establishment (Section 3.2.1), existing leaf density and geometry expressed in the form of the LAI and leaf angle distribution (LAD). The algorithm for shoot distribution uses information about shoot positions from foliage point cloud (Section 3.2.1), about shoot density from the LAI (user defined variable), and about angular distribution from LAD obtained from Barták (1992, Figure 3.2, and Section 3.2.1).

The LAI is required to be retrievable as a free variable. It has to be parametrized independently. In other words, the model is constructed based on user predefined value of the LAI.

Shoots are defined as separate 3D objects (i.e. planes along the shoot axis, individual needles), however for the description of this algorithm it is not important to consider the exact shoot representation (Section 3.4.3).

The shoot distribution procedure had three main steps. In the first step we calculate the position of each shoot within a tree crown. In the second step we split shoot positions in two groups by their age: current-year shoots and older shoots. Finally, in the third step we place shoots to their defined spatio-geometric positions and angular orientations.

3.3.3.1 Calculation of shoot positions

As already indicated, the number of shoots depends on the user-defined LAI. The total number of shoots within a reconstructed crown is, therefore, computed from a given LAI value as follows:

$$n_{shoots} = \frac{2 \cdot LAI \cdot S_{proj}}{S_{shoot}}, \tag{3.1}$$

where n_{shoots} is number of all shoots in a whole crown, S_{shoot} is total area of the needles in one shoot (calculated by Blender, www.blender.org), and S_{proj} is the circular projection area of the crown represented by extracted and scaled foliage point cloud. The diameter of the circular projection area is calculated as:

$$d = min(max_x - min_x, max_y - min_y), \tag{3.2}$$

50

where d is a diameter of the circular tree projection, max_x and min_x is the maximum and minimum value of x coordinates of all points and max_y and min_y is the same variables for y coordinates.

The calculation of shoot positions runs in two steps. First, we separate the foliage point cloud into cubes with a given size (side around 0.18 m for trees of 15 m in height). The size of cubes directly influences the computational time because more points present in a single cube requires more time to calculate all shoot positions. Thus, the size of cubes is expected to be specified by the user according to available computational resources and density of processed foliage point cloud.

In the second step we calculate shoot positions within every cube. The positions are calculated by k-means function from the cluster analysis theory (see Section 2.1.5.6). Each cube contains set of points $\mathbf{x} = \{\mathbf{x_1}, \mathbf{x_2}, \ldots, \mathbf{x_n}\}$, where $n \in \mathbb{N}$ is a number of the points in the currently processed cube. Each point is defined by its position $\mathbf{x_i} = (x, y, z)$. The k-mean clustering makes a partition in the set of points into the $k < n$ subsets $\mathbf{S} = \{S_1, S_2, \ldots, S_k\}$. The k is then calculated from the given number of shoots (Equation 3.1):

$$k = \frac{n}{\frac{n_{points}}{n_{shoots}}}, \tag{3.3}$$

where n_{points} is number of total points in the whole foliage point cloud. The k-mean function provide also coordinates of the clusters centroid, which represents the position, where a shoot is placed. The algorithm iterates through all cubes with at least one point defines position of each shoot.

3.3.3.2 Separation of shoots in two age categories

Next task is to extract shoot positions of two needle age groups: current-year and older needles (Figure 3.8e). For this we divide the processed tree into the cubes with a different size. It would be possible to use the original cubes, established during the calculation of the shoot positions, but since the new cubes do not need to be so small, their larger size helps us to save computer memory and computational time. Nevertheless, creation of both cube meshes requires per tree optimization, because each tree varies in size and structure and also it has LiDAR scans of different quality in sense of point density, number and size of gaps etc.. Therefore, size of cubes for the shoot location calculation is generally smaller (in our case 0.18 m), whereas cubes for the shoot separation into the age categories are larger (in this study 0.3 m for 15 m high trees).

Before we start separating the needle shoots into two age categories, we need to find a tree envelope, i.e. cubes at the tree crown's periphery, where the current shoots occur prevailingly at the crown periphery. The process of finding the crown envelope consists of four steps (illustrated in Figure 3.10):

1. choosing a cube v_c, the algorithm iterates through every cube contained at least one shoot position,

2. finding set of neighbors $N_{26}(v_c)$ of cube v_c (see Definition 2.1.7),

3. creation of the tree envelope - checking if at least one cube of the $N_{26}(v_c)$ does not contain a shoot positions, if yes add the v_c to set of edge cubes and continue with the next cube, otherwise directly continue with the next cube,

4. filling the envelope of a given crown - reduce convexity of the envelope (for more details see explanation below),

1. choosing a cube

iterate through every cube contained at least one shoot position

2. finding all neighbors

3. checking for empty cubes

if $\sum$ > 0 → set of envelop cubes

if $\sum$ $= 0$ → set of inside cubes

4. filling the envelope of a given crown - reduce convexivity of the envelope
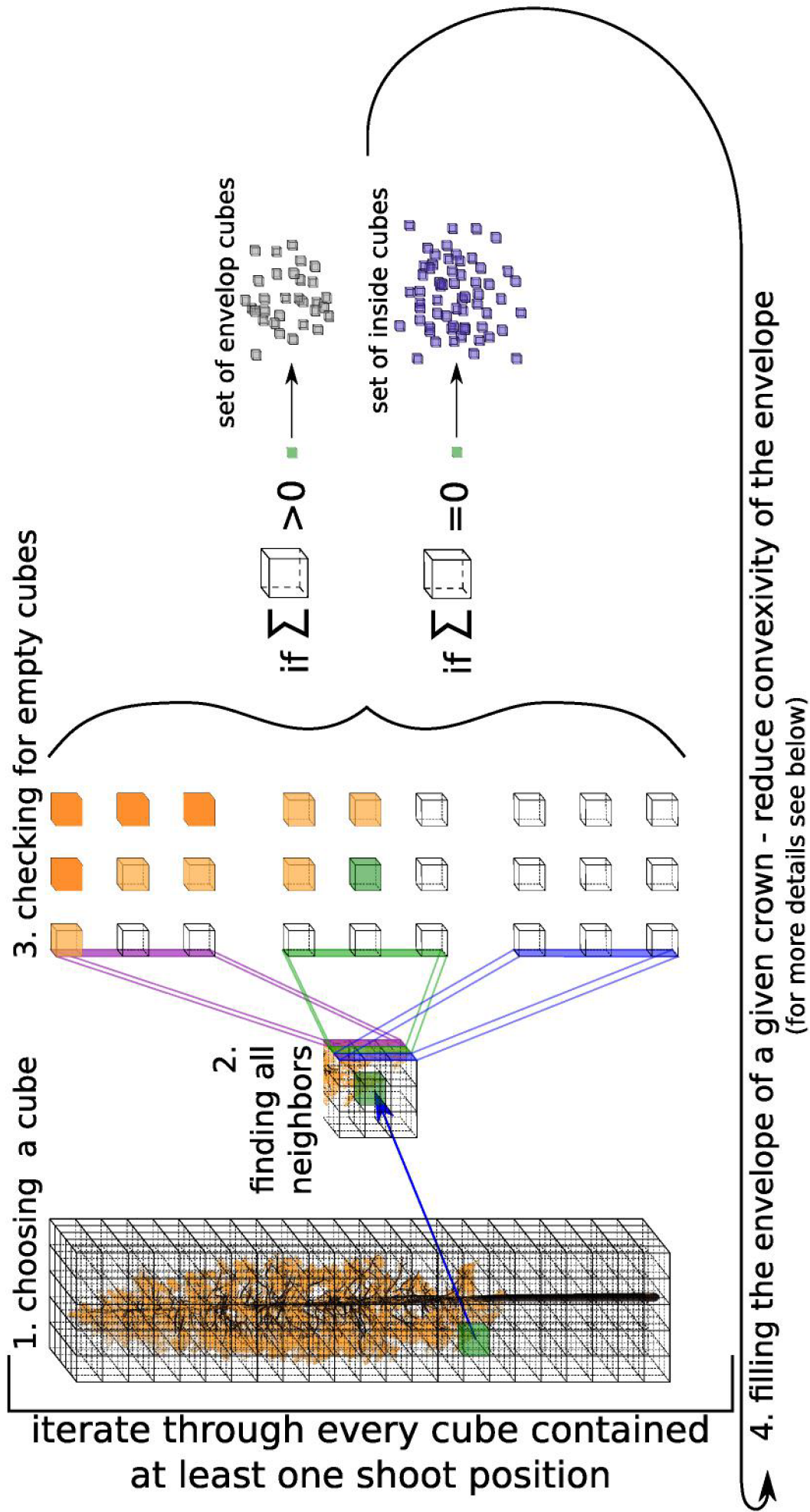(for more details see below)

Figure 3.10: The process of finding crown envelope. The corresponding steps are described above 1. – 4.

52

The crown envelope convexity reduction prevents the new shoots are being placed inside the crown as they are naturally growing at the periphery. This may happen when the air gap size is larger than cube size. The following steps were implemented to reduce the inappropriate crown envelope convexity (illustrated in Figure 3.11):

4.1. finding cubes from the crown envelope in a current horizontal layer - $\mathbf{V_c}$,

4.2. separating $\mathbf{V_c}$ into lines by x coordinate,

4.3. finding cubes with minimum and maximum y coordinate value - v_{min}, v_{max},

4.4. finding gaps between v_{min} and v_{max},

4.5. if there are any gaps, fill them with new cubes,

4.6. creating a new set $\mathbf{V_{cf}}$ and adding new cubes together with cubes from $\mathbf{V_c}$,

4.7. repeating steps 4.2. – 4.5. for the y-axis,

4.8. adding new cubes into $\mathbf{V_{cf}}$,

4.9. separating $\mathbf{V_{cf}}$ in lines by x coordinate,

4.10. finding cubes with the minimum and the maximum y coordinate value - v_{min}, v_{max},

4.11. adding cubes v_{min} and v_{max} into $\mathbf{V_{c\,new}}$,

4.12. repeating steps 4.9. – 4.11. for the y-axis,

4.13. setting of cubes $\mathbf{V_{c\,new}}$ as the new set of envelope cubes for the current horizontal layer.

The algorithm processes tree crown, as being divided in several horizontal layers (l_n). The height of each layer is based on empirical observations that one whorl takes about 0.8 m of crown height. The percentage of the current-year needle category in each layer was assigned according to measurements published by Barták (1992) (see Table 3.6). The following steps were carried out (illustrated in Figure 3.12):

1. finding corresponding percentage of current-year shoots in a horizontal layer l_n,

2. finding envelope cubes of the tree crown in l_n,

3. finding shoot positions inside the envelope cubes,

4. calculating number of found shoot positions,

5. adding found shoot positions into the set of current-year shoot positions,

6. subtracting the found shoot positions from the remaining shoot positions,

7. verifying the percentage of shoot positions in the set of current-year shoot positions; testing if the percentage is higher or lower than the corresponding percentage in l_n,

8. deciding to continue or stop the algorithm; if there are not enough current shoot positions, algorithm continues to the next step 9. otherwise it continues to the next layer and repeats steps 1. – 7.,

9. extending amount of cubes in the envelope of tree crown toward the tree trunk in l_n done for x, y axis separately (see Figure 3.13),

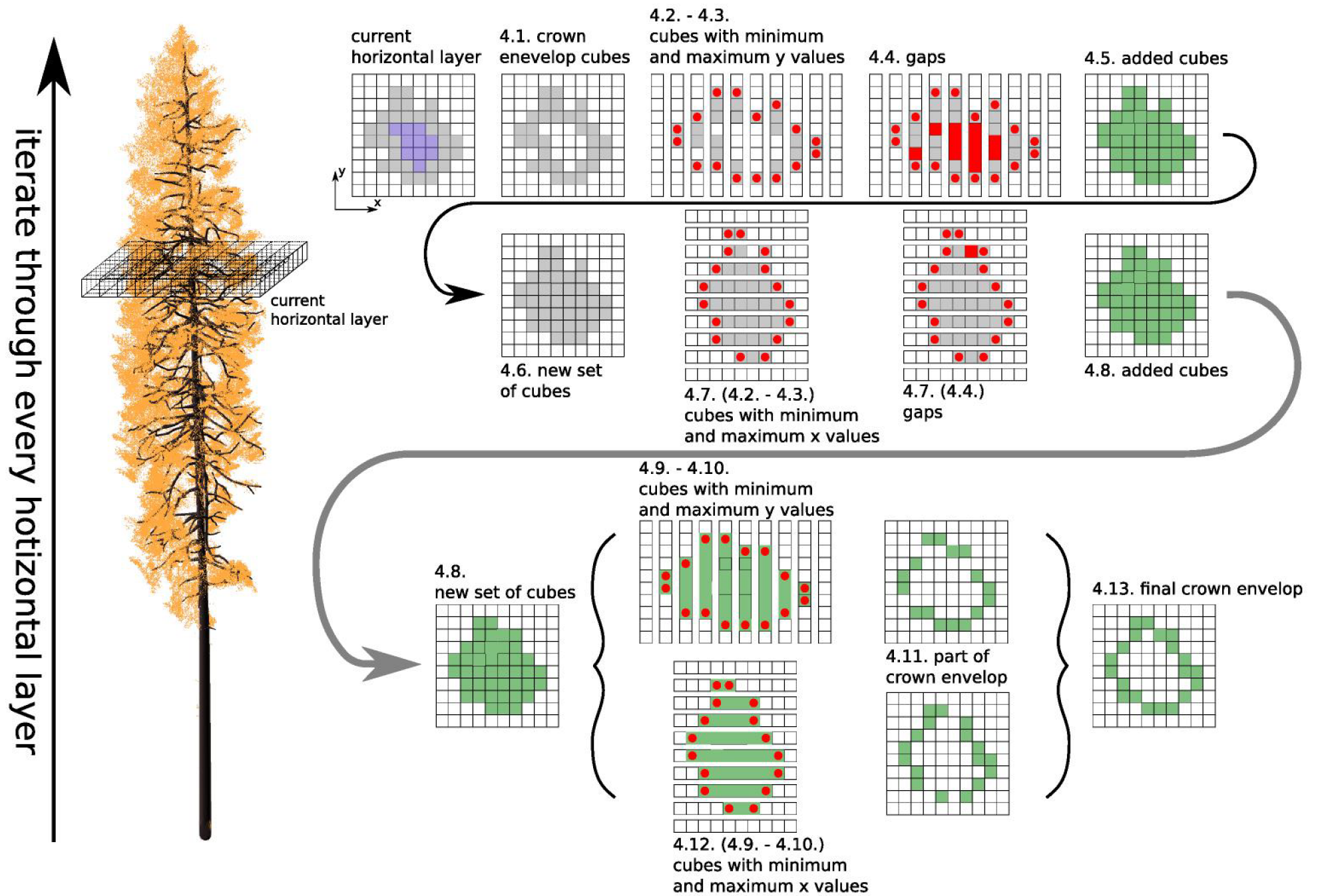10. returning to the step 3. until the end.

Figure 3.11: The process of crown envelop convexity reduction. This process describes in a detail the step 4. that forms the process of finding crown envelop. The corresponding steps are described above 4.1. – 4.13.

1. finding corresponding percentage of current-year shoots in a current horizontal layer

order of the whorl	1	2	3	4	5	6	7	8	9	10
percent	0.66	0.68	0.48	0.31	0.26	0.24	0.18	0.10	0.07	0.05

2. finding envelope cubes

3. finding shoot positions inside the envelope cubes

found shoot positions

current horizontal layer

5. adding found shoot positions into the set of current-year shoot positions

6. substracting found shoot positions from the remaining shoot positions

4. calculating number of found shoot positions

found shoot positions → set of current-year shoot positions

found shoot positions — set of remaining shoot positions

continuing to next horizontal layer

7. - 8. verifiing the percentage of found current-yer shoot positions

9. extending amount of cubes in the envelope and continue to step 3.

if $\dfrac{\sum \blacksquare}{\sum} \geq 0.26$
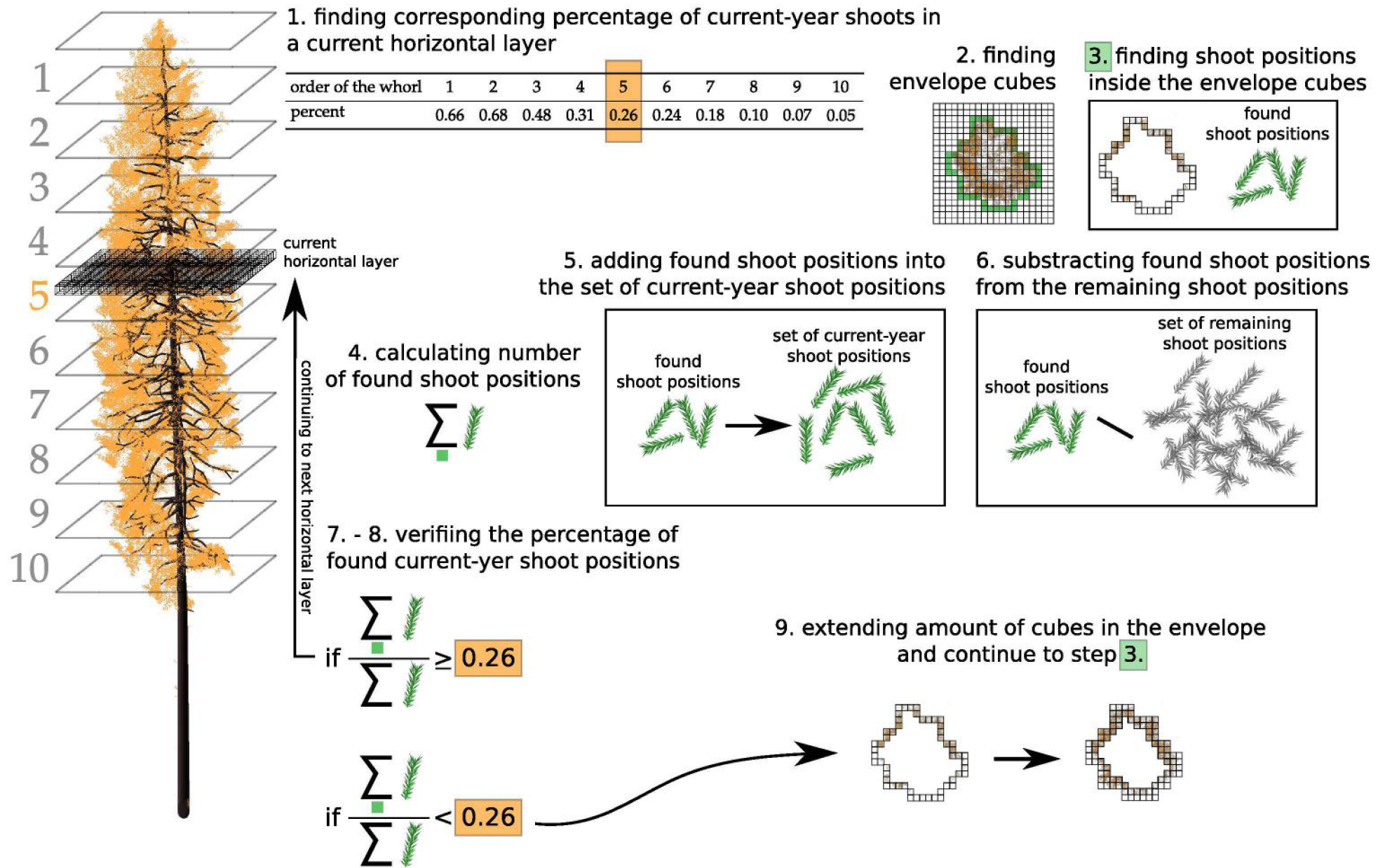
if $\dfrac{\sum \blacksquare}{\sum} < 0.26$

Figure 3.12: The process of separating finding crown envelope. The process iterates through every cube one by one, where are some points from foliage point cloud.

order of the whorl	1	2	3	4	5	6	7	8	9	10
percent	1	0.82	0.61	0.49	0.35	0.29	0.23	0.14	0.07	0.05

Table 3.6: The percentage of current-year shoots in branch whorls according to Barták (1992, 1993). The top whorl has number one and numbering is increasing towards the ground. The current-year shoots are prevailingly located on the periphery of a tree crown.
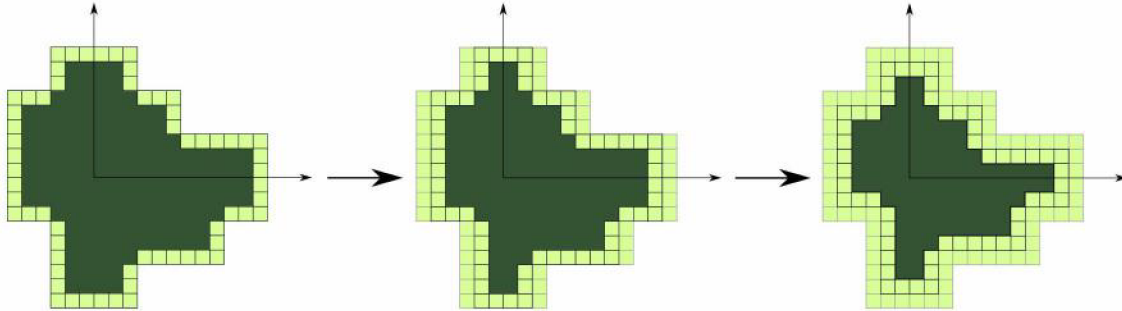

Figure 3.13: Extension of a crown edge towards the tree trunk. The extension is conducted in two consecutive steps namely in x and y direction. Light green represents cubes contained in tree crown envelop and the dark green represents inside of crown.

3.3.3.3 Shoots transformation to their position

Once the position of all shoots are determined, shoots are distributed within a tree crown. The shoots have to be first rotated and then translated depending on their position in tree crown. Transformation matrix for these two-step operation is calculated for each shoot separately. For the transformation composition it was more efficient to apply first the rotation and then the translation.

The position in which the shoot was supposed to be translated is noted as $L = (l_x, l_y, l_z)$. A shoot was first rotated around the y and z axis (Equation 2.18 and 2.19). The elevation angle β, listed in Table 3.7, are dependent on height (l_z). The calculation of the azimuth angle γ is based on l_x and l_y. It is randomize by an angle ψ gaining values within the range $\langle -\frac{\pi}{4}, \frac{\pi}{4} \rangle$ (Equation 3.4).

$$\gamma = \begin{cases} arctan(\frac{l_y}{l_z}) + \psi & \text{if } l_x > 0 \\ arctan(\frac{l_y}{l_z}) + \pi + \psi & \text{if } l_x < 0 \end{cases} \tag{3.4}$$

	age	1	2	3	4	5	6	7	8
β	angle [°]	35	35	5	-15	-35	-45	-25	-35
$d\beta$	deviation [°]	-5 − 12	5 − 12	-5 − 15	-5 − 30	-10 − 40	-5 − 40	-15 − 20	-15 − 15
h	height [m]	0 − 1	1 − 2	2 − 3	3 − 4	4 − 5	5 − 6	6 − 7	> 7

Table 3.7: Summary of shoot elevation angles (β), their deviations $d\beta$ and height (h) in which the shoots of eight age classes occur. The height is expressed as the distance from the tree top ($h_t - l_z$), where h_t is z coordinate of the tree top and l_z is z coordinate of a shoot position.

the vector for shoot translation was calculated as $\mathbf{v} = (L - \mathbf{0})$, where $\mathbf{0}$ is the origin of the co-ordinate system. The transformation matrix was computed as:

$$
\begin{pmatrix} 1 & 0 & 0 & v_x \\ 0 & 1 & 0 & v_y \\ 0 & 0 & 1 & v_z \\ 0 & 0 & 0 & 1 \end{pmatrix} \left(\begin{pmatrix} cos\gamma & -sin\gamma & 0 & 0 \\ sin\gamma & cos\gamma & 0 & 0 \\ 0 & 0 & 1 & 0 \\ 0 & 0 & 0 & 1 \end{pmatrix} \begin{pmatrix} cos\beta & 0 & -sin\beta & 0 \\ 0 & 1 & 0 & 0 \\ sin\beta & 0 & cos\beta & 0 \\ 0 & 0 & 0 & 1 \end{pmatrix} \right) =
$$

$$
= \begin{pmatrix} 1 & 0 & 0 & v_x \\ 0 & 1 & 0 & v_y \\ 0 & 0 & 1 & v_z \\ 0 & 0 & 0 & 1 \end{pmatrix} \begin{pmatrix} cos\gamma\,cos\beta & -sin\gamma & -cos\gamma\,sin\beta & 0 \\ sin\gamma\,cos\beta & cos\gamma & -sin\gamma\,sin\beta & 0 \\ sin\beta & 0 & cos\beta & 0 \\ 0 & 0 & 0 & 1 \end{pmatrix} = \qquad (3.5)
$$

$$
= \begin{pmatrix} cos\gamma\,cos\beta & -sin\gamma & -cos\gamma\,sin\beta & v_x \\ sin\gamma\,cos\beta & cos\gamma & -sin\gamma\,sin\beta & v_y \\ sin\beta & 0 & cos\beta & v_z \\ 0 & 0 & 0 & 1 \end{pmatrix}
$$

Equation 3.5 represents the general matrix for shoot models transformation, which was applied to distribute shoots of the two age categories within the reconstructed 3D model of a Norway spruce tree.

3.3.4 Main outcome

New 3D model of a Norway spruce tree reconstructed from terrestrial LiDAR scans is the main outcome of this part. The 3D model is composed out of two sets of objects created separately: wooden skeleton and foliage - needle shoots. The wooden skeleton was reconstructed using LiDAR returns from main wooden tree parts (trunk and branches) with the algorithm designed by Sloup (2013). The foliage reconstruction was done with a new algorithm designed in this study. The main task of this algorithm is biologically correct distribution of shoots within a tree crown, which represents the most innovative outcome.

The reconstructed 3D spruce model of a single tree contains significantly large number of facets, about 22 Millions. For better imagination, the same number of geometrical facets was needed to create a large scale 3D representation of Toulouse city center in France. In order to achieve a feasible computational time, it was necessary to optimize the model before its operational use for simulating canopy forest scenes in the DART model. The optimization procedure is described in the following Sections 3.4.3, 3.4.4, and 3.4.5.

3.4 Radiative transfer modelling and optimization

One of the main goals of this thesis was to optimize 3D spruce model that it is applicable for radiative transfer (RT) simulations. Radiative transfer of forest scenes composed from the 3D spruce models with needle shoots (Figure 3.19a) contain large number of facets, therefore RT computation is extremely demanding. For the operational use, it is necessary to optimize the scene parametrization.

This section is separated into five parts. The first part describes all possibilities how to parametrize trees in the DART model (Section 3.4.1). In the second part the spruce model with pre-prepared geometric crown shapes (base model) is introduced (Section 3.4.2), which was used before the 3D spruce models were created in this study. The last three parts describe the optimization that was studied at three structural levels:

shoot level: Four shoot models were evaluated (Section 3.4.3),

tree level: Four shoot models were evaluated in whole tree and compared to airborne data (Section 3.4.4),

canopy level: Four shoot models were evaluated in whole forest scene and compared to airborne data. The 3D spruce models were transformed to turbid cells (Section 3.4.5).

3.4.1 DART scenes

In the DART model it is possible to parametrize trees in several ways (Figure 3.14). The first way uses the pre-prepared geometric crown shapes (base model) (Figure 3.14 on the right). Turbid cells contain infinite number of infinite small facets, which are distributed in the cell based on LAD, LAI and other DART parameters specifying gaps distribution in the tree crown vertically and horizontally. The tree crown can be separated into horizontal levels and for each level it is possible to set up different properties of turbid cells, gaps distribution and relative trunk width. It is also possible to define the branches as simple 3D objects. The base tree models are used mainly because they reduce computation requirement. However, for coniferous trees this parametrization may leads to large discrepancies in forest reflectance (BRF) simulations. The difference between DART simulated and remote sensing (RS) reflectance (BRF) is illustrated in Figure 3.15. From the comparison it can be seen that more significant differences are found for the coniferous spruce stand than for broadleaf beech stand. The possible explanation is that the base tree model is not able to describe fine scale scattering properties of conifer trees.

The second way how to parametrize trees in the DART model is to import a 3D tree model (Figure 3.14 on the left). This approach allows to import object groups and set up different properties to each group, e.g. set up different optical properties for different age category of shoots.

The 3D tree model can be treated in two different ways. First radiative transfer is calculated directly on the 3D model. This approach is very precise, but extremely computationally demanding. Simulating a scene with several mature trees is almost impossible.

The second way how to treat the 3D tree model is to transform the foliage part to turbid cells. This approach preserves the structure of the tree and the distribution of the foliage within the tree crown. The possibility to set up different optical properties for different object groups is also preserved. Although RT computation is slightly more demanding than for the base model with predefined crown shapes, it produces more accurate simulations of canopy reflectance (BRF).
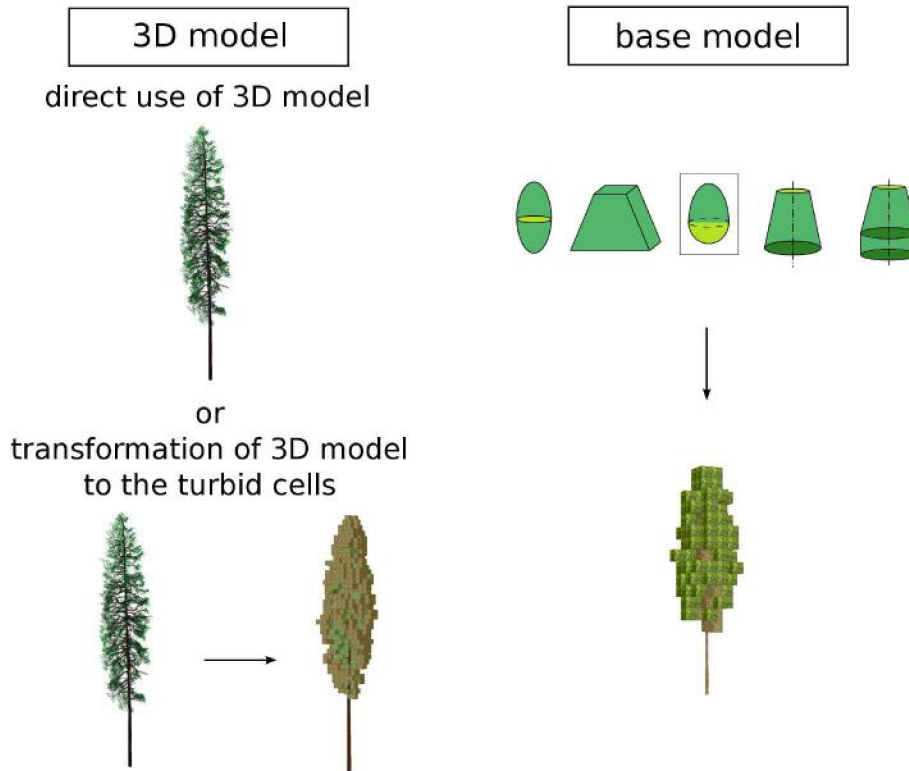
Figure 3.14: There are three ways how to parametrize trees in DART: using 3D tree model directly, letting 3D tree model to be transformed to turbid cells, and using trees with pre-prepared geometric crown shapes (base model).

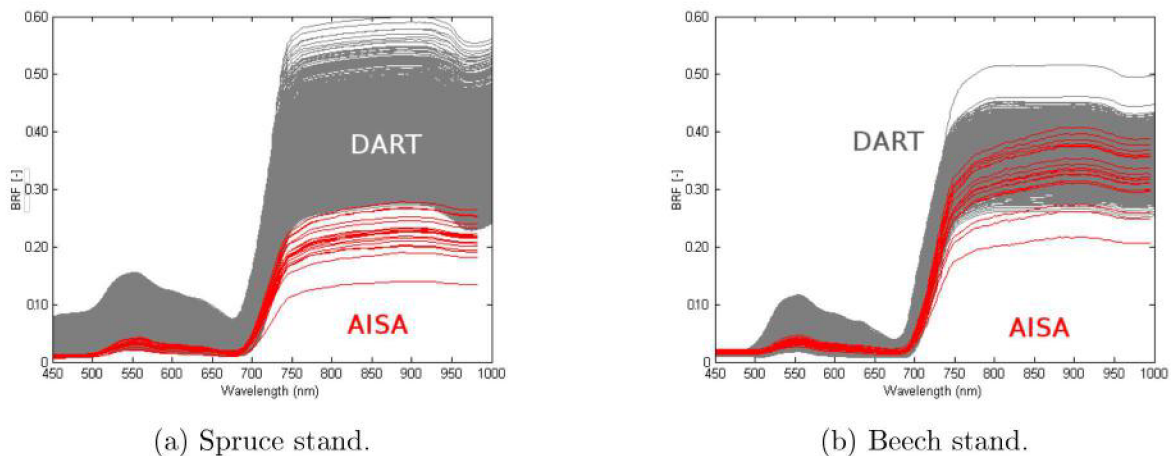(a) Spruce stand.

(b) Beech stand.

Figure 3.15: A comparison of spectral reflectance (BRF) between results simulated by with base spruce model (grey) and airborne data (aggregated into 20 m pixel size) acquired by the AISA Eagle imaging system (red).

3.4.2 Base spruce model

First the base spruce model is introduced. This type of spruce forest parametrization was used in earlier studies of Malenovský et al. (2008, 2013), where retrievals were applied on sunlit canopy pixels only, however this parameterization might not be always suitable as demonstrated in Figure 3.15a. This parametrization was used at the tree (Section 3.4.4) and the canopy (Section 3.4.5) levels to assess the improvement of the new 3D spruce model.

The base spruce model parametrization was build from field measurements acquired at the Bílý Kříž site in 2006. Parametrization of tree crown shape were done by following parameters:

- tree height

- crown height

- trunk height below crown

- crown projection, and

- intermediate height, where is the crown widest from side view.

Illustration of these parameters are in Figure 3.16 and used values are in Table 3.8. Distribution of foliage and gaps were measured in horizontal layers (Figure 3.17) and applied in the DART model (Figure 3.18 and Table 3.9).

Figure 3.16: Illustration of base spruce model parametrization. Adapted from DART manual (CESBIO 2016).
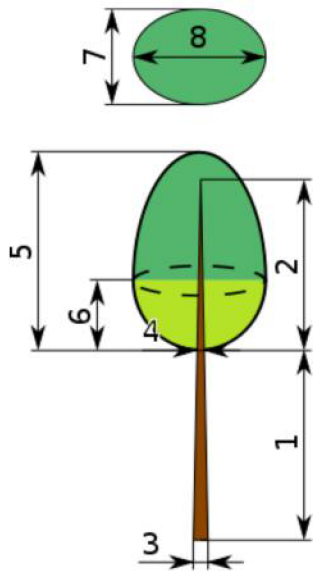
dim.	parameter	mean	SD
1	trunk height below crown [m]	2.91	0.68
2	trunk height within crown [m]	6.4	0
3	trunk diameter below crown [m]	0.11	0.025
4	trunk diameter within crown [m]	0.05	0
	crown type	composed ellipsoid	
5	crown height [m]	7.87	2.5
6	intermediate height [m]	2.62	0.8
7	first axis	2.38	0.4
8	second axis	2.38	0.4
	number of crown levels	3	

Table 3.8: Settings for parametrization of base spruce model. The dimensions are illustrated in Figure 3.16.
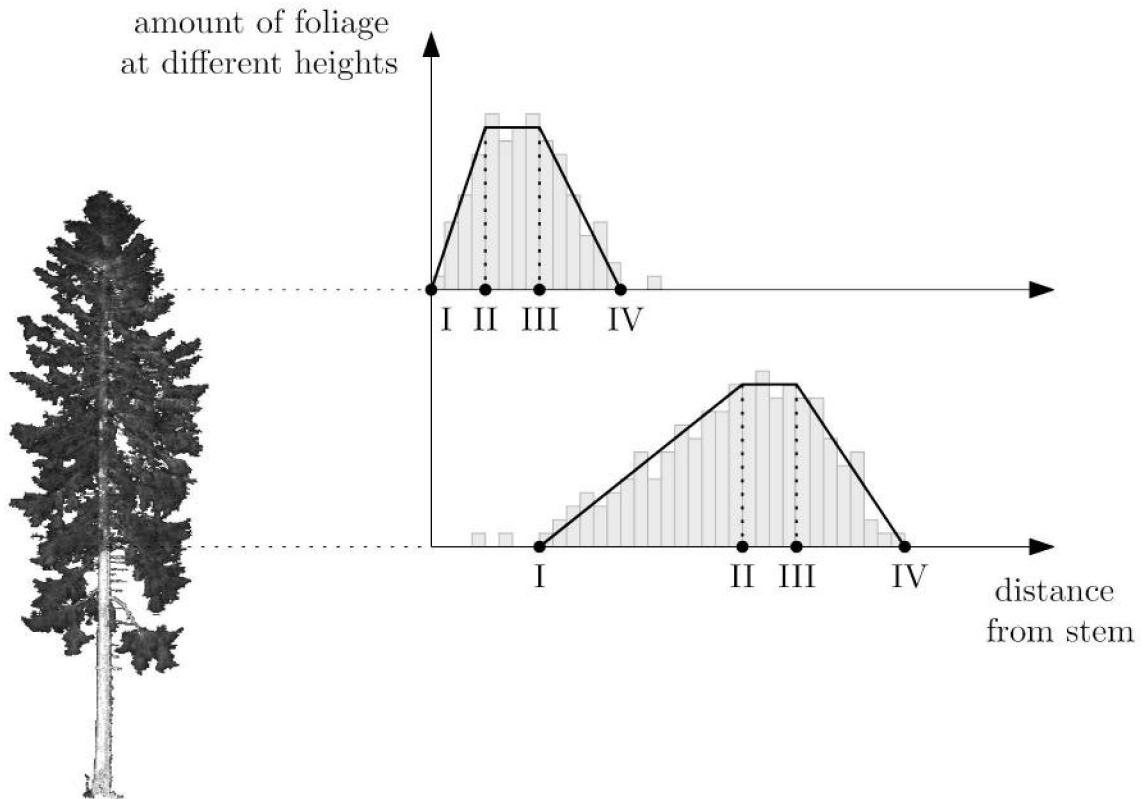
Figure 3.17: Distribution of the foliage density in tree horizontal layers, where I is the beginning of growth of living foliage, II is the beginning of full growth, III is the end of full growth, IV is the end of growth.
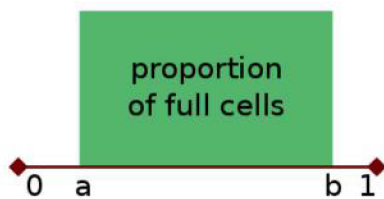

Figure 3.18: Illustration of gaps distribution. The zero value corresponds to trunk and one value corresponds to edge of tree crown. Adapted from DART manual (CESBIO 2016).

parameter	crown levels		
	exposed	transition	shaded
rel. trunk height	0.18	0.36	0.46
rel. trunk diameter [-]	0	0.375	0.75
gaps distribution			
rel. horizontal distr. a	0	0.3	0.75
rel. horizontal distr. b	1	1	1
proportion of full cells [-]	0.85	0.5	0.3

Table 3.9: DART parametrization of crown levels with gaps distribution. Trunk height and diameter in crown level are relative to parameters for whole trunk (Table 3.8 and Figure 3.16). Horizontal distribution of leaves/gaps is relative to perpendicular distance from trunk to periphery of tree crown. Parameters a and b are illustrated in Figure 3.18.

Since the spruce trees preserve shoots with different age classes, there are differences in optical properties of shoots of different age. The optical properties in case of base spruce models were generated using the recalibrated PROSPECT 3 (PROSPECT 3S) leaf radiative transfer model (Malenovský et al. 2006). The optical properties were simulated by three standalone PROSPECT models adjusted for spruce needles of current season, one- and two-years old needles. PROSPECT generated optical properties were then combined per vertical crown level

according to incident solar radiation reaching crown (i.e., sun exposed, transitional, and shaded levels see Figure 1.2) as weighted mean with weights corresponding to the needle-generation abundance measured at the site within the destructive experiment of several sample trees extracted and taken apart during the growing seasons prior 2000 (Pokorný & Marek 2000). The actual weights applied for each crown level are provided in Table 3.10.

crown level	current needles	1 - year old needle	2 - year old needle
exposed	0.41	0.42	0.17
transition	0.15	0.18	0.67
shaded	0.02	0.31	0.67

Table 3.10: The weights applied to combine optical properties of three spruce needle generations within three horizontal crown levels of spruce trees (sum of the weights per functional crown level must be equal to 1) (adopted from Homolová et al. 2015a).

Disadvantage of using base spruce models is that the complex structure of spruce trees is not well captured using the parameters above. Especially, LAD and the gaps distribution are more complicated and their influence to light scattering is important, therefore the 3D spruce model is considered to be more appropriate solution.

3.4.3 Optimization at shoot level

Objectives of this part were:

- to find the optimal DART parametrization of the reference 3D needle shoot model (Figure 3.19a) and to find the best 3D simplified shoot model (Figure 3.19b)

- to compare these two shoot models with optimal distribution of sun zenith and azimuth angles.

For this tasks the data from Centre d'Etudes Spatiales de la BIOsphère (CESBIO) and RAdiation transfer Model Intercomparison (RAMI) IV exercises were used. The needle shoot model (needle, Figure 3.19a) and its first simplification (simple 1, Figure 3.19b) was created by Nicolas Lauret from CESBIO for RAMI IV exercises (Widlowski et al. 2015) and the other two simplifications were designed in this thesis.

In the DART model it is possible to transform 3D objects to turbid cells, nevertheless the number of facets in a single 3D spruce model with needle shoot model is still too high for simulating the whole look-up-tables (LUT) in reasonable time. Therefore it was needed to use simplification of the needle shoot model. The first simplification significantly decrease the number of facets (Table 3.11). The needle shoot model (Figure 3.19a) was taken as reference in this optimization level.

In the optimization of shoot level the ground reflectance (BRF) have a big influence on reflectance (BRF) of whole scene. Therefore two different ground reflectance values 1 and 0 were chosen.

In case of the first simplified model (Figure 3.19b) a problem with nadir view (zenith viewing angle is equal to 0) appeared, because the planes do not have any width. Therefore, the two new shoot models are created (Figure 3.19c and 3.19d). Both shoot models are based on the first simplified model (Figure 3.19b). The second simplified shoot model has small planes added perpendicularly to the top and bottom of the original ones. The shorter side d of the added

a) needle   b) simple 1   c) simple 2   d) simple 3
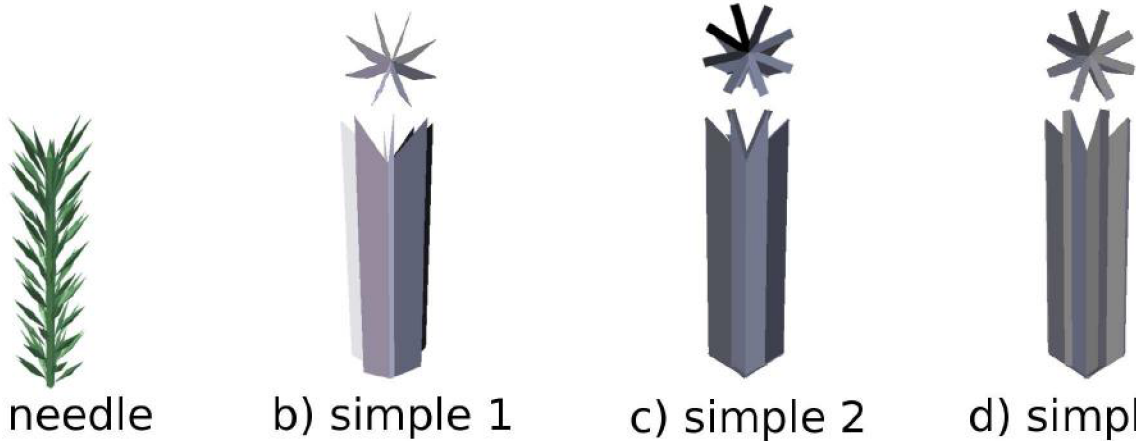
optimization setup

2 ground reflectances (0, 1), 3 viewing angles, 5 cell sizes

Figure 3.19: Model of a spruce needle shoot (needle) a) and its simplifications b)-d). The first simplified model (simple 1) b) is created by adding planes along the shoot axis and the area of the needles are the same as the planes. The second simplified model (simple 2) c) is created by adding small perpendicular plane on top and bottom of each plane from the first simplified model b). The third simplified model (simple 3) d) is created by adding a width dimension to the planes from the first simplified model. The width corresponds to the size of the small perpendicular planes from the second simplified model c). The optimization setup is shown at the bottom of the figure.

shoot model	shoot ID	number of facets
needle shoot model	needle	824
first simplification	simple 1	16
second simplification	simple 2	48
third simplification	simple 3	80

Table 3.11: Number of facets of the shoot model and its simplifications.

plane is $\frac{1}{10}$ from its larger side (Figure 3.20 on the left and Figure 3.19c). In the third simplified shoot model the width (the same as a shorter side from simple 2 shoot model) to the original planes was added (Figure 3.20 on the right and Figure 3.19d).
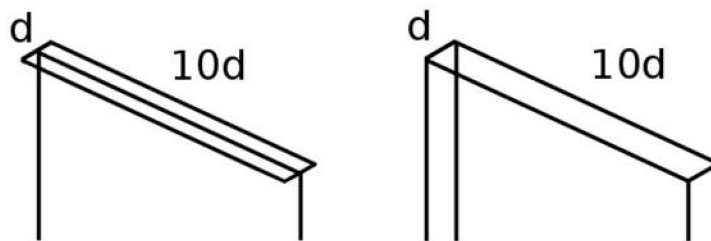

Figure 3.20: Illustration of how the second and the third simplifications of shoot model were created. On the left it is illustrated small added plane to the original plane. On the right it is illustrated the added width dimension (d) of the original plane.

Here the cell size was optimized and the best simplified shoot model was found. The cell size optimization was limited by actual computational resources, therefore, the sequences with combination of different cell size (0.2, 0.5, 0.8, 1, and 2 mm), and two different ground reflectance (0 and 1) were executed.

Since nadir viewing angle is the one where the difference between needle shoot model and its simplifications were the largest significant, the other two viewing angles were added into the optimization (Table 3.12). the optimization was run for three spectral bands from different regions (Table 3.12 and Figure 3.21), because it was very computationally demanding to simulate the whole spectra.

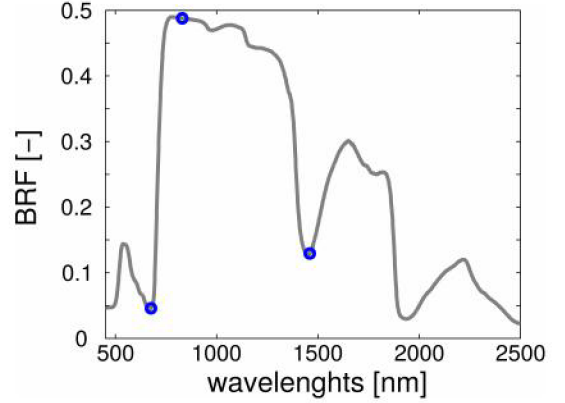| viewing angles		
	zenith angle [°]	azimuth angle [°]
nadir	0	0
offnadir 1	22	30
offnadir 2	80	354

Table 3.12: Viewing angles and bands used for optimization of cell size for needle shoot and for comparison of shoot models.

Figure 3.21: Bands selected for cell size optimization of shoots: 675, 830, and 1460 nm.

The cell size optimization showed that for smaller cell sizes the reflectance (BRF) is higher (Figure 3.22). The trend is the same for almost all settings of parameters and shoot models.

The comparison of shoot simplifications shows that the best performing simplified model is the second one (Figure 3.19c). This is not that obvious from the graphs (Figure 3.23), but we can see it when a mean value of each simplification and each setting of parameters was calculated (Table 3.13).

model	ground refl. = 0	ground refl. = 1
simple 1	0.53	0.37
simple 2	0.35	0.34
simple 3	0.47	0.42

Table 3.13: The mean of relative difference between the reference (Figure 3.19a) and each shoot simplification (Figure 3.19b − 3.19d) for two different ground reflectance (BRF). The green values are the smallest for both ground reflectance.
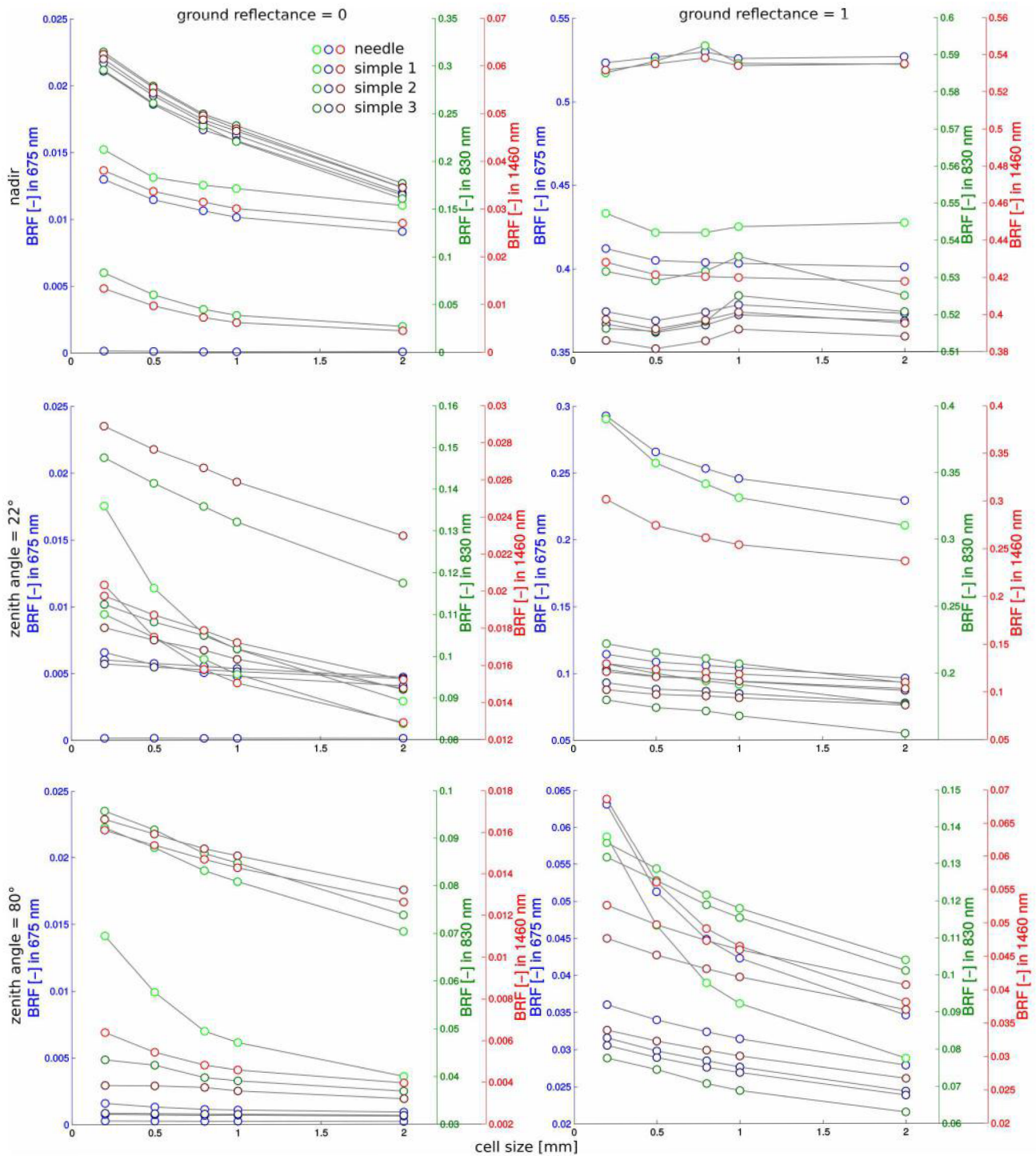
Figure 3.22: Results from cell size optimization for four shoot models, two ground reflectance, three angles, and three wavelengths (blue 675 nm, green 830 nm, and red 1460 nm). These graphs illustrate that reflectance (BRF) decreases with bigger cell size.

The further assessment was done for the reference needle shoot model (Figure 3.19a) and the best performing simplification only (Figure 3.19c). We analyzed detailed dependencies on solar viewing geometry and wavelengths. The results are shown in Figure 3.24 for:

- full illumination hemisphere: zenith angle with step 10° and azimuth angle with step 36°;
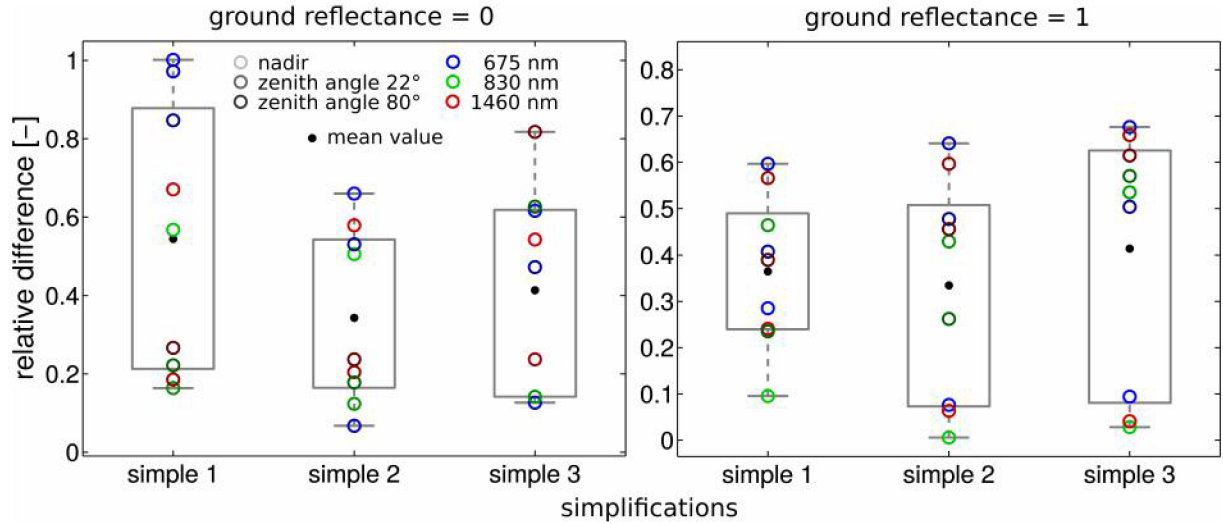
- two bands: 675 and 830 nm;

Figure 3.23: Relative difference between needle shoot and its simplifications. The difference is calculated as absolute value. There are combinations of two ground reflectance (BRF), three bands and three viewing angles. The bands are differentiated by colors: blue - 675 nm, green - 830 nm, and red - 1460 nm. The viewing angles are differentiated by shades: light - nadir, middle - zenith angle 22° and azimuth angle 30°, and dark - zenith angle 80° and azimuth angle 354°. The black dot is mean value of all the cases for one simplification.

- three viewing angles: nadir, zenith angle 22° and azimuth 30°, and zenith angle 80° and azimuth 354°;

- reflectance (BRF) of whole scene.

The optimization at the shoot level revealed that the shape of a shoot is very important for RT simulation. The difference in reflectance (BRF) between reference and simplified shoot models increases with increasing solar zenith angle. The results indicate that the magnitude of reflectance differences for two investigated wavelengths is smaller for less oblique viewing angles. This sensitivity study helped to understand the angular behavior of shoot scattering properties. Nevertheless the differences between reference and simplified shoot model strongly depends on viewing geometry.

The next step was a testing the applicability of the shoot simplifications at the tree level because reflectance differences are expected to be lower and more homogeneous than those at the shoot level.

Possible improvement of this part is to use a more precise reference shoot model. We already acquired detailed 3D scans of spruce needle shoots ATOS Core 3D scanner (http://www.gom.com-/metrology-systems/atos/atos-core.html) in collaboration with colleagues from Palacký University Olomouc. The scanned shoots have very high number of facets and the 3D scans have to be further processed before using it in the DART model. This was not feasible in the time frame of this thesis, but we plan to implement it in the near future.
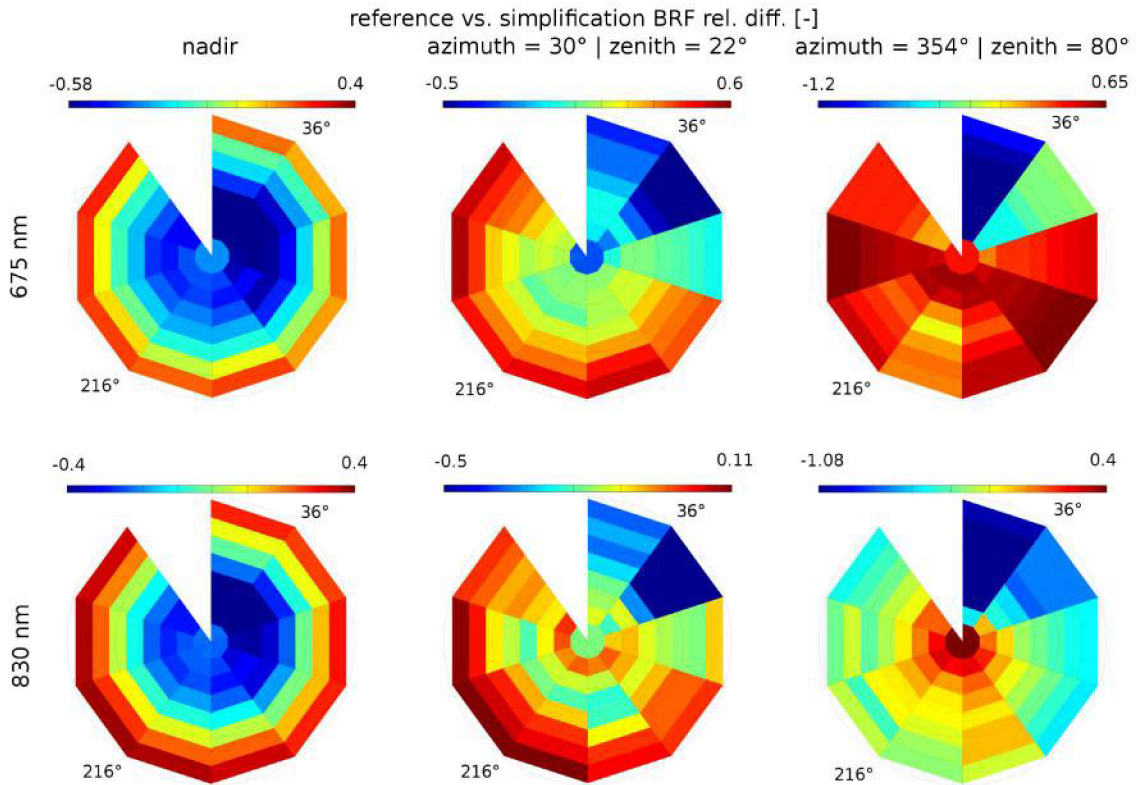
Figure 3.24: Comparison between reference needle shoot model (Figure 3.19a) and the best simplification (Figure 3.19c) influenced by solar illumination. On the radial coordinate is the sun zenith angle and on the angular coordinate is the sun azimuth angle. There is relative difference between these two shoot models for three different viewing angles and for two different bands in red (675 nm) and NIR region (830 nm).

3.4.4 Optimization at tree level

The main objectives of this optimization were:

- to compare shoot models at the tree level,

- to compare angular dependency at the tree level with the results at the shoot level,

- to compare DART simulations of 3D spruce model, 3D spruce model transformed to turbid cells, base spruce model, and airborne image.

For the comparison of the shoot models the following setup was used:

- nadir solar and viewing geometry,

- ground reflectance equal to 0,

- spectral range 400 − 1000 nm, and

- the optical properties generated by PROSPECT 3S RTM based on field data measured at the Bílý Kříž site in 2006 (Figure 3.34).

The compared values in this step were calculated as mean value of nonzero pixels from whole scene.

First we needed to find optimal cell size for this level. The cell size optimization was done only for the tree with needle shoot model (Figure 3.25a). The cell sizes was chose in range 0.1 − 0.5 m with step 0.1 m. The results illustrate that reflectance (BRF) decreases with bigger cell size (Figure 3.26).
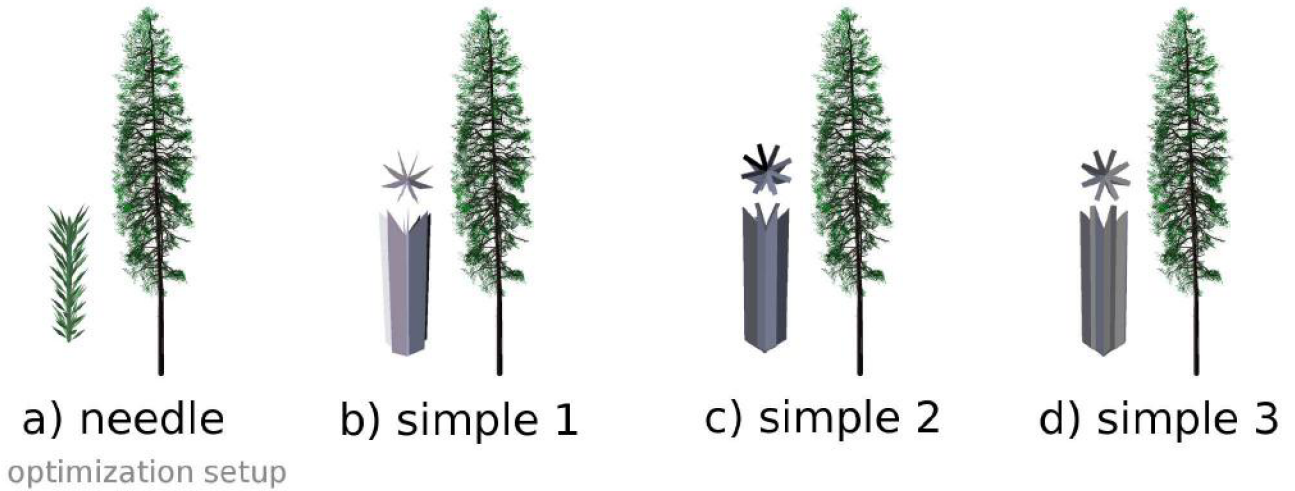
Figure 3.25: 3D spruce model with a) needle, b) the simple 1, c) the simple 2 , and d) the simple 3 shoot model. The optimization setup is shown at the bottom of the figure.
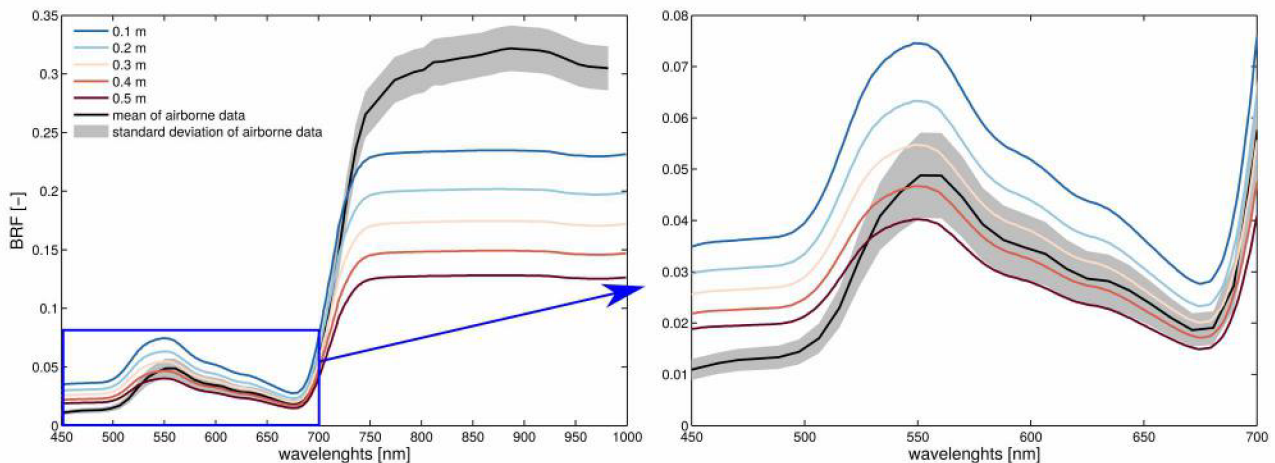
Figure 3.26: Cell size optimization results compared to the mean value of selected pixels from airborne image data. The pixels were selected as 3×3 average window with the center in the middle of tree crown.

The most suitable cell size was chosen based on selected pixels from airborne image. The pixels were selected as 3 × 3 average window with the center in the middle of tree crown. The simulations do not fit to the airborne data in VIS spectra well (Figure 3.26 and 3.31), but the NIR region of the spectra can be used as reference. The differentiation in VIS region was probably caused by optical properties generated by PROSPECT 3S RTM (Section 3.4.5). In the NIR

region of the spectra is seen that higher value of reflectance (BRF) are closer to airborne data. Therefore for the further analysis was chosen the smallest cell size.

Next the simulations with different shoot models were compared using chosen cell size of 0.1 m. This comparison shows that simulation with needle shoot model (Figure 3.25a) is significantly higher than the ones with simplified shoot models (Figure 3.27). The simulations with simple 1 (Figure 3.25b) and simple 2 (Figure 3.25c) shoot model are closer to the needle one than simple 3 shoot model (Figure 3.25d).
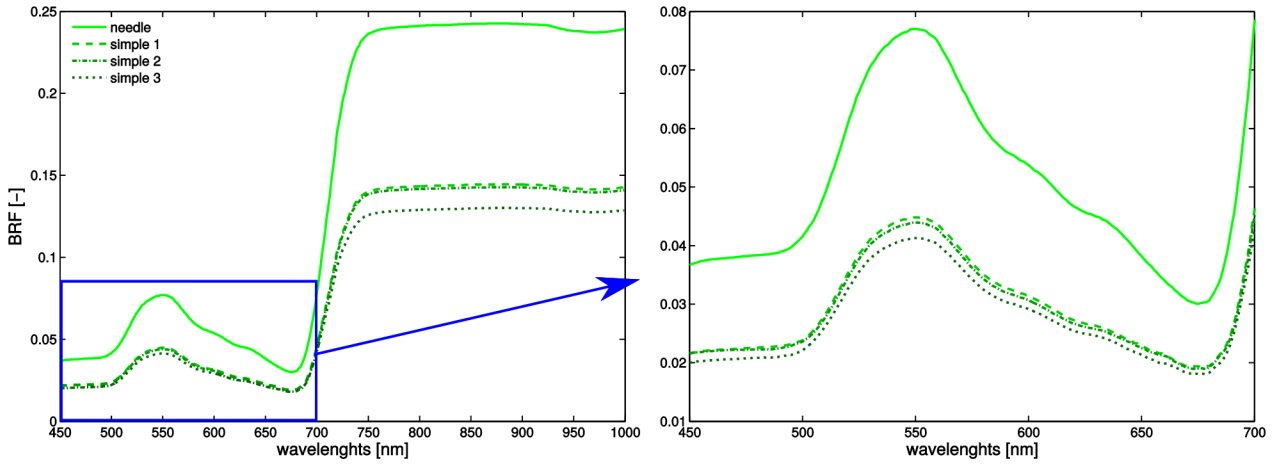

Figure 3.27: The mean reflectance (BRF) of nonzero values of whole scene. There were simulated single trees with different shoot models, and the ground reflectance is equal to 0.

The difference between simulations with simple 1 (Figure 3.25b) and simple 2 (Figure 3.25c) shoot model are not so significant in Figure 3.27, therefore relative difference were calculated between simulation with needle shoot model (Figure 3.25a) and the both last mentioned simplifications (Figure 3.28). This graph clearly shows that the simulation with the simple 1 shoot model (Figure 3.25b) is more similar to the one with needle shoot model.

The optimization at the shoot level showed strong angular dependency, compared to that on tree level. The shoot models were distributed in a crown with variation in angles (Section 3.3.3), therefore a certain degree of angular homogenization was expected. For the angular assessment only two shoot types were used, the reference needle (Figure 3.25a) and the simple 1 (Figure 3.25b) shoot model. This comparison was done the same way as at the shoot level (Figure 3.29):

- full illumination hemisphere: zenith angle with step 10° and azimuth angle with step 36°;

- two bands: 675 and 830 nm;

- three viewing angles: nadir, zenith angle 22° and azimuth 30°, and zenith angle 80° and azimuth 354°;

- reflectance (BRF) of whole scene.

the range of reflectance (BRF) values was chosen similar to the case of the shoot level for better comparison of this two cases. Therefore this time it is seen more homogeneous differences between simulations with needle and simple 1 shoot model.
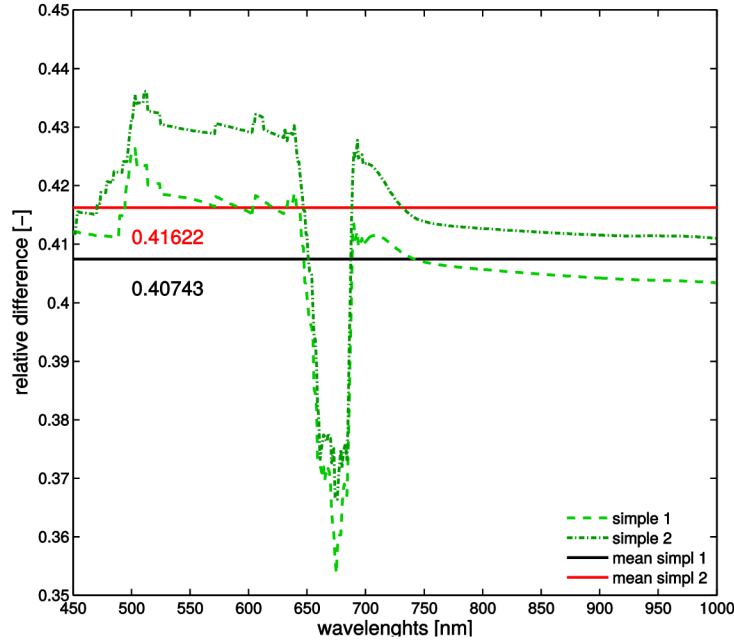
69

Figure 3.28: Comparison of simulations with 3D spruce model with the needle shoot model (Figure 3.25a) and simple 1 (Figure 3.25b) and simple 2 (Figure 3.25c) shoot model. The relative difference were calculated.

This part showed that the expected homogenization was realized at this level. Still there is a difference between the simulation with needle (Figure 3.25a) and simple 1 (Figure 3.25b) shoot model. The multiple scattering between the spruce needles and its angular anisotropy (Stenberg 1996, Smolander & Stenberg 2003, Rautiainen et al. 2012, and Mõttus et al. 2012) needs a complex solution using ray-tracing RT approaches, which was not further elaborated in this thesis due to limited computation resources.

Comparison of the 3D spruce model without turbid conversion with the base spruce model is possible only at this level. Due to limitation in computer resources it was not possible to assess it at the canopy level. In the last part of the assessment at the tree level following simulations were compared:

- 3D spruce model with needle shoot model (Figure 3.30a),

- 3D spruce model with simple 1 shoot model (Figure 3.30b),

- base spruce model (Figure 3.30c)

- 3D spruce model with needle shoot model transformed to turbid cells (Figure (3.30d), and

- 3D spruce model with simple 1 shoot model transformed to turbid cells (Figure (3.30e).

All the simulations were compared to the selected pixels from airborne image data. These selected pixels are the same as in the case of cell size selection. Because the comparison should be as similar as possible with airborne data, it was needed to set up different parametrization for DART scenes. The differences are in the ground reflectance and sun angles. The ground reflectance was set up according to real measured spectra and the sun angles was set up the same as in airborne image (Table 3.3).
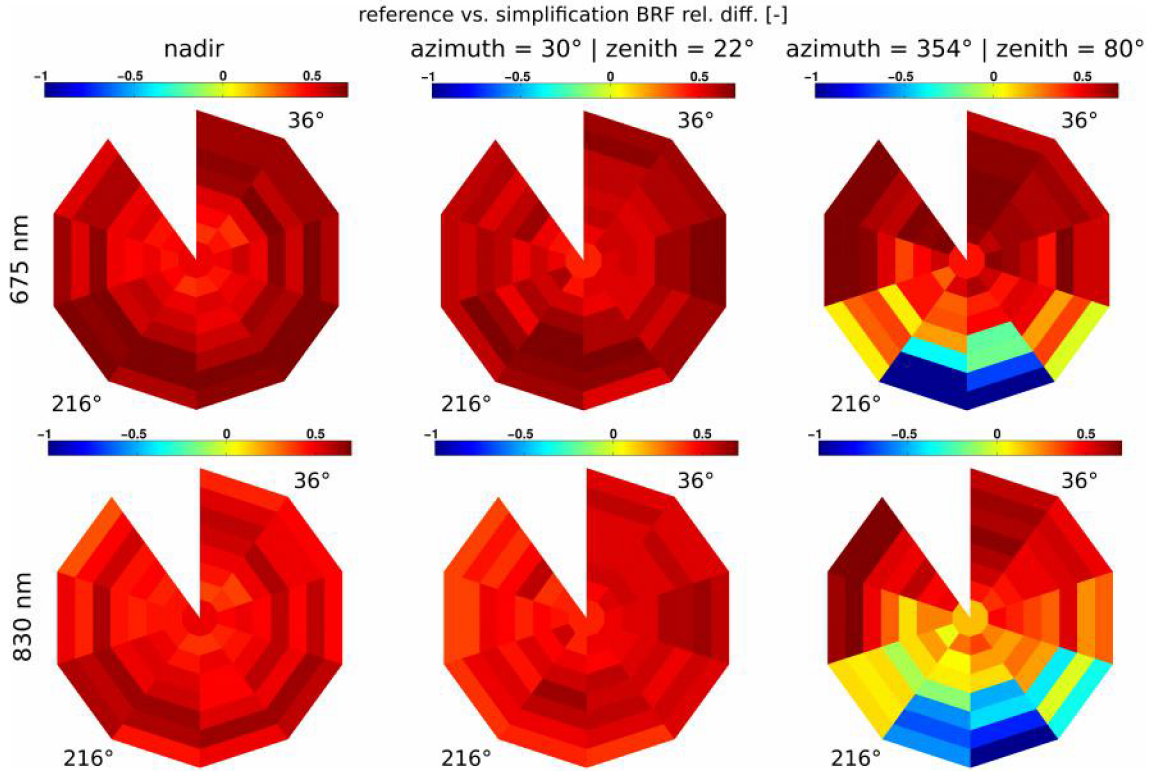
Figure 3.29: Comparison between tree with reference shoot model (Figure 3.19a) and the best simplification (Figure 3.19b) on tree level influenced by solar illumination. On the radial coordinate is the sun zenith angle and on the angular coordinate is the sun azimuth angle. There is relative difference between these two models for three different viewing angles and for two different bands in red (675 nm) and NIR region (830 nm). The range for this set of graphs were chosen close to the range of graphs on the shoot level (Figure 3.24) for better comparison of the results from these two optimizations.

The comparison shows the improvement of tree parametrization in case of 3D spruce model transformed to turbid cells (see Figure 3.31). The VIS spectral range does not fit well to airborne data as was mentioned above in this section due to used PROSPECT version for generation optical properties. Based on the NIR spectral range the most similar parametrization of spruce tree to airborne data was the one with 3D spruce tree with needle shoot transformed to turbid cells (Figure 3.30d). The 3D models do not fit well to airborne data. One reason of that can be that parametrization of these approach is need smaller cell size, but due to the computational requirements is not possible to simulate them with smaller cell size.

This optimization level showed that the best simplified shoot model on this level is the simple 1 (Figure 3.19b). This shoot model is even the least computationally demanding. The problem with nadir view from the needle level are less significant here because on the tree level are the shoots distributed with variation of angles. This allows to choose more simpler shoot model than the one chosen on shoot level.

Even if trees are modelled as 3D objects, the computation of radiative transfer in DART is done for discrete cells. The size of those cells controls amount of incident radiation and therefore multiple scattering between the 3D objects. For both 3D spruce models without transformation to turbid cells we observed lower reflectance values compared to the airborne data and spruce models transformed to turbid cells. This could be attributed to limited multiple scattering due to too coarse cell size (10 cm) chosen for this comparison. We expect that the finer

a) needle   b) simple 1   c) base model

d) needle   e) simple 1   f) airborne
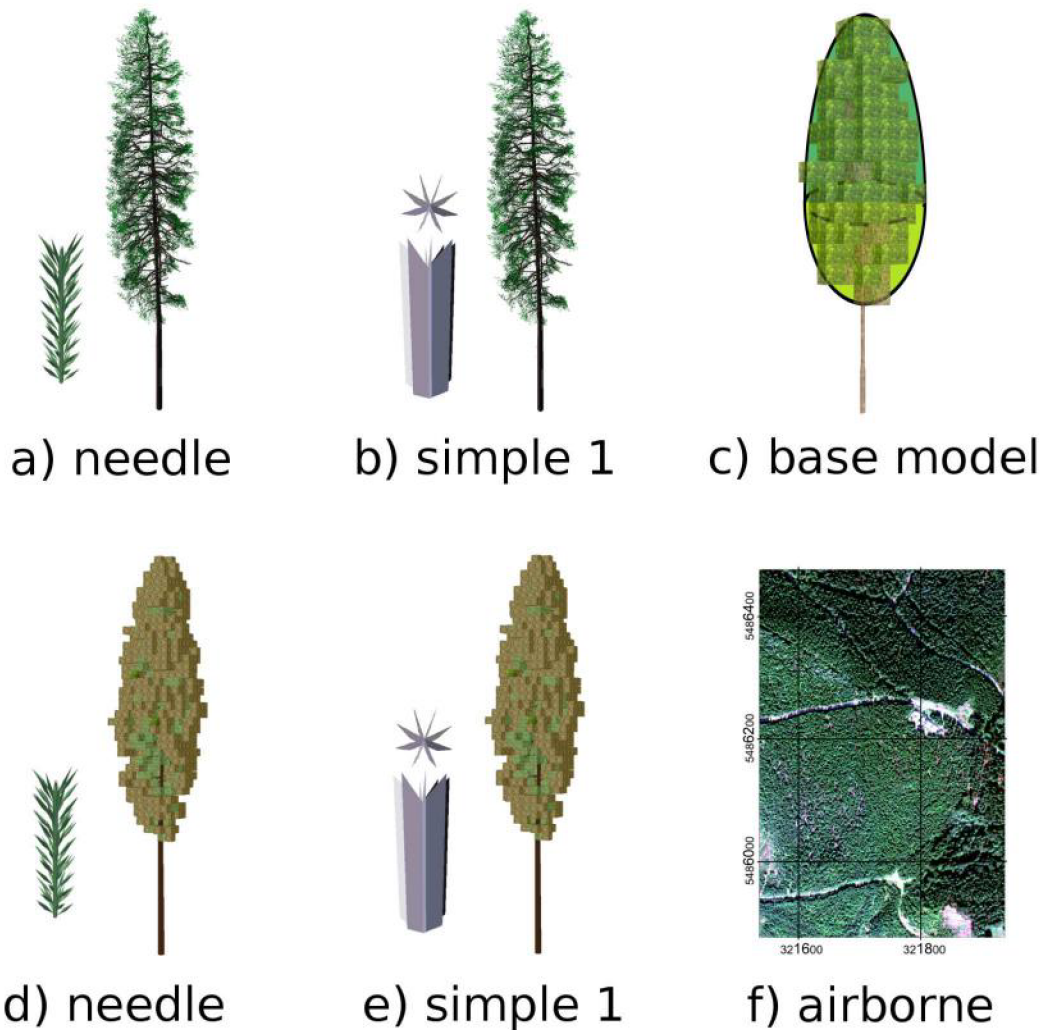
comparison setup

1 ground reflectances (vegetation), 1 viewing angles

Figure 3.30: Spruce models compared with selected pixels from airborne image data. a) 3D spruce model with needle shoot model, b) 3D spruce model with simple 1 shoot model, c) base spruce model, d) 3D spruce model with needle shoot model transformed to turbid cells, and e) 3D spruce model with simple 1 shoot model transformed to turbid cells, f) airborne image data. Comparison setup is shown at the bottom of the figure.

cell size could produce results closer to real airborne data, but it was unfeasible to compute it in this thesis with the current computer resources.

3.4.5 Optimization at canopy level

The previous two optimizations at the shoot and the tree levels were useful to assess the quality of the 3D tree model and its simplifications, but for the purpose of estimation of vegetation parameters from RS data it is needed to use the DART model at the canopy level, i.e., a scene with several trees. For the canopy level simulations, however, time and computer requirements need to be carefully considered. The aim of this comparison is to decide, if the transformation to turbid cells yields similar results to the RS data or if it is necessary to use 3D spruce models directly.
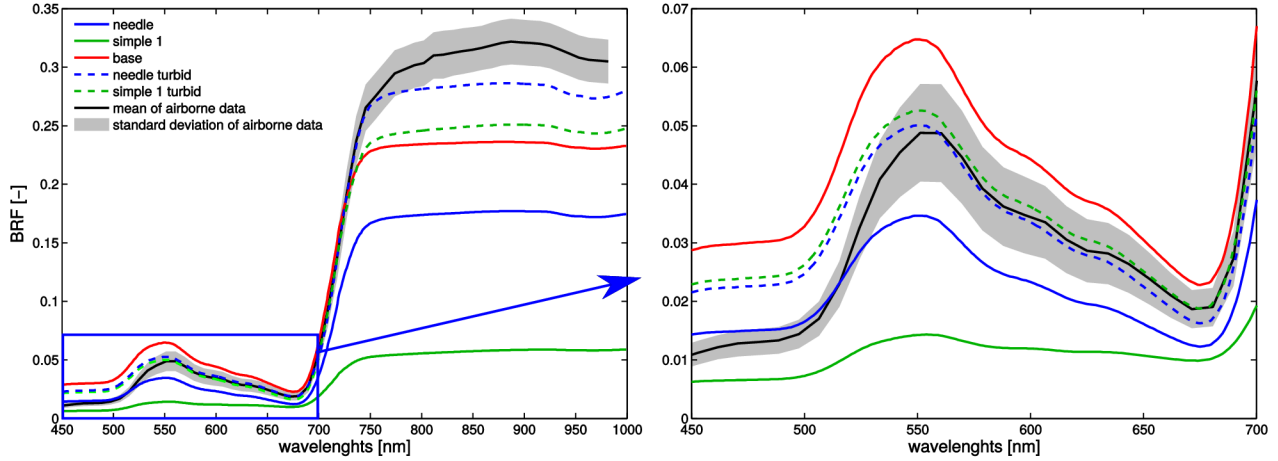
Figure 3.31: Comparison of selected pixels from airborne image data, their mean and standard deviation, with 3D spruce model with needle shoot model (needle), b) 3D spruce model with simple 1 shoot model (simple 1), c) base spruce model (base), d) 3D spruce model with needle shoot model transformed to turbid cells (needle turbid), and e) 3D spruce model with simple 1 shoot model transformed to turbid cells (simple 1 turbid).

At this level of comparison, it was not possible to simulate entire canopy scene using 3D spruce models, because it was too computationally demanding, but the canopy foliage objects had to be transformed to turbid cells. The comparison at this level was done for five DART canopy scenes which were compared with airborne data (Figure 3.32e). The five DART canopy scenes were:

- 3D spruce model with needle shoot transformed to turbid cells (Figure 3.32a),

- 3D spruce model with simple 1 shoot transformed to turbid cells (Figure 3.32b),

- 3D spruce model with simple 2 shoot transformed to turbid cells (Figure 3.32c),

- 3D spruce model with simple 3 shoot transformed to turbid cells (Figure 3.32d), and

- base spruce model (Figure 3.32e),

All simulations were conducted for the same basic scene parameters (summarized in Table 3.14), which represent the real spruce canopy at the Bílý Kříž site (Table 3.1) and the solar acquisition geometry of the airborne images (Table 3.3). Because the simulated DART canopy scenes are comparable with airborne RS images, the RS reference data for this comparison level were extracted from the airborne hyperspectral images acquired at the Bílý Kříž site (Section 3.2.3). The reference airborne spectra were extracted as an average and standard deviation of all pixels under an area of 100×100 m from images acquired in 3 date terms (2006, 2011, and 2013, Figure 3.35). Like this spatial and temporal variability of forest reflectance (BRF) was captured.

First we compare the simulated scenes with 3D spruce models transformed to turbid cells. Only the foliage part of the 3D spruce model was transformed. For the comparison we use airborne data from 3 years, previous DART scene with base spruce models, the new scenes with 3D spruce models with four shoot models (Figure 3.19), and the new scene with the first simplified shoot model (Figure 3.19b) and optical properties simulated by PROSPECT 5 (Figure 3.34). All the spectra mentioned above are in the Figure 3.35.
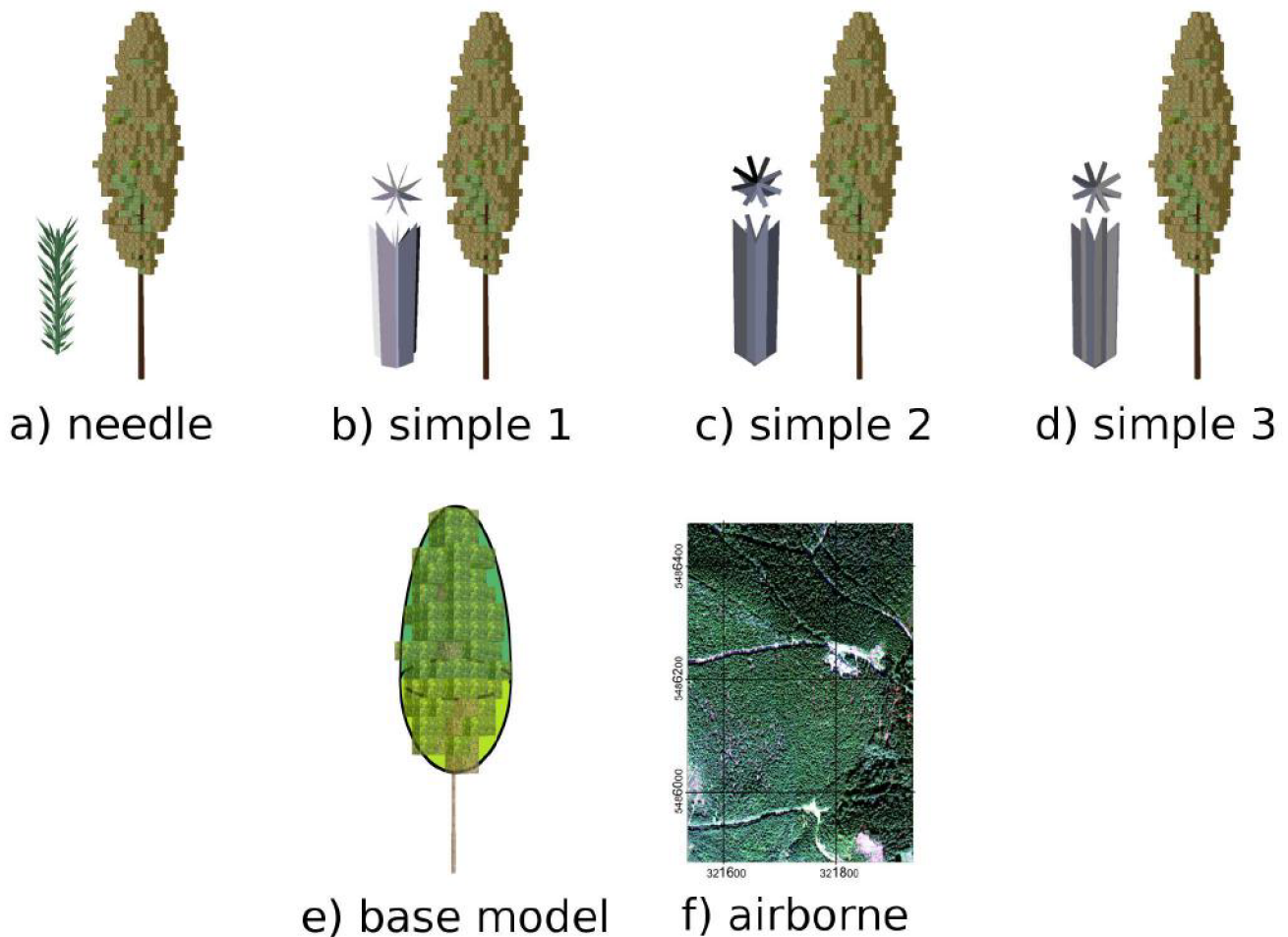
Figure 3.32: Spruce models used in comparison with airborne image data f). Used spruce models are a) 3D spruce model with needle, b) simple 1, c) simple 2, and d) simple 3 shoot model all transformed to turbid cells, and e) base spruce model. The comparison setup is shown at the bottom.

The main differences between the base and 3D spruce models are further in definition of the optical properties, leaf are index (LAI), and LAD. The optical properties in the base model were defined for three horizontal crown levels (exposed, transition, and shaded, see Section 3.4.2). The optical properties in the 3D models were separated to current-year and older shoots (Figure 3.8e). In this case we used the exposed optical properties for the current-year shoots and the transition optical properties for the older shoots. The optical properties were simulated by PROSPECT 3S RTM and were used in all five DART canopy scenes. Already at the tree level we noticed differences between simulated and airborne reflectance (BRF) in the VIS spectral region (Figure 3.26 and 3.31), what we have expected. It was due to the PROSPECT 3S RTM. Therefore, at this level we also simulated the DART scene with simple 1 shoot model (Figure 3.32b) with the PROSPECT 5 RTM simulated optical properties. The difference between PROSPECT 3S and 5 input optical properties is shown in Figure 3.34.

In case of the canopy scene with the base spruce model (Figure 3.32e), the LAI and LAD parameters were setup directly in the DART model. The LAI was equal to 7 and the LAD was de-

parameter	value
scene dimension $x \times y$ [m]	10×10
cell dimension $x \times y \times z$ [m]	$0.5 \times 0.5 \times 0.5$
slope [°]	15
exposition	southern
scene canopy cover [%]	80
LAI	7
number of trees	26
sun zenith angle [°]	46.16
sun azimuth angle [°]	177.04

Table 3.14: DART parametrization of the whole scene - general parameters.

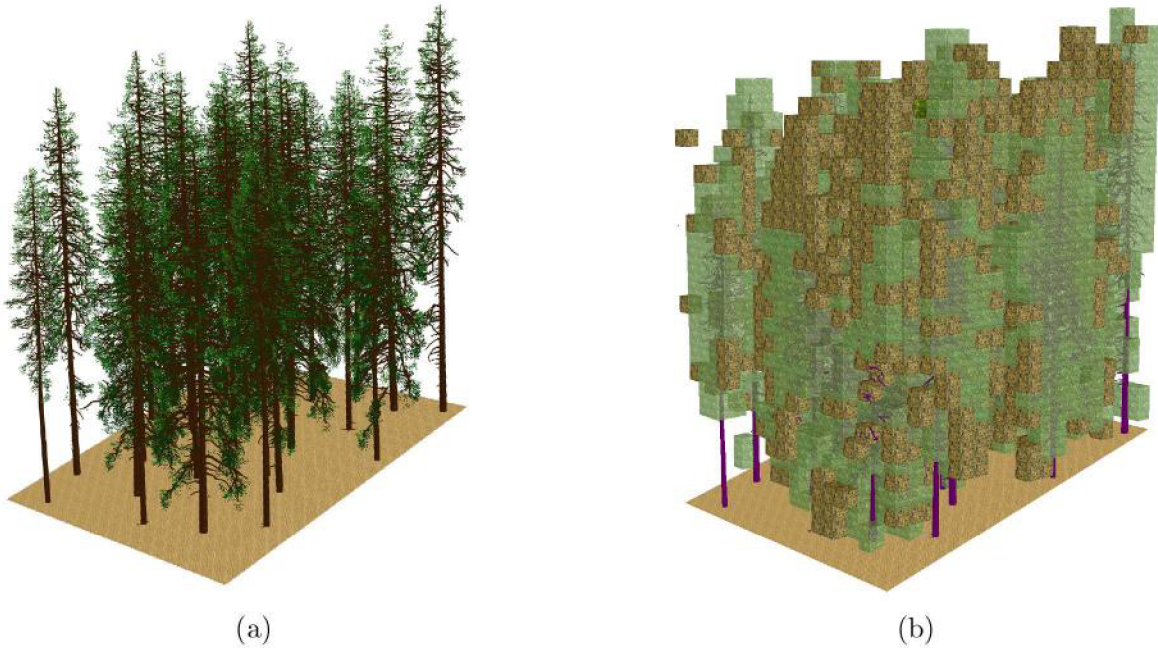(a)   (b)

Figure 3.33: DART scenes of spruce site a) with 3D models of trees and b) with 3D models of trees transformed to turbid cells.

fined as spherical distribution. In case of the canopy scenes with 3D models (Figure 3.32a − d), LAI and LAD parameters were calculated directly from 3D models. The calculated LAI was different for each shoot model (Table 3.15) because the calculation takes into account all the facets of the shoot objects. This causes that in case of needle shoot (Figure 3.19a) and simple 3 shoot (Figure 3.19d) the LAI is more than twice higher that that of simple 1 shoot model. It was complicated to control either tree or canopy LAI for 3D spruce model with two sets of shoot objects (current-year and older) and this functionality of the DART model should be addressed in future.

The results show the comparison between airborne reference data and DART simulated canopy scenes (Figure 3.36). From the first glance the most similar simulations to the reference airborne data are those with simple 1 and simple 2 shoot models, but the closer look into VIS spectral region revealed differences, which could be attributed to optical properties simulated by PROSPECT 3S RTM. The canopy spectra with optical properties simulated by PROSPECT 5 RTM resembles better the reference airborne data in the VIS spectral region and fits well in the NIR spectral region too.
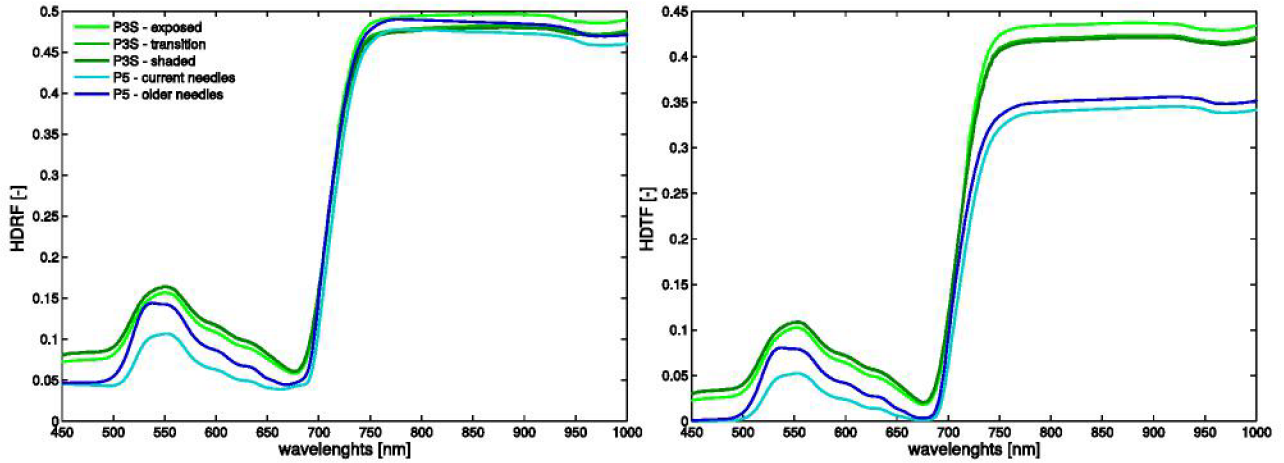
Figure 3.34: Input optical properties for needles, shoots or turbid cells used in DART simulations. The optical properties generated by PROSPECT 3S (P3S) for exposed, transition, and shaded tree crown level are in different shades of green. These optical properties are generated with chlorophyll content of 42.55 $\mu g\,cm^{-2}$. The optical properties generated by PROSPECT 5 (P5) for current needles with chlorophyll content of 42.47 $\mu g\,cm^{-2}$ and older needles with chlorophyll content 57.62 $\mu g\,cm^{-2}$ are in shades of blue.
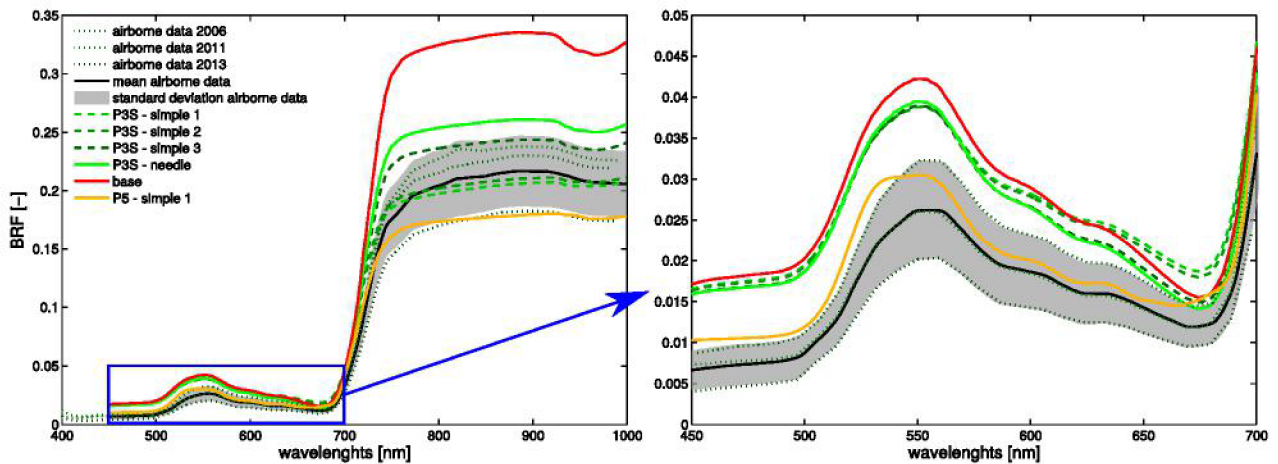
Figure 3.35: Comparison of airborne data and DART simulations with different type of tree parametrization. There are showed three airborne data from years 2006, 2011, and 2013, their mean and standard deviation. DART simulations are with base spruce models, with needle, simple 1, simple 2, and simple 3 shoot model, where optical properties were simulated by PROSPECT 3S (P3S). Last is simulation with simple 1 shoot model but the optical properties were simulated with PROSPECT 5 (P5). On the left side are the spectra, and on the right side are the spectra only in VIS region of the spectra.

The absolute and relative difference between mean of airborne data and each DART simulation were calculated (Figure 3.37). From these graphs is seen the significant improvement in the NIR region of spectra in case of all new scenes with 3D spruce models transformed to turbid cells. The behavior in the VIS region is influenced more by the PROSPECT model version rather than the spruce model. The comparison showed that using 3D model with simple 1 or simple 2 shoot model is still the best choice.

76

shoot model	base	needle	simple 1	simple 2	simple 3
LAI	7	15.61	6.5	7.12	14.08

Table 3.15: The LAI values calculated by the DART model from 3D models. The simulations are labeled as in Figure 3.35. The LAI values are independent on optical properties, therefore there is no need to differentiate PROSPECT versions.
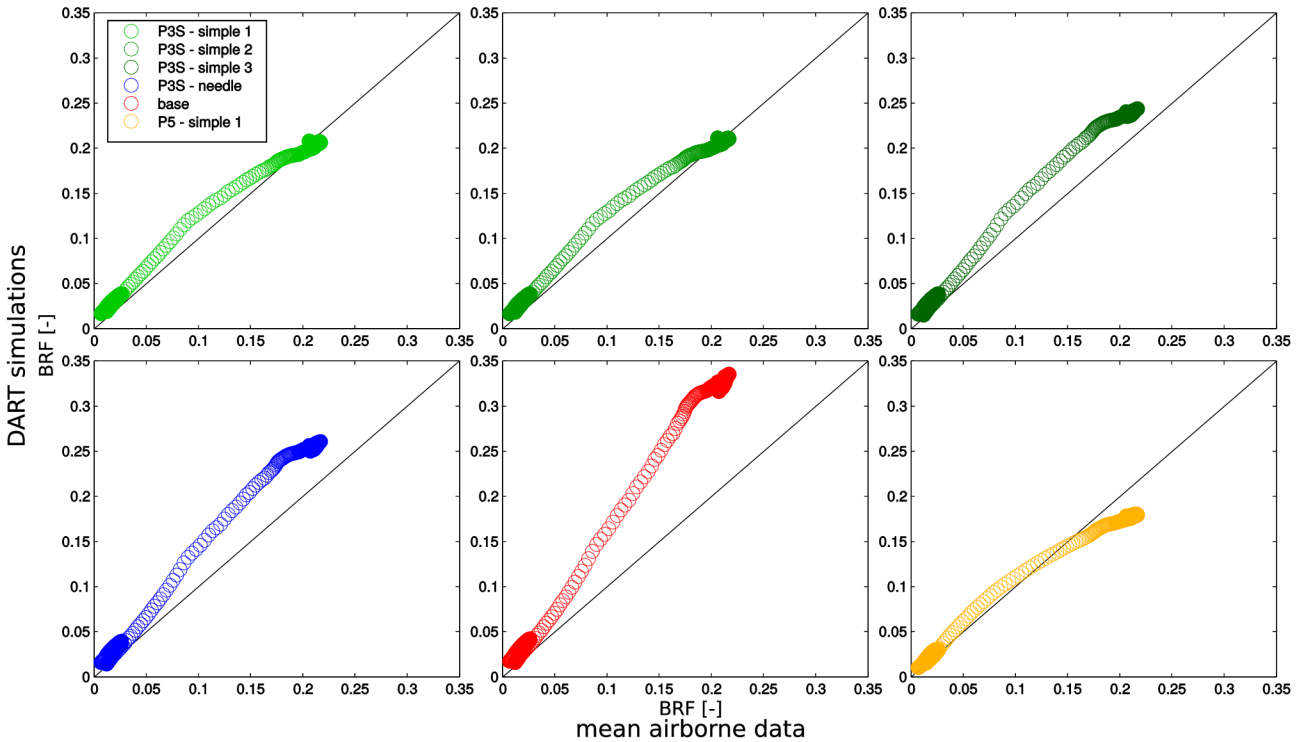

Figure 3.36: The mean value of airborne mean data and each DART simulation plotted against each other. The legend of the data are the same as in Figure 3.35.
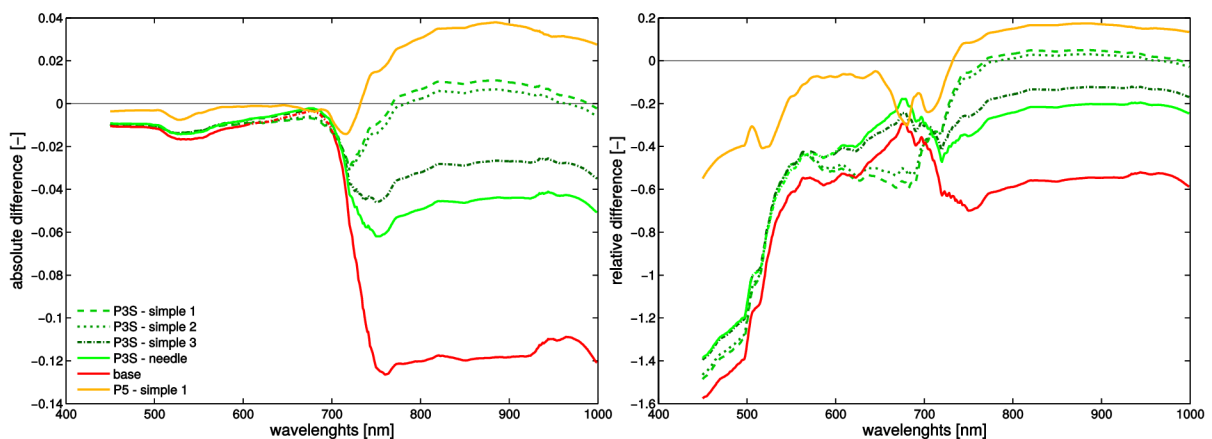

Figure 3.37: The absolute (on the left) and relative (on the right) difference between mean value of the airborne data and each DART simulation. The legend of the data are the same as in Figure 3.35.

RMSE values between mean of airborne data and each DART simulation is also calculated (Table 3.16 and Figure 3.38). Also this graph shows that the simple 1 and simple 2 shoot model give better results than the original base spruce models.

shoot model	simple 1	simple 2	simple 3	needle	base	simple 1
used PROSPECT version	3S	3S	3S	3S	3S	5
RMSE	0.0106	0.0100	0.0240	0.0349	0.0828	0.0222

Table 3.16: The RMSE values between mean of airborne data and each DART simulations. The legend of the data are the same as in Figure 3.35.
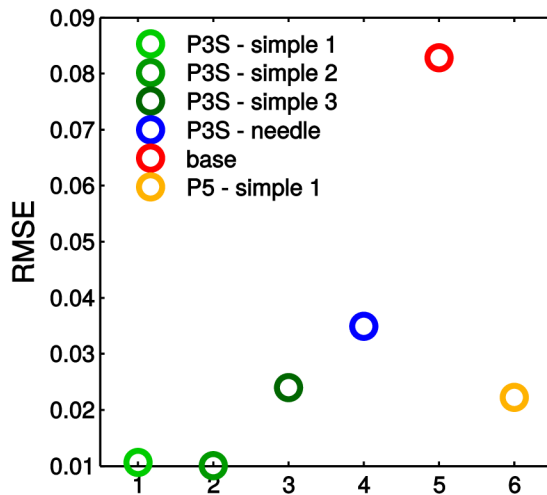
Figure 3.38: The RMSE values between mean of airborne data and each DART simulations. The legend of the data are the same as in Figure 3.35.

Nevertheless the discrepancies appear in VIS spectral region. They are probably caused by optical properties simulated with PROSPECT 3S RTM model (Figure 3.34).

Conclusion of this section is that the improvement in DART simulation is significant with used 3D spruce models even if the foliage part of the spruce model is transformed to turbid cells and are much closer to the airborne data. Therefore it could be concluded that there is no need to use 3D spruce models directly without transformation to turbid cells. The time and computation demands are significantly lower.

Although the simulations with needle shoot model was treated as the references in case of the shoot and the tree level, the results at the canopy level show that this case is worse than the simulations with shoot simplifications. This behavior could be caused by way in which the LAI is calculated when 3D model is transformed to turbid cells. The LAI calculated from 3D spruce model is shown in Table 3.15. The best shoot model for this level is the simple 1 or simple 2. If we compare the time and computation demands for simulations used these two shoot models there is better to use the model with less facets. It means that the best setup is to create DART scene with 3D spruce models with simple 1 shoot model (Figure 3.19b) and let the DART model to transform the foliage part to turbid cells.

3.4.6 Main outcome

Since the reconstructed 3D spruce model was too complex for direct implementation in the DART model, the key outcome of this part was the optimized 3D spruce representation.

The optimization at the shoot level used two new simplified shoot models (labeled as simple 2 and simple 3) to replace the detailed reference needle shoot model. A high agreement with the reference was found for the simple 2 shoot model. However, a strong angular dependency was still observed when simulating single shoots, with the largest differences in the nadir viewing angle caused by regular structure of planes in the simplified shoot models. Less angular dependencies were expected at the tree level, because of larger angular variability in distribution of shoot within the crown. Contrary to the shoot level, the optimal solution at the tree level was obtained with the simple 1 shoot model, which yielded slightly better results than the simple 2 model. Results confirmed the angular homogenization of a single tree crown reflectance (BRF).

The goal of the canopy level optimization was to decide, if the 3D spruce models transformed to turbid cells are sufficiently representative for accurate estimations of selected vegetation parameters from RS data. The choice of the optimal tree parametrization was based on comparison of reflectance simulations using all four shoot models (Figure 3.19) with the airborne data of a spruce forest. The results revealed that the 3D spruce model transformed to turbid cells significantly improved forest canopy reflectance (BRF) simulation. This spruce model with the simple 1 shoot model produced simulated reflectance, which, compared to the results obtained with the base spruce model, fits better with real airborne hyperspectral image data. RMSE values calculated between mean of airborne data and DART canopy simulations confirm that spruce model with simple 1 or simple 2 shoot model with RMSE values 0.0106 and s0.0100 fit better to real airborne hyperspectral data than the base spruce model with RMSE value 0.0828 (Table 3.16 and Figure 3.38).

The outcome of this part is not definite. As the DART model is being constantly updated and its computational efficiency improved, a more efficient 3D spruce model can be defined in a near future. It is expected that the computation efficiency of the DART model will soon allow to simulate canopy scenes created form geometrical objects without the turbid cell transformation necessity.

3.5 Estimation of quantitative vegetation parameters

The main goal of this study was to test if the optimized 3D spruce model improves the estimation of vegetation parameters (i.e. Leaf chlorophyll a+b content (Cab) and LAI) from satellite observations. In order to assess the improvement, the vegetation parameters were estimated by two look-up tables (LUTs), which were generated by two parameterizations of spruce canopy in the DART model (base versus 3D spruce model). The first parameterization of the spruce canopy was based on the base spruce model (described in Section 3.4.2), the second parameterization was based on the optimized 3D spruce model (described in Sections 3.4.3, 3.4.4, and 3.4.5).

This section is composed of three parts:

- Creation of the two types of LUTs (Section 3.5.1).

- the retrieval of vegetation parameters from Sentinel-2 (S2) images by applying support vector machines (SVM) to both LUTs and necessary optimization of the SVM input parameters (Section 3.5.2).

- Last, validation of estimated parameters with the field data acquired at the Bílý Kříž site (Section 3.5.3). The last step helped to evaluate the impact of 3D spruce model and its DART parameterization, which was newly developed in this thesis.

3.5.1 LUT creation

The LUTs were created within the framework of two international projects (RedEdge - RED-EDGE-CG-CESBIO-ATBD-03-0002 and HYPOS - AO/1-8345/15/NL/LvH projects, European Space Agency), therefore they differed based on project specifications such as in spruce model parameterization, LUT structure, version of the DART model used for its creation etc. The LUT with the base spruce model was tailored to airborne and field data from the Bílý Kříž site in 2006 (see Sections 3.2.2 and 3.2.3). The LUT with the 3D spruce model transformed to turbid cells was tailored to satellite and field data at the same study site, but in 2016 (see Sections 3.2.2 and 3.2.4). For LUTs creation the newest version of the DART model available at the time when they were simulated was used. Some improvements of the DART model were specifically made for the purpose of these projects. Most of improvements are made in sense of computation efficiency.

3.5.1.1 Base spruce model

These LUT simulations were made with the DART model version 5.5.1 v494 (released in 2014). Parameterization of the spruce canopy in the DART model using the base spruce model is already described in earlier Sections 3.4.2 and 3.4.5. In the following paragraphs only the variable parameters of the DART scene will be described and they are summarized in Table 3.17. Canopy cover varied between 50 and 95 % in step of 15 %. Canopy cover below 50 % were not considered, because the reflectance (BRF) of such a forest stand is formed prevailingly by the forest understory, which is not included in our DART scenes.

The LAI range (3 – 10) was selected based on real measurements (Table 3.1) and available literature (Leuschner et al. 2006; Pokorný and Stojnič 2013, see Table 3.17). Typically spruce stands are characterized by higher LAI values. Similarly to canopy cover, we did not include simulations of $LAI < 3$ as they would be too much affected by the understory plants and wooden elements (adapted from Jan et al. 2016).

Four scene topography categories (flat, south, north, and east oriented slopes) were considered in order to compensate for different illumination conditions in mountain regions.

parameters	base model	3D model
canopy cover (CC)	50, 65, 80, 95 %	
LAI	3 – 10 with step 1	
topography (topo)	flat, south, north, and east slope	
leaf optical properties (lop)	900	464*
combinations	(topo · CC · LAI · lop)	(topo · CC · (comb(LAI and lop)))
number of simulations	115 200	7 424

Table 3.17: Structure of DART simulated spectral database. (*) *leaf optical properties in case simulations with 3D spruce models are generated together with the LAI values. That means, for each case of generated leaf optical property was randomly chosen the LAI value from range 3 – 10. Instead of the case of simulations with base spruce models they were generated set of leaf optical properties and this set were assigned to each LAI level.*

Leaf optical properties that were used as inputs into the DART model were simulated using PROSPECT 3S, which was specifically adjusted for the Norway spruce needles by Malenovský et al. (2006) (Section 3.4.2). In case of the base spruce model DART is able to separate the tree crown in horizontal layers, therefore the leaf optical properties were defined for each crown level as described in Section 3.4.2. The adjusted PROSPECT 3S simulates optical properties only in the spectral range between 450 and 1000 nm. Therefore, all DART simulations were also restricted to the maximum wavelength of 1000 nm. The spectral sampling was 1 nm.

Meaningful combinations of PROSPECT input parameters were randomly derived using the Matlab function `mvnrnd`, which generates multivariate normal random values. This function takes into account covariance computed among the measured PROSPECT input parameters. The function generated an initial pool of 50 000 input combinations that were restricted by realistic min – max ranges defined according to available literature (Stuckens et al. 2011, Feret et al. 2008, 2011, and Ciganda et al. 2009) or by available experimental measurements (Figure 3.39).

Figure 3.39: Distribution of in-situ measured leaf biochemical properties Cab - chlorophyll content, Cw - water content, Cm - dry matter content for spruce needles.

Since one of the estimated parameters is Cab, it was essential to ensure that the sampling space of possible chlorophyll values was spaced equally. Therefore, the initial pool of input combinations was divided into equally spaced groups of Cab values (e.g. Cab varied between 10 and 100 $\mu g\,cm^{-2}$, we obtained nine groups representing nine intervals of 10 $\mu g\,cm^{-2}$ each). From each group ten PROSPECT input combinations were then randomly selected resulting in 900 combinations scenes. Distributions of all input parameters derived by PROSPECT are shown in Figure 3.40.
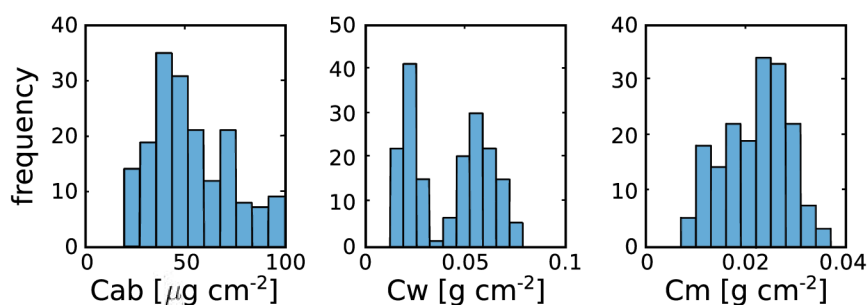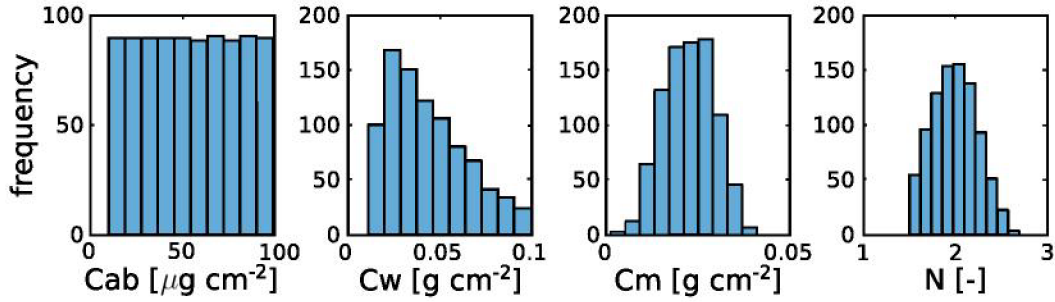
Figure 3.40: Distribution of leaf biochemical and structural properties Cab - chlorophyll content, Cw - water content, Cm - dry matter content, N - structure that were used to simulate leaf optical properties in PROSPECT model in case of base spruce models.

3.5.1.2   3D spruce model

These LUT simulations were made with the DART model version 5.6.3 v858 (released in 2016). The setup this LUT structure is almost similar to the previous one with base spruce model, the major difference is in simulation of input optical properties and distribution of the LAI (Table 3.17). The optical properties were simulated using the PROSPECT 5 RTM (Jacquemoud & Baret 1990; Feret et al. 2008). The PROSPECT 5 model calculates leaf reflectance (HDRF) and transmittance (HTRF) in the range from 400 to 2500 nm. The use of PROSPECT 5 was justified by the ESA project requirements to simulate full spectral range (400 – 2300 nm) and to include leaf carotenoids (Car) as a variable.

Needles of spruce trees were divided into two categories, current-year needles growing at crown periphery (20 %) and older needles growing inside the crown (80 %) (Section 3.3.3). The older needles generally have higher Cab, carotenoid (Car) and dry matter (Cm) content (Homolová et al. 2013) and this was reflected in the distribution of PROSPECT 5 input parameters (Figure 3.41).
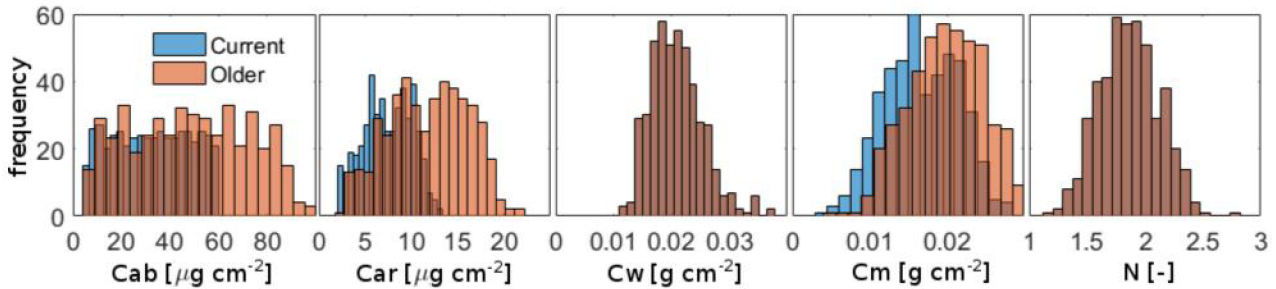
Figure 3.41: Distribution of leaf biochemical and structural properties Cab - chlorophyll content, Car - carotenoid content Cw - water content, Cm - dry matter content, N - structure that were used to simulate leaf optical properties in PROSPECT 5 model in case of 3D spruce models transformed to turbid cells.

Other difference is in the distribution of the LAI. In the case of simulations with the base spruce model generated set of leaf optical properties were assigned to each LAI level. But in case of simulations with the 3D spruce model the LAI values were randomly chosen from the range 3 – 10 and assigned to each generated leaf optical properties. That enabled a smaller size of the LUT.

3.5.1.3 Common computer requirements and LUT post-processing

Computation of forest scene is very computationally demanding, therefore both cases were simulated at MetaCentrum, Czech national grid infrastructure for distributed computing (www.metacentrum.cz). Both LUTs were generated in different years, different DART model versions were used to simulate the LUTs. Due to the continual development of the DART model, the computation requirements in 2016 for the LUTs based on the 3D model significantly decreased. Computer requirements of MetaCentrum to simulate both LUTs are summarized in Table 3.18.

requirements	base model	3D model
used DART version	5.5.1 v494	5.6.3 v858
year of DART version releasing	2014	2016
number of sequences per canopy cover and topography	24	20
number of simulations per sequence	300	23
number of simulations run in one time	8	2
RAM needed for one parallel computation	32 GB	25 GB
disk capacity required to store results of one sequence	100 GB	1 GB
computation time per sequence	10 − 48 h	6 − 14 h

Table 3.18: Optimal computational requirements for DART simulations at MetaCentrum for two LUTs: with the base spruce model and with the 3D spruce model transformed to turbid cells. The differences are due to the improved version of the DART model released in 2016.

The simulated spectral signatures by the DART model had the original spectral resolution of 1 nm. This spectral resolution was not suitable for further analysis and therefore the spectral databases were resampled according to S2 images, using Gaussian convolution (Huck & Berthelot 2015). The spectral resampling allows us to retrieve from real S2 images. Description of computational requirements was adopted from Homolová et al. (2015b).

3.5.2 Estimation of Cab and LAI

The Cab and LAI retrievals were implemented using SVM (Chang & Lin 2011), as these algorithms represent a good compromise between computation cost, efficiency and accuracy. SVM are kernel-based computer learning algorithms used widely for solving N-class classifications or regression problems (Smola & Schölkopf 2004, Section 2.3.4).

Since we used the radial basis function kernel, the most significant parameters were: i) the cost value of a kernel (parameter C) and ii) the parameter γ defining the kernel function. It was necessary to find the most optimal values of C and γ to ensure the best possible performance of SVM when applied on real datasets. The optimization procedure used 5-fold cross-validation and it was applied on a selected subset of LUT, i.e. training dataset. The highest computed coefficient of determination (r^2) and the lowest mean square error (MSE) pointed out the optimum solutions of both parameters simultaneously. An envelope of optimum solutions was identified as the 25% of C, γ combinations yielding the highest r^2 (Figure 3.42).

Since $C > 15$ caused overtraining of the SVM, it was decided to fix the optimal value of C equal to 10. The optimum values of γ parameter were less stable and varied. It was inefficient to determine the single most optimal value of γ, therefore γ varied within a restricted range of optimal values, which was between -5 and 5 with steps of 1.

The SVM was trained with 1000 samples and applied on S2 image data for both cases of LUT. The estimated values of the Cab and LAI were filtered by 3×3 median filter `medfilt2`
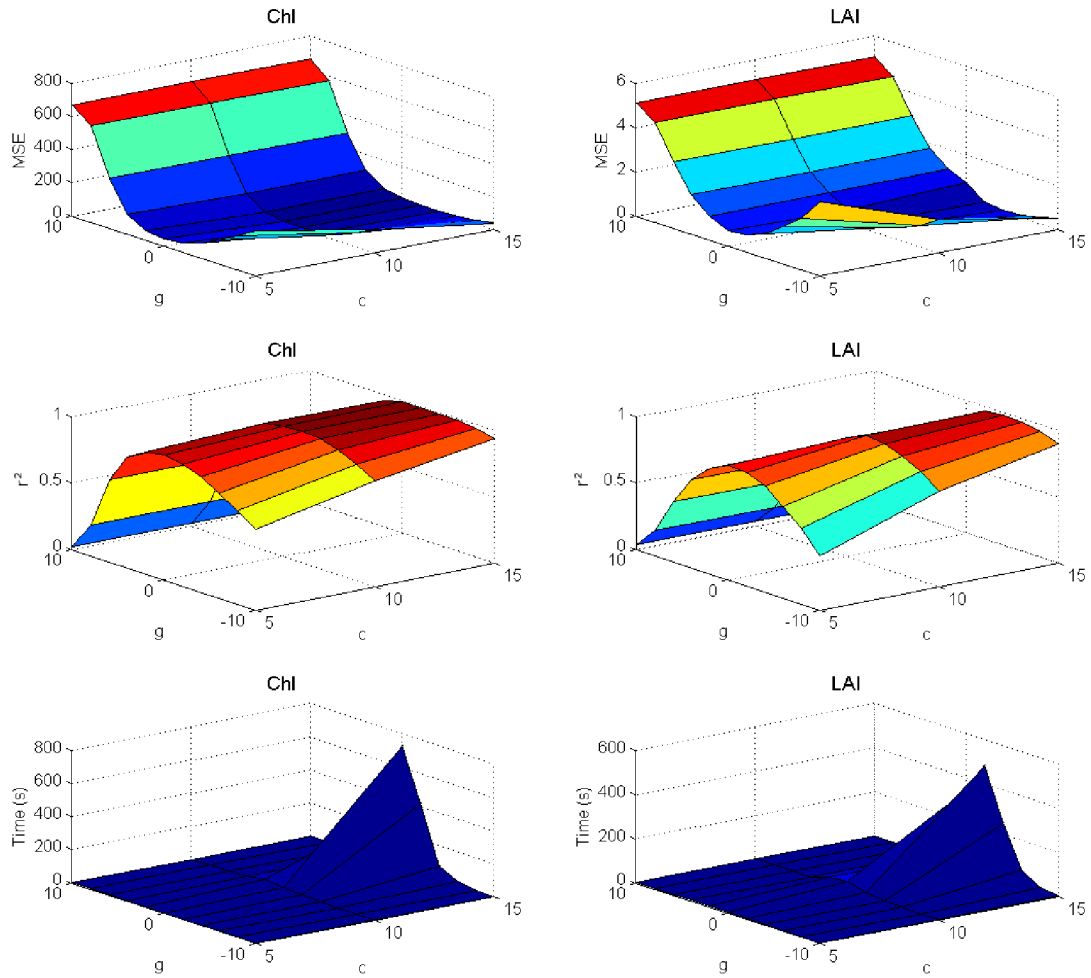
Figure 3.42: Results of the SVM kernel optimization for retrieval of Cab - leaf chlorophyll content, LAI and leaf area index using the S2 band. The upper graphs show results for MSE, the middle graphs for the coefficient of determination (r^2) and the lower graphs for time of processing.

in Matlab. For better visualization the results of the estimated Cab and LAI were displayed in discrete ranges (according to expected real values see Figure 3.39). Therefore the pixels with extreme values were not classified. Finally, the results were restricted to forested areas only. The forested pixels were identified using supervised maximum likelihood classification method. Final maps of estimated Cab and LAI from both LUTs are shown in Figures 3.43 and 3.44.

The results from LUT with 3D spruce model are more consistent and closer to the real values. The validation according to field data are described in next Section 3.5.3.

3.5.3 Validation against the field data

Validation of the Cab and the LAI retrievals from S2 images were done with the field data that were measured almost synchronously with S2 acquisition in summer 2016 (see Section 3.2.2). The field sampling plots are better distributed within the study area than in 2006 (see Figure 3.5). The ten years difference between forest height captured by the two LUTs is not such a complication for the Cab and LAI estimation, because the S2 image subset contains spruce forests of different heights. The difference in variability of the field data measured in 2006
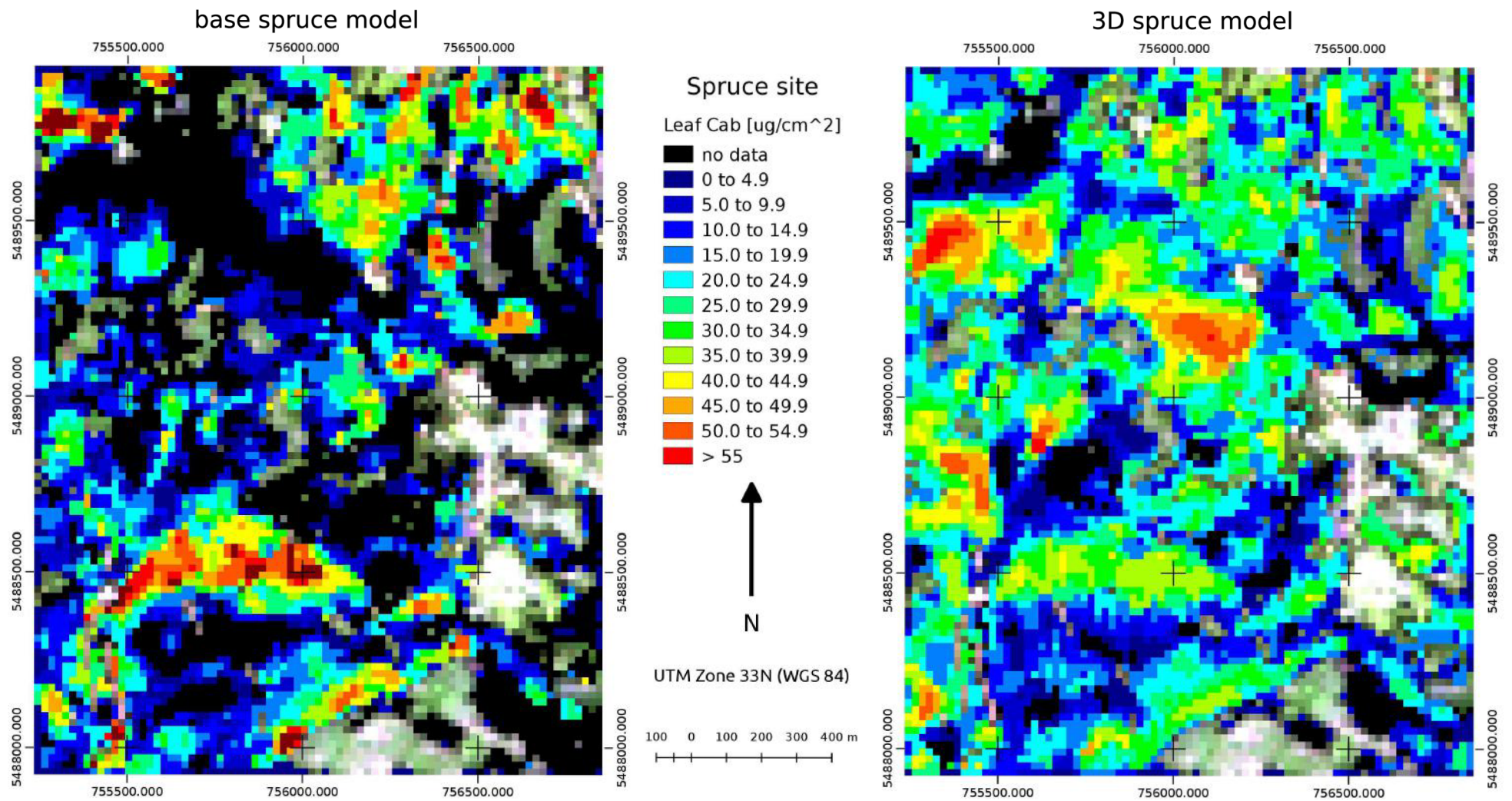
Figure 3.43: Estimated Cab content. The map on the left was calculated from LUT with base spruce models, the map on the right was calculated from LUT with 3D spruce models transformed to turbid cells.
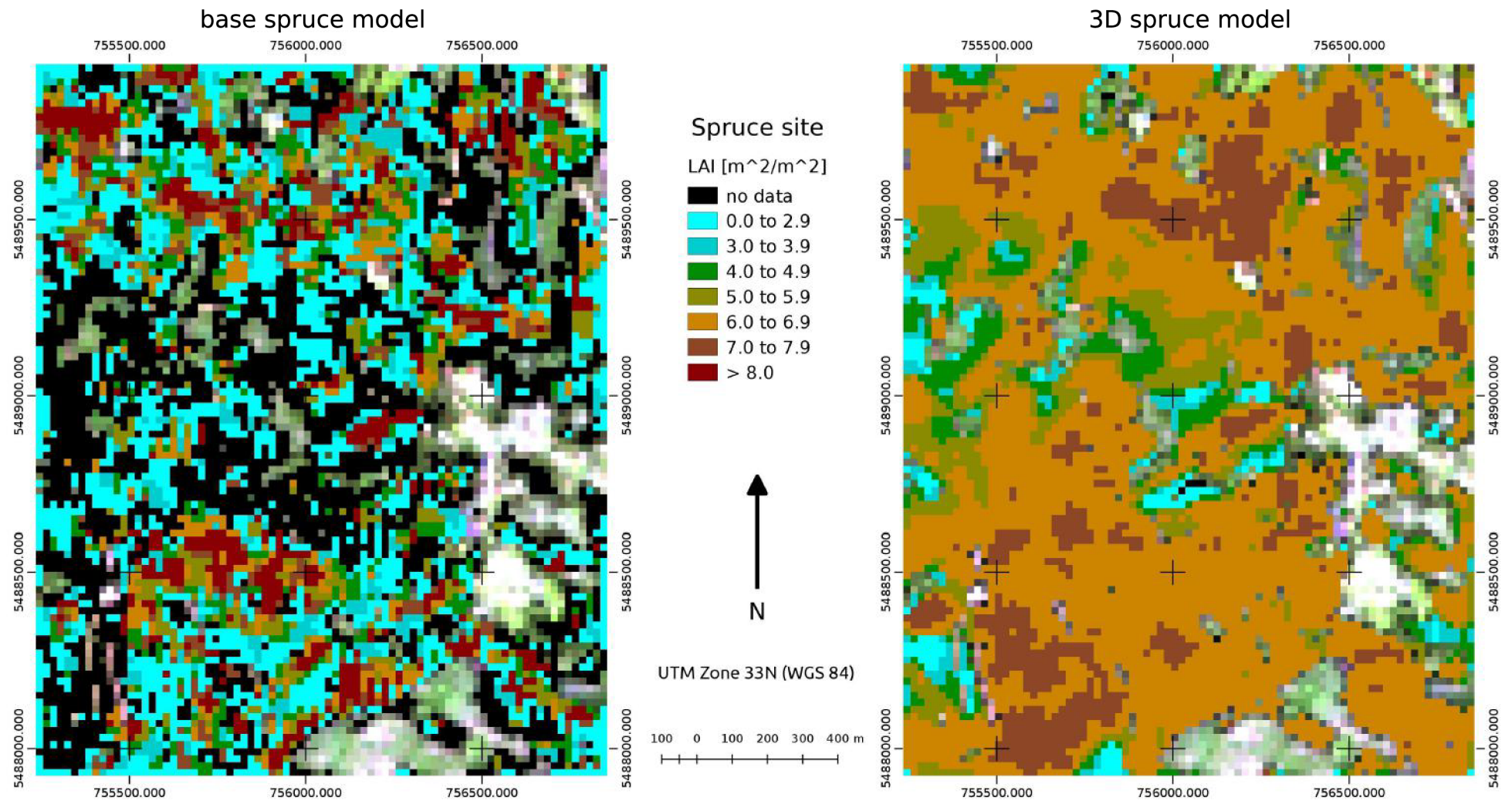
Figure 3.44: Estimated LAI. The map on the left was calculated from LUT with base spruce models, the map on the right was calculated from LUT with 3D spruce models transformed to turbid cells.

and 2016 is not significant for the purpose of this study (cf. Figures 3.39, 3.40, and 3.41).

For validation of estimated Cab from S2 images with the pixel size of 20×20 m, mean Cab value was computed from three sample trees representative for each plot (2×2 S2 pixels). Mean Cab exhibited low variability among the plots, the mean value hanged between around Cab = $30 - 40 \ \mu g \, cm^{-2}$. The LAI values were computed per plot and varied in range $5 - 9 \ m^2 \, m^{-2}$. For purpose of the Cab and LAI validation there are only seven values available. The number is very low, since gathering of this type of data is very time consuming. The validation was realized as a scatter plot between the measured and estimated values (Figure 3.45). Furthermore, RMSE values were computed for all combinations of parameters and used spruce models.

(a) Validation of Cab.
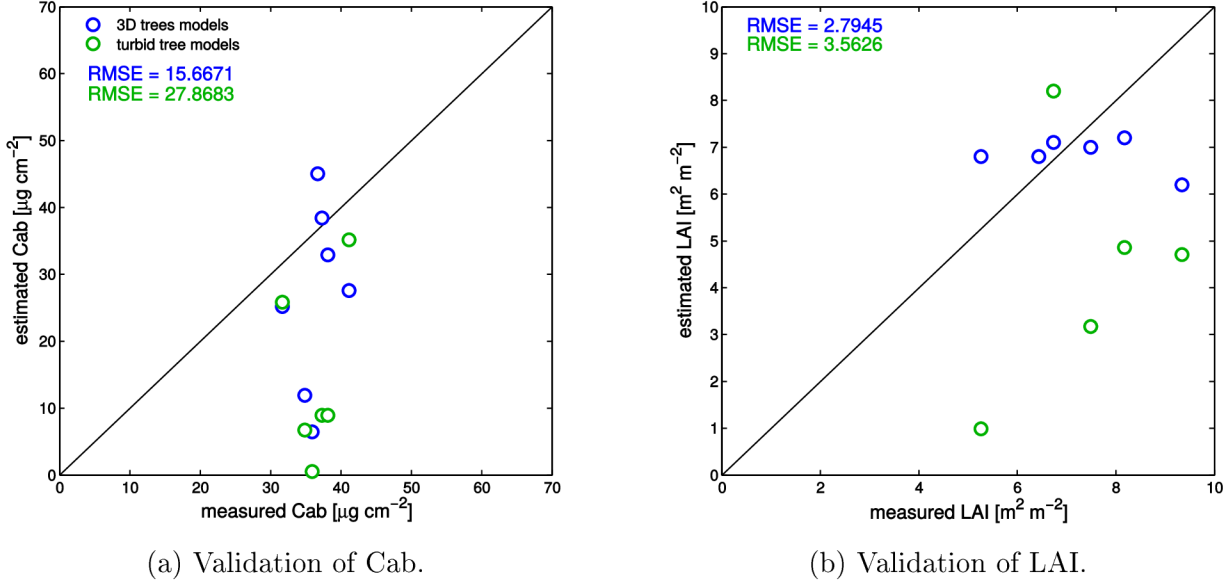
(b) Validation of LAI.

Figure 3.45: Validation of the estimated Cab and LAI values from S2 images of seven localities at the Bílý Kříž site. In graphs are two sets of data depends on 3D spruce models used for generation of the LUT. First are used 3D spruce models transformed to turbid cells (blue) and second are used the base spruce models (green). There are also calculated RMSE value for both cases and both parameters.

From the RMSE values can be seen that the retrievals with the 3D spruce model are closer to the field data than the case with the base spruce model. In case of the Cab estimation the RMSE decreased from 27.9 $\mu g \, cm^{-2}$ to 15.7 $\mu g \, cm^{-2}$, in case of LAI it decreased from 3.5 $m^2 \, m^{-2}$ to 2.8 $m^2 \, m^{-2}$ because of implementing the 3D spruce model. Regarding the spatial patterns, the Cab map derived from the 3D spruce model exhibits realistic pattern, whereas the maps derived from the base spruce model has high number of negative values. The LAI map derived from the 3D spruce model also exhibits more realistic pattern than the map derived from the base spruce model, where values seems to be distributed randomly. Despite this, the estimated LAI derived from the 3D spruce model does not capture the variability as observed in the field data. The possible explanation is that the variability of LAI in the LUT with the 3D spruce model is not sufficient and the SVM method is not able to cope with that fact.

3.5.4 Main outcome

The last aim of this study was to assess the improvement achieved in the remote sensing estimation of the two vegetation parameters, Cab and LAI, after operational implementation of the newly designed 3D spruce model. The validation against field data of both canopy traits estimated using the base and the 3D spruce models was performed. Results showed that the accuracy of both parameters retrieved from a Sentinel-2 multispectral image was improved when the precise 3D spruce model transformed into the turbid cell representation was implemented instead of the traditional DART turbid tree model. The improvement was clearly observed in a higher consistency of spatial patterns in both Cab and LAI maps.

Nevertheless, the direct comparison with the field data suggests that there is still a room for further improvements. For example, the application of the Sentinel-2 image topographic correction, which was not available during this study, would decrease the angular anisotropy of a spruce canopy HDRF. This correction removes canopy reflectance differences especially on steeper slopes of different expositions (northern vs. southern slopes), which would reduce mathematical illpostness of the retrievals and consequently increase their accuracies. Other potential improvement could be a meaningful restriction of the DART simulated LUT based on a prior knowledge, such as known topography, canopy covers and/or a reasonable limitation of ranges of free (searched) variables (Cab and LAI). This approach would, however, require production of more specialized DART LUTs applicable to specific forest types. The retrieval would require pre-classification and segmentation of the satellite image into the corresponding forest type classes. It should be mentioned, that misclassified forest types coupled during the retrieval process with an inappropriate LUT could potentially result in even higher errors then current approach.

4 | Synthesis and outlook

This chapter summarizes main scientific achievements, conclusions and outlines potentials for future use of the newly designed 3D spruce model in forest radiative transfer modelling.

4.1 Main conclusions and impact

The detailed computer 3D model of Norway spruce tree, based on reconstruction of terrestrial LiDAR point clouds, was successfully created. A new algorithm was developed for biologically correct distribution of the needle shoots within the reconstructed tree crowns. Optimization of the 3D spruce model was conducted and tested at three structural levels, at the scale of shoot, tree crown, and canopy. Achieved results showed that use of the optimized 3D spruce model with a simplified shoot model (labeled as simple 1) and transformed into turbid cell mockup yielded significantly better results when compared to outputs obtained with the traditional simpler spruce model. Besides higher accuracy estimates of canopy chlorophyll content and leaf area index retrieved from spectral remote sensing data through DART LUT inversion, this work contributed to new improvements of the DART model itself. Triggered by needs of this study, DART developers improved functions translating geometrical objects in turbid cell representations, introduced better model file management and optimized the DART code in general.

4.2 Potential improvements

One possible improvement of the 3D spruce model is creation of more realistic reference needle shoot model. The one used in this study was relatively simple, because it was designed for older versions of the DART model with limited capabilities of 3D objects handling. Moreover, it does not resemble the real natural distribution of individual needles along the central wooden twig. The architecture of each shoot varies depending on illuminations conditions, age and stress impacts. Precise 3D representation of shoot can be obtained from laboratory laser scanning. Although several shoot types were recreated this way, it was unfeasible to use them all within the framework of this thesis. The scanned shoots contain gaps, irregularities, and extremely high number of facets, which would require time demanding preprocessing. However, with a constant improvement of the DART model computational resources, we can expected its ability to process trees with more complex shoot models soon.

Similarly, it might be in future feasible to simulate larger forest scenes entirely reconstructed from airborne laser scanning data with the site-specific tree spatial and height distributions. Radiative transfer simulations of such scenes could facilitate retrievals of vegetation biochemical parameters from RS data fully customized to the study site conditions.

Additionally, a possible future extension of the algorithms creating the 3D models of trees is its adaptation to other coniferous or even further to broadleaf tree species.

4.3   Possible application of the 3D spruce model

In general, the 3D spruce model designed in this study can be used to understand better light interactions within a single tree crowns or whole canopies.

From RS perspective, one of the key issues in coniferous forest canopies is the upscaling of optical properties from needles, to shoots and to canopies. From operational point of view, it is easier to measure optical properties of needles rather than shoots. However, since shoots are the main scattering elements in the coniferous forest canopies, there is a strong demand to know shoot optical properties and phase functions with a high accuracy (Stenberg 1996, Smolander & Stenberg 2003, Rautiainen et al. 2012, and Mõttus et al. 2012). Traditional forest reflectance models, based on the radiative transfer equations, handle shoot level clumping by correcting the radiation attenuation coefficient with a clumping index, which simulates a reduction in the interception of radiation by the canopy at fixed LAI (Smolander & Stenberg 2003). Implementation of the precise 3D spruce model could help to disentangle and understand better light interaction related to the foliage clumping.

Finally, the 3D spruce model has been used to investigate scattering, reabsorption and angular isotropy of the chlorophyll fluorescence emissions produced by the plant cellular photosystems I and II. Results, presented at the Remote Sensing of Fluorescence, Photosynthesis and Vegetation Status Workshop (Malenovský et al. 2017), demonstrated a strong angular anisotropy of the top-of-canopy chlorophyll fluorescence signal caused by size, spatial geometry and clumping of spruce needles and shoots. Such sensitivity analyses contribute to full comprehension of this new vegetation optical signa, which will from 2022 acquired by a new ESA satellite mission called FLEX (Drusch et al. 2016).

List of Abbreviations

BRF   Bidirectional Reflectance Factor

Cab   leaf Chlorophyll a+b content

Car   Carotenoid content

CESBIO   Centre d'Etudes Spatiales de la BIOsphère

Cm   Dry matter content

Cw   Water content

DART   Discrete Anisotropic Radiative Transfer

ESA   European Space Agency

HDRF   Hemispherical-Directional Reflectance Factor

HDTF   Hemispherical-Directional Transmittance Factor

LAD   Leaf Angle Distribution

LAI   Leaf Area Index

LiDAR   Light Detection and Ranging

LUT   Look-Up-Tables

MSE   Mean Square Error

N   N-number used by PROSPECT

NIR   Near InfraRed

RAMI   RAdiation transfer Model Intercomparison

RMSE   Root Mean Square Error

RS   Remote Sensing

RT   Radiative Transfer

RTM   Radiative Transfer Model

S2   Sentinel-2

SVC   Support Vector Classification

SVM	Support Vector Machines
SVR	Support Vector Regression
UTC	Coordinated Universal Time
UTM	Universal Transverse Mercator
VIS	VISible
WGS	World Geodetic System

References

Allen, W. A., Gausman, H. W., Richardson, A. J., & Thomas, J. R. (1969). Interaction of Isotropic Light with a Compact Plant Leaf. Journal of the Optical Society of America, 59(10), 1376–1379.

Allen, W. A., Gayle, T. V., & Richardson, A. J. (1970). Plant-Canopy Irradiance Specified by the Duntley Equations. Journal of the Optical Society of America, 60(3), 372–376.

Atzberger, C. (2004). Object-based retrieval of biophysical canopy variables using artificial neural nets and radiative transfer models. Remote Sensing of Environment 93, 53–67.

Barták, M. (1992). Struktura koruny smrku ztepilého ve vztahu k produkci (Doctoral thesis). Institute of Systematic and Ecological Biology, Brno, Czech Republic

Barták, M., Dvořák, V., Hudcová, L. (1993). Rozložení biomasy jehlic v korunové vrstvě smrkového porostu. Lesnictví, 39(4), 273281.

Bennett, K. P., & Campbell, C. (2000). Support vector machines: hype or hallelujah? ACM SIGKDD Explorations Newsletter, 2(2), 1–13.

Baret, F., & Buis, S. (2008). Estimating Canopy Characteristics from Remote Sensing Observations: Review of Methods and Associated Problems. In Advances in Land Remote Sensing, S. Liang, ed. (Springer Netherlands), pp. 173–201.

Borovička, V., & Pazdera, J. (2009). Technická zpráva - Zaměření dospělého smrkového porostu v lokalitě Černá hora - Šumava. GEOVAP,spol.s r.o., Pardubice.

Boser, B. E., Guyon, I. M., & Vapnik, V. N. (1992). A Training Algorithm for Optimal Margin Classifiers. In Proceedings of the 5th Annual ACM Workshop on Computational Learning Theory (pp. 144–152). ACM Press.

Bréda, N. J. J. (2003). Ground-based measurements of leaf area index: a review of methods, instruments and current controversies. Journal of Experimental Botany, 54(392), 2403–2417.

CESBIO (2016) Centre d'Etudes Spatiales de la BIOsphère. DART User's manual (V5.6.2)

CESBIO (2015) Centre d'Etudes Spatiales de la BIOsphère. DART Handbook (October 9, 2015)

Chang, C.-C., & Lin, C.-J. (2001). Training v-support vector classifiers: theory and algorithms. Neural Computation, 13(9), 2119–2147.

Chang, C.-C., & Lin, C.-J. (2002). Training nu-support vector regression: theory and algorithms. Neural Computation, 14(8), 1959–1978.

Chang, C.-C., & Lin, C.-J. (2011). LIBSVM: a library for support vector machines. ACM Transactions on Intelligent Systems and Technology (TIST), 2(3), 27.

Chen, J. M., & Black, T. A. (1992). Defining leaf area index for non-flat leaves. Plant, Cell & Environment, 15(4), 421–429.

Chen, J. M. (1996). Optically-based methods for measuring seasonal variation of leaf area index in boreal conifer stands. Agricultural and Forest Meteorology, 80(2–4), 135–163.

Ciganda, V., Gitelson, A., & Schepers, J. (2009). Non-destructive determination of maize leaf and canopy chlorophyll content. Journal of Plant Physiology, 166(2), 157–167.

Combal, B., Baret, F., Weiss, M., Trubuil, A., Mace, D., Pragnere, A., Myneni, R., Knyazikhin, Y., & Wang, L. (2002). Retrieval of canopy biophysical variables from bidirectional reflectance - Using prior information to solve the ill-posed inverse problem. Remote Sensing of Environment 84, 1–15.

Cortes, C., & Vapnik, V. (1995). Support-Vector Networks. Machine Learning, 20(3), 273–297.

Crisp, D. J., & Burges, C. J. (1999). A Geometric Interpretation of v-SVM Classifiers. In Neural Information Processing Systems Conference, 12, 44–250.

Croft, H., Chen, J.M., Zhang, Y., & Simic, A. (2013). modelling leaf chlorophyll content in broadleaf and needle leaf canopies from ground, CASI, Landsat TM 5 and MERIS reflectance data. Remote Sensing of Environment 133, 128–140.

Curran, P.J., Dungan, J.L., & Peterson, D.L. (2001). Estimating the foliar biochemical concentration of leaves with reflectance spectrometry: Testing the Kokaly and Clark methodologies. Remote Sensing of Environment 76, 349–359.

Darvishzadeh, R., Skidmore, A., Atzberger, C., & van Wieren, S. (2008). Estimation of vegetation LAI from hyperspectral reflectance data: Effects of soil type and plant architecture. International Journal of Applied Earth Observation and Geoinformation 10, 358–373.

Darvishzadeh, R., Matkan, A.A., & Ahangar, A.D. (2012). Inversion of a Radiative Transfer Model for Estimation of Rice Canopy Chlorophyll Content Using a Lookup-Table Approach. IEEE Journal of Selected Topics in Applied Earth Observations and Remote Sensing 5, 1222–1230.

Drusch, M., Moreno, J., Bello, U. D., Franco, R., Goulas, Y., Huth, A., . . . Verhoef, W. (2016). The FLuorescence EXplorer Mission Concept-ESA's Earth Explorer 8. IEEE Transactions on Geoscience and Remote Sensing, PP(99), 1–12.

Everitt, B. (1977). Cluster analysis. London: Heinemann Educational Ltd.

Feret, J.-B., François, C., Asner, G.P., Gitelson, A.A., Martin, R.E., Bidel, L.P.R., Ustin, S.L., le Maire, G., & Jacquemoud, S. (2008). PROSPECT-4 and 5: Advances in the leaf optical properties model separating photosynthetic pigments. Remote Sensing of Environment 112, 3030–3043.

Féret, J.-B., François, C., Gitelson, A., Asner, G. P., Barry, K. M., Panigada, C., ... Jacquemoud, S. (2011). Optimizing spectral indices and chemometric analysis of leaf chemical properties using radiative transfer modeling. Remote Sensing of Environment, 115(10), 2742–2750.

Ferguson, T. S. (2015, January 13), Linear Programming, *Electronic references.* Retrieved from http://www.math.ucla.edu/ tom/LP.pdf

Gastellu-Etchegorry, J.-P., Demarez, V., Pinel, V., & Zagolski, F. (1996). Modeling radiative transfer in heterogeneous 3-D vegetation canopies. Remote Sensing of Environment 58, 131–156.

Gastellu-Etchegorry, J.-P., Martin, E., & Gascon, F. (2004). DART: a 3D model for simulating satellite images and studying surface radiation budget. International Journal of Remote Sensing 25, 73–96.

Gastellu-Etchegorry, J.-P., Yin, T., Lauret, N., Cajgfinger, T., Gregoire, T., Grau, E., Feret, J.-B., Lopes, M., Guilleux, J., Dedieu, G. a kol (2015). Discrete Anisotropic Radiative Transfer (DART 5) for Modeling Airborne and Satellite Spectroradiometer and LIDAR Acquisitions of Natural and Urban Landscapes. Remote Sensing 7, 1667–1701.

Gauch, H. G. (1982). Multivariate Analysis in Community Ecology. Cambridge University Press.

Gitelson, A.A., Gritz, Y., & Merzlyak, M.N. (2003). Relationships between leaf chlorophyll content and spectral reflectance and algorithms for non-destructive chlorophyll assessment in higher plant leaves. Journal of Plant Physiology 160, 271–282.

Gonzalez, R. C., & Woods, R. E. (2002). Digital image processing (2nd ed). Upper Saddle River, N.J: Prentice Hall.

Govaerts, Y.M., & Verstraete, M.M. (1998). Raytran: a Monte Carlo ray-tracing model to compute light scattering in three-dimensional heterogeneous media. IEEE Transactions on Geoscience and Remote Sensing 36, 493–505.

Hanzel, V., Novotný, J., Cibulka, M., & Homolová, L. (2014). Aerial and terrestrial laser scanning. In Zemek, F. et al., *Airborne remote sensing: theory and practice in assessment of terrestrial ecosystems* (pp. 63–74). Global Change Research Institute CAS, Brno.

Hogg, R. V., & Craig, A. T. (1978). Introduction to mathematical statistics (4. ed). New York: Macmillan.

Homolová, L. (2005). Leaf Area Index estimation for Norway Spruce forest stand by means of radiative transfer modeling and imaging spectroscopy. Thesis Report. Wageningen University.

Homolová, L., Malenovský, Z., Hanuš, J., Tomášková, I., Dvořáková, M., & Pokorný, R. (2007). Comparison of different ground techniques to map leaf area index of Norway spruce forest canopy. In Proceedings of ISPRS Working Group VII/1 Workshop, Schaepman, M. et al., *Physical Measurements and Signatures in Remote Sensing*, 28(14), 12–5.

Homolová, L., Lukeš, P., Malenovský, Z., Lhotáková, Z., Kaplan, V., & Hanuš, J. (2013). Measurement methods and variability assessment of the Norway spruce total leaf area: implications for remote sensing. Trees, 27(1), 111–121.

Homolová, L., Pivovarník, P., & Zemek, F. (2014). Introduction and basic theory of remote sensing. In Zemek, F. et al., *Airborne remote sensing: theory and practice in assessment of terrestrial ecosystems* (pp. 15–35). Global Change Research Institute CAS, Brno.

Homolová, L., Malenovský, Z., Janoutová, R., Landier, L., Gastellu-Etchegorry, J.-P. (2015a). Technical note - Validation Database Description. Red Edge Positioning (REP) Techniques for Earth Observation Optical Missions (AO/1-7600/13/NL/LvH). Published by European Space Agency (p.38)

Homolová, L., Malenovský, Z., Janoutová, R., Landier, L., Crochet, T., Berthelot, B. (2015b). Algorithm Theoretical Basis Document - Retrieval of Biophysical Variables: Leaf Chlorophyll Content and Leaf Area Index (REDEDGE-CG-CESBIO-ATBD-03-0002). Red Edge Positioning (REP) Techniques for Earth Observation Optical Missions (AO/1-7600/13/NL/LvH). Published by European Space Agency (p.88).

Houborg, R., Anderson, M., & Daughtry, C. (2009). Utility of an image-based canopy reflectance modeling tool for remote estimation of LAI and leaf chlorophyll content at the field scale. Remote Sensing of Environment 113, 259–274.

Huck, A. & Berthelot, B. (2015). Algorithm Theoretical Basis Document - Rededge spectra reconstruction (REDEDGE-TN-054-MAG). Red Edge Positioning (REP) Techniques for Earth Observation Optical Missions (AO/1-7600/13/NL/LvH). Published by European Space Agency (p.29).

Jacquemoud, S., & Baret, F. (1990). PROSPECT: a model of leaf optical properties spectra. Remote Sensing of Environment 34, 75–91.

Jacquemoud, S., Verhoef, W., Baret, F., Bacour, C., Zarco-Tejada, P.J., Asner, G.P., François, C., and Ustin, S.L. (2009). PROSPECT + SAIL models: a review of use for vegetation characterization. Remote Sensing of Environment 113, Supplement 1, S56–S66.

Jain, A. K., & Dubes, R. C. (1988). Algorithms for Clustering Data. Upper Saddle River, NJ, USA: Prentice-Hall, Inc.

Jan, C., Homolová, L., Janoutová, R., Gastellu-Etchegorry, J.-P. (2016). Technical note - Database Description. Hyperspectral analysis and heterogeneous surface modelling (HYPOS) (AO/1-8345/15/NL/LvH). Published by European Space Agency (p.51).

Janoutová, R. (2012). Mathematical methods of morphology modelling of coniferous trees. Brno University of Technology. Brno: Vysoké učení technické v Brně, Fakulta strojního inženýrství, pp. 51.

Jensen, J. R. (2005). Introductory Digital Image Processing (3 edition). Upper Saddle River, N.J: Prentice Hall. pp 526.

Jones, H. G. & Vaughan, R. A. (2010). Remote sensing of vegetation: principles, techniques, and applications. Oxford University Press, Oxford ; New York

Kimes, D., Gastellu-Etchegorry, J., & Estève, P. (2002). Recovery of forest canopy characteristics through inversion of a complex 3D model. Remote Sensing of Environment 79, 320–328.

Laurent, V.C.E., Verhoef, W., Damm, A., Schaepman, M.E., & Clevers, J.G.P.W. (2013). A Bayesian object-based approach for estimating vegetation biophysical and biochemical variables from APEX at-sensor radiance data. Remote Sensing of Environment 139, 6–17.

Legendre, P., & Legendre, L. F. J. (1998). Numerical Ecology. Elsevier.

Legendre, P., & Rogers, D. J. (1972). Characters and clustering in taxonomy: a synthesis of two taximetric procedures. Taxon, 21,567-606.

le Maire G, François C, Soudani K, et al. (2008). Calibration and validation of hyperspectral indices for the estimation of broadleaved forest leaf chlorophyll content, leaf mass per area, leaf area index and leaf canopy biomass. Remote Sensing of Environment 112, 3846–3864.

Leonenko, G., Los, S.O., & North, P.R.J. (2013). Statistical Distances and Their Applications to Biophysical Parameter Estimation: Information Measures, M-Estimates, and Minimum Contrast Methods. Remote Sensing 5, 1355–1388.

Leuschner, C., Voß, S., Foetzki, A., & Clases, Y. (2006). Variation in leaf area index and stand leaf mass of European beech across gradients of soil acidity and precipitation. Plant Ecology, 186(2), 247–258.

Liang, S. (2005). Quantitative Remote Sensing of Land Surfaces (John Wiley & Sons).

MacKay, D. J. (2003). Information theory, inference and learning algorithms. Cambridge university press.

MacQueen, J. B. (1967). Some Methods for classification and Analysis of Multivariate Observations. Proceedings of 5-th Berkeley Symposium on Mathematical Statistics and Probability 1, 281-297.

Main, R., Cho, M.A., Mathieu, R., O'Kennedy, M.M., Ramoelo, A., & Koch, S. (2011). An investigation into robust spectral indices for leaf chlorophyll estimation. ISPRS Journal of Photogrammetry and Remote Sensing 66, 751–761.

Malenovský, Z., Albrechtová, J., Lhotáková, Z., Zurita-Milla, R., Clevers, J. G. P. W., Schaepman, M. E., & Cudlín, P. (2006). Applicability of the PROSPECT model for Norway spruce needles. International Journal of Remote Sensing, 27(24), 5315–5340.

Malenovský, Z., Martin, E., Homolová, L., Gastellu-Etchegorry, J.-P., Zurita-Milla, R., Schaepman, M. E., . . . Cudlín, P. (2008). Influence of woody elements of a Norway spruce canopy on nadir reflectance simulated by the DART model at very high spatial resolution. Remote Sensing of Environment, 112(1), 1–18.

Malenovský, Z., Homolová, L., Zurita-Milla, R., Lukeš, P., Kaplan, V., Hanuš, J., . . . Schaepman, M. E. (2013). Retrieval of spruce leaf chlorophyll content from airborne image data using continuum removal and radiative transfer. Remote Sensing of Environment, 131(0), 85–102.

Malenovský, Z., Gastellu-Etchegorry, J.-P., Lauret, N., Yin, T., Guilleux, J., Chavanon, E., Janoutová, R., Verhoef, W., van der Tol, C., Cook, B., Morton, D., & Middleton, E.M. (2017). Discrete Anisotropic Radiative Transfer (DART) modelling of chlorophyll fluorescence in three-dimensional structurally explicit plant canopies [poster]. In Remote Sensing of Fluorescence, Photosynthesis and Vegetation Status Workshop.

Marková, I., Pavelka, M., Krejza, J., Janouš, D. (2015). Meteorological Yearbook 2012. Global Change Research Institute CAS, Brno.

Mather, P. M., & Koch, M. (2004). Computer Processing of Remotely-Sensed Images: An Introduction. Chichester, UK: John Wiley & Sons, Ltd.

McGarigal, K., Cushman, S., Stafford, S. (2000). Multivariate statistics for wildlife and ecology research. Springer, Berlin.

Morsdorf, F., Kötz, B., Meier, E., Itten, K. I., & Allgöwer, B. (2006). Estimation of LAI and fractional cover from small footprint airborne laser scanning data based on gap fraction. Remote Sensing of Environment, 104(1), 50–61.

Mõttus, M., Rautiainen, M., & Schaepman, M. E. (2012). Shoot scattering phase function for Scots pine and its effect on canopy reflectance. Agricultural and Forest Meteorology, 154–155, 67–74.

Nikolov, N., & Zeller, K. F. (2003). Modeling coupled interactions of carbon, water, and ozone exchange between terrestrial ecosystems and the atmosphere. I: Model description. Environmental Pollution, 124(2), 231–246.

North, P. (1996). Three-dimensional forest light interaction model using a Monte Carlo method. IEEE Transactions on Geoscience and Remote Sensing 34, 946–956.

Pokorný, R., & Marek, M. V. (2000). Test of Accuracy of LAI Estimation by LAI-2000 under Artificially Changed Leaf to Wood Area Proportions. Biologia Plantarum, 43(4), 537–544.

Pokorný, R., & Stojnič, S. (2013). Leaf area index of Norway spruce stands in relation to age and defoliation. Beskydy, 5(2), 173–180.

Porra, R. J., Thompson, W. A., & Kriedemann, P. E. (1989). Determination of accurate extinction coefficients and simultaneous equations for assaying chlorophylls a and b extracted with four different solvents: verification of the concentration of chlorophyll standards by atomic absorption spectroscopy. Biochimica et Biophysica Acta (BBA)-Bioenergetics, 975(3), 384–394.

Rautiainen, M., Mõttus, M., Yáñez-Rausell, L., Homolová, L., Malenovský, Z., & Schaepman, M. E. (2012). A note on upscaling coniferous needle spectra to shoot spectral albedo. Remote Sensing of Environment, 117, 469–474.

Richards, J. A., & Xia, X. (2005). Remote Sensing Digital Image Analysis: An Introduction. Berlin: Springer.

Richter, R., & Schläpfer, D. (2002). Geo-atmospheric processing of airborne imaging spectrometry data. Part 2: Atmospheric/topographic correction. International Journal of Remote Sensing, 23(13), 2631–2649.

Rivera, J.P., Verrelst, J., Leonenko, G., & Moreno, J. (2013). Multiple Cost Functions and Regularization Options for Improved Retrieval of Leaf Chlorophyll Content and LAI through Inversion of the PROSAIL Model. Remote Sensing 5, 3280–3304.

Russ, J. C. (2006). The Image Processing Handbook, Fifth Edition (5 edition). CRC Press.

Schaepman-Strub, G., Schaepman, M. E., Painter, T. H., Dangel, S., & Martonchik, J. V. (2006). Reflectance quantities in optical remote sensing—definitions and case studies. Remote Sensing of Environment, 103(1), 27–42.

Schlerf, M., & Atzberger, C. (2006). Inversion of a forest reflectance model to estimate structural canopy variables from hyperspectral remote sensing data. Remote Sensing of Environment 100, 281–294.

Schölkopf, B., Smola, A. J., Williamson, R. C., & Bartlett, P. L. (2000). New support vector algorithms. Neural Computation, 12(5), 1207–1245.

Schölkopf, B., Platt, J. C., Shawe-Taylor, J., Smola, A. J., & Williamson, R. C. (2001). Estimating the support of a high-dimensional distribution. Neural Computation, 13(7), 1443–1471.

Sloup, P. (2013). Automatic Tree Reconstruction from its Laser Scan. Master Thesis. Masaryk University Faculty of Informatics, Brno, (p.74).

Sloup, P., Rebok, T. & Hanuš, J. (2013). Automatic Tree Reconstruction from its Laser Scan [poster]. In Global Change and Resilience, Brno.

Smola, A. J., & Schölkopf, B. (2004). A tutorial on support vector regression. Statistics and Computing, 14(3), 199–222.

Smolander, S., & Stenberg, P. (2003). A method to account for shoot scale clumping in coniferous canopy reflectance models. Remote Sensing of Environment, 88(4), 363–373.

Sneath, P. H. (1957). The application of computers to taxonomy. Microbiology, 17(1), 201–226.

Sneath, P. H. A., & Sokal, R. R. (1973). Numerical Taxonomy: the Principles and Practice of Numerical Classification. W. H. Freeman.

Sokal, R. R., & Rohlf, F. J. (1962). The Comparison of Dendrograms by Objective Methods. Taxon, 11(2), 33–40.

Stenberg, P. (1996). Simulations of the effects of shoot structure and orientation on vertical gradients in intercepted light by conifer canopies. Tree Physiology, 16(1), 99–108.

Stuckens, J., Dzikiti, S., Verstraeten, W. W., Verreynne, S., Swennen, R., & Coppin, P. (2011). Physiological interpretation of a hyperspectral time series in a citrus orchard. Agricultural and Forest Meteorology, 151(7), 1002–1015.

Tso, B., & Mather, P.M. (2001). Classification Methods for Remotely Sensed Data. Taylor and Francis Inc., New York.

Vapnik, V. N. (1998). Statistical Learning Theory (1 edition). New York: Wiley-Interscience.

Verrelst, J., Alonso, L., Camps-Valls, G., Delegido, J., & Moreno, J. (2012a). Retrieval of Vegetation Biophysical Parameters Using Gaussian Process Techniques. IEEE Transactions on Geoscience and Remote Sensing 50, 1832–1843.

Verrelst J, Muñoz J, Alonso L, et al. (2012b). Machine learning regression algorithms for biophysical parameter retrieval: Opportunities for Sentinel-2 and -3. Remote Sensing of Environment 118, 127–139.

Watson, D. J. (1947). Comparative Physiological Studies on the Growth of Field Crops: I. Variation in Net Assimilation Rate and Leaf Area between Species and Varieties, and within and between Years. Annals of Botany, 11(1), 41–76.

Weiss, M., Baret, F., Myneni, R., Pragnère, A., & Knyazikhin, Y. (2000). Investigation of a model inversion technique to estimate canopy biophysical variables from spectral and directional reflectance data. Agronomie 20, 3–22.

Wellburn, A. R. (1994). The spectral determination of chlorophyll a and chlorophyll b, as well as total carotenoids, using various solvents with spectrophotometers of different resolution. Journal of Plant Physiology, 144(3), 307–313.

Widlowski, J.-L., Mio, C., Disney, M., Adams, J., Andredakis, I., Atzberger, C., . . . Zenone, T. (2015). The fourth phase of the radiative transfer model intercomparison (RAMI) exercise: Actual canopy scenarios and conformity testing. Remote Sensing of Environment, 169, 418–437.

Williams, W. T., Lance, G. N., Dale, M. B., & Clifford, H. T. (1971). Controversy concerning the criteria for taxonometric strategies. The Computer Journal, 14(2), 162–165.